A Measurement of the Gluon Density in the Proton Based on Charm Production at HERA

Inaugural–Dissertation

zur

Erlangung der philosophischen Doktorwürde

vorgelegt der

Philosophischen Fakultät II

der

Universität Zürich

von

David Müller

aus Pfäffikon ZH

begutachtet von Prof. Dr. Peter Truöl

und Dr. Felix Sefkow

Zürich 1998

Die vorliegende Arbeit wurde von der Philosophischen Fakultät II der Universität Zürich auf Antrag von Prof. Dr. Peter Truöl und Prof. Dr. Roland Engfer als Inaugural–Dissertation angenommen.

Abstract

A measurement of the cross sections for the production of charmed mesons in deep inelastic positron–proton scattering is presented in this thesis. The gluon density in the proton can be extracted from this result.

The data were collected in 1995 with the H1 detector at the HERA storage ring where high–energy positrons collide with a beam of protons. In the momentum transfer range $2\ \mathrm{GeV}^2 \leq Q^2 \leq 100\ \mathrm{GeV}^2$ considered here, the positron is detected in the backward calorimeter. By requiring a $D^\star$ meson decaying into the channel $D^{\star\pm} \to D^0 {\pi_s}^\pm \to (K^\mp \pi^\pm){\pi_s}^\pm$ inside the central tracking system, events induced by a photon–gluon fusion process ($\gamma g \to c\bar{c}$) can be selected. An analysis of the photon and $D^\star$ meson kinematics allows to approximately calculate the momentum of the incoming gluon.

The data are corrected for experimental inefficiencies. The photon is reconstructed using information from the scattered positron as well as the hadronic final state of the event. Higher order QCD effects as well as the hadronization of the charm quark into the measured $D^\star$–meson are taken into account by using an unfolding procedure based on a QCD calculation in next–to–leading order (NLO).

Results for the gluon density in NLO are presented here in a range of $7.5 \cdot 10^{-4} \leq x_g \equiv p_{Gluon}/p_{Proton} \leq 2.5 \cdot 10^{-2}$. They agree within errors with theoretical NLO predictions and with an independent measurement at the H1 experiment based on a QCD analysis of the inclusive structure function F_2.

Zusammenfassung

Die vorliegende Arbeit beschreibt eine Messung des differentiellen Wirkungsquerschnitts für die Produktion von Charm-Mesonen in tief-inelastischer Positron-Proton Streuung, aus denen die Gluondichte im Proton bestimmt werden kann.

Die analysierten Daten wurden 1995 mit dem H1 Detektor am Positron–Proton Speicherring HERA aufgezeichnet. Im betrachteten kinematischen Bereich bei Impulsüberträgen von $2\ \mathrm{GeV}^2 \leq Q^2 \leq 100\ \mathrm{GeV}^2$ wird das Positron im rückwärtigen Kalorimeter des Experiments nachgewiesen. Ereignisse aufgrund des Photon–Gluon Fusionsprozesses ($\gamma g \rightarrow c\bar{c}$) werden selektiert, indem ein $D^\star$–Meson im Zerfallskanal $D^{\star\pm} \rightarrow D^0 {\pi_s}^\pm \rightarrow (K^\mp \pi^\pm){\pi_s}^\pm$ verlangt wird. Aus den gemessenen Impulsen von Photon und $D^\star$ kann der Impuls des Gluons näherungsweise bestimmt werden.

Zur Rekonstruktion des Photonimpulses wird die experimentelle Information über das gestreute Positron und den hadronischen Endzustand verwendet. Verluste von Ereignissen durch die Selektionsschnitte werden mithilfe einer Monte-Carlo Simulation des Detektors korrigiert. Zur Rekonstruktion der Kinematik auf dem Parton–Niveau wird eine Entfaltungsmethode verwendet, die sowohl den Einfluss von Prozessen höherer Ordnung als auch die Hadronisierung des Charm–Quarks zum $D^\star$–Meson berücksichtigt. Die Entfaltung stützt sich auf eine störungstheoretische QCD Rechnung zweiter Ordnung.

Die im Bereich von $7.5 \cdot 10^{-4} \leq x_g \equiv p_{Gluon}/p_{Proton} \leq 2.5 \cdot 10^{-2}$ gemessene Gluondichte in NLO wird mit theoretischen Vorhersagen und einer unabhängigen Messung basierend auf Skalenverletzungen der Strukturfunktion F_2 verglichen. Die Resultate stimmen innerhalb der Messunsicherheiten gut überein.

Contents

Chapter 1

Introduction

1.1 Parton densities in the proton

The electron (positron)–proton collider HERA was built to allow new insight into the structure of hadrons. Unlike the electron, the proton is a compound object which is made out of *quarks* and *gluons*. These constituents are called *partons*. Interactions of quarks and gluons at high energies are very well described by perturbative *QCD(Quantum Chromodynamics)*. The structure of the hadrons is however characterized by the interactions of the partons at low energies and cannot be predicted from first principles. Thus it is necessary to probe the proton structure experimentally with leptons, where high center–of–mass energies allow to resolve smallest structures.

At HERA, ep scattering is dominated by the exchange of a photon which couples electromagnetically to the positron and to a quark inside the proton, as indicated in Figure 1.1 a). This process is sensitive to the quark density inside the proton. The coupling of gluons and quarks in the proton leads to the effect of the so–called *scaling violations* which allows to extract the gluon density from measurements of the quark density functions. A more direct measurement of the gluon density can be achieved when charmed mesons are required in the final state: the production of charm quarks proceeds predominantly through *boson–gluon fusion (BGF)*, i. e. when the photon couples via a $c\bar{c}$ pair to a gluon from the proton (see Fig. 1.1 b)). The fraction of the proton momentum carried by the struck gluon (x_g) can be determined from the measured final state of the event. Therefore it is possible to measure a differential cross section $d\sigma/dlog(x_g^{obs})$ which is almost directly proportional

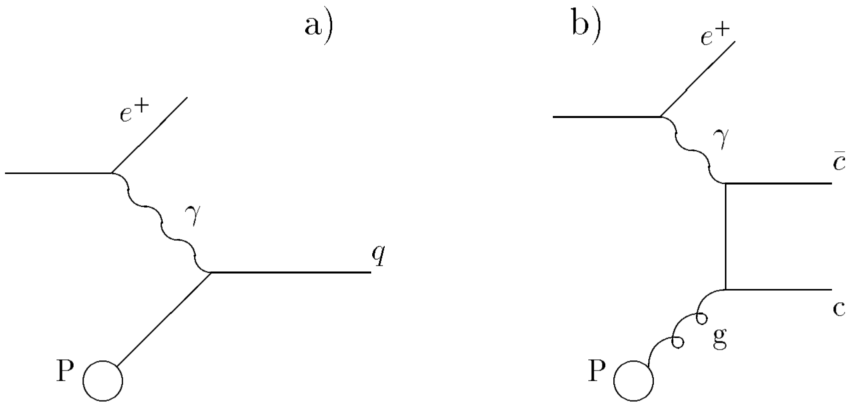

Figure 1.1: *ep scattering processes at HERA: a) lowest order electron–quark scattering; b) boson–gluon fusion of a $c\bar{c}$ pair*

to the gluon density in the proton.

With the help of a QCD calculation, the gluon density can be derived from this cross section. The result can then be compared to the gluon density function obtained from the analysis of the scaling violations of the structure function F_2, which represents a non–trivial test of QCD and of the concept of the universality of the parton density functions.

1.2 Overview of the measurement

The measurement presented here proceeds in two major steps which are summarized in this section. The references given in brackets indicate the sections where details can be found. For illustration, a good event candidate is shown in Figures 1.2 and 1.3 .

1.2.1 Cross section measurement

We observe deep inelastic scattering (DIS) of 27.5 GeV positrons on 820 GeV protons inside the H1 detector. The production of charm quarks proceeds mostly through the photon gluon fusion process ($\gamma g \to c\bar{c}$) where the gluon made up part of the proton (Section 2.3.1). Charm quarks can be tagged by reconstructing invariant masses from the final state particles according to the decay chain $c \to D^{\star +} \to D^0 \pi_s^+ \to K^- \pi^+ \pi_s^+$ (+ c. c.). Improved accuracy

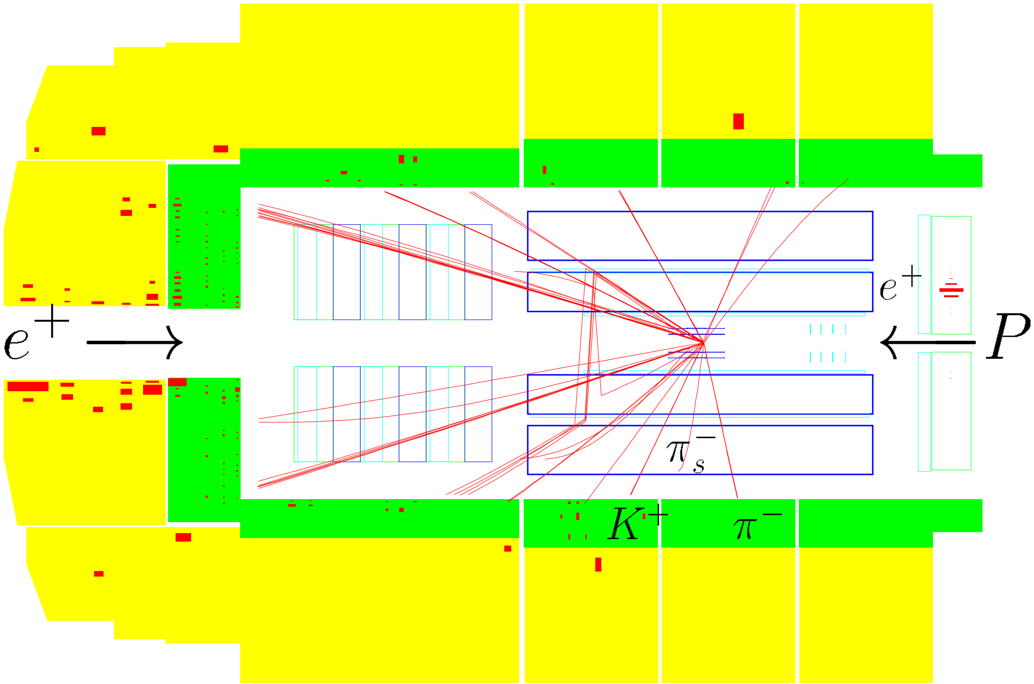

Figure 1.2: *Side view of a $D^\star$ in DIS candidate event. The proton has entered from the right, the positron from the left side.*

is reached by inspecting the mass difference between the $D^\star$ and the D^0 candidate (4.4.3). The scattered positron is measured in the backward calorimeter (3.5, 4.3) and, together with the hadronic finale state, is used to determine the momentum transfer between positron and proton ($e\Sigma$ method) (4.3.2). Experimental cuts guarantee that the final state particles are well measured; these cuts define the visible range of the measurement (4.1). The polar angle of the decay products is limited by the acceptance of the central tracking chambers (3.4). Additional cuts on the final state particles are needed in order to obtain a clean sample and are corrected for by using a *Monte Carlo* description of the detector (4.4.1, 4.4.2). The final event sample contains, apart from the process we are interested in, events from the decay of b quarks (4.4.5) and $D^\star$ mesons from other than the selected decay chains, faking a mass peak (*reflections*) (4.4.4). These effects are compensated. In addition we correct for event losses due to the emission of a photon from

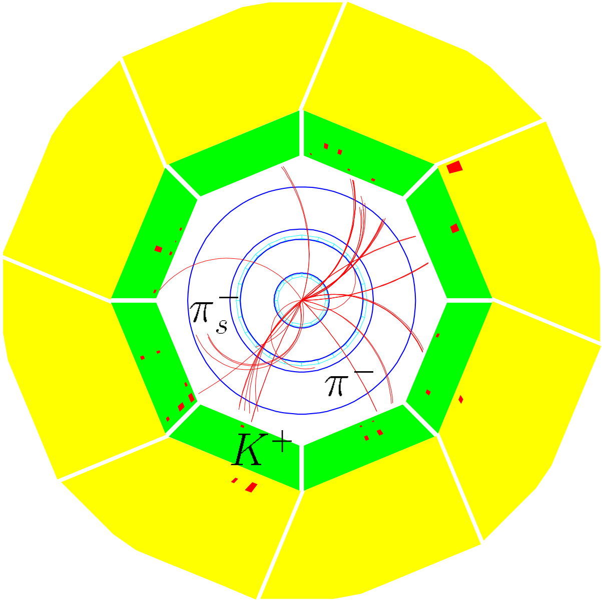

Figure 1.3: *Front view of a $D^\star$ in DIS candidate event*

the positron just before the scattering process takes place (ISR) (4.3.3). Systematic errors introduced by the uncertainties of the energy scales and due to the applied corrections are evaluated (4.5). A sample of 152±17 $D^\star$ mesons has been reconstructed from a total luminosity $\mathcal{L}$ =2.40 pb^{-1} . This yields a visible cross section $\sigma_{D^\star}^{visible} = 5.48\ \pm 0.63(stat)\ ^{+0.82}_{-0.66}(syst)$ nb (4.6). In addition, we give differential cross sections, among others as a function of the variable $log(x_g^{obs})$, defined to approximate the fractional momentum of the incoming gluon as good as possible from the observable final state (2.3.3). These results depend only very weakly on the used MC calculation, as no extrapolation to the full phase space of the $D^\star$ has been done and the used model was found to be consistent with the data in the range of the measurement.

1.2.2 Determination of the gluon density

For the extraction of the gluon density from the measurement, a QCD calculation in *Next–to–Leading Order (NLO)* has been used (2.3.5) . The main task of that calculation is to compute the hard partonic cross section $\hat{\sigma}$ for the positron–gluon scattering process. The cuts defining the visible range of the measurement could be implemented in that calculation. The fragmentation of the charm quark into the $D^\star$ meson is described using the Peterson fragmentation model (2.3.2). Various predicted cross sections have been checked and were found to be in agreement with the data. The measured cross section as a function of $log(x_g^{obs})$— which has maximal sensitivity to the gluon density — has therefore been compared to the theoretical expectation as well. It is given by the product of the gluon density $g(x_g^{true})$ with the hard partonic cross section $\hat{\sigma}$, smeared by a correlation function $A(x_g^{true}, x_g^{obs})$ which absorbs the NLO contributions and the fragmentation effects. As we measured the cross section for $D^\star$ production, the calculated charm production cross section has to be scaled by the fragmentation fraction $BR(c \to D^\star)$.

$$\frac{d\sigma^{theo}_{ep\to eD^\star X}}{d\log{(x_g^{obs})}} = BR_{(c\to D^\star)} \cdot \int dx_g^{true} A(x_g^{true}, x_g^{obs}) \cdot \frac{d\hat{\sigma}}{d\log{(x_g^{true})}} \cdot g(x_g^{true}) \ . \qquad (1.1)$$

The measured cross section has been unfolded using an iterative procedure (5.1) based on the smearing matrix A (5.2). The results are given in Sections 5.3 and 6 .

Chapter 2

Physics at HERA

This section tries to give a schematic introduction into the field of *Quantum Chromodynamics* (*QCD*) and hadron structure. The aim is not to be complete or to be mathematically self-contained. The idea of the section is to introduce all the terms needed later on and to give some intuitive pictures of the physical processes we deal with. More complete introductions can be found in textbooks [1, 2, 3, 4].

2.1 Overview

The positron proton collider HERA allows the study of ep scattering in a large kinematical range. Designed for accelerating electrons and positrons, HERA has been operated with positrons from 1994 to 1997. With beam energies of 820 GeV for the protons and 27.5 GeV for the positrons, a total center–of–mass energy of $\sqrt{s} \approx 300$ GeV is reached. Thus positrons are scattered on protons at roughly an order of magnitude higher energies than were observed in previous fixed target experiments at the *Stanford Linear Accelerator Center (SLAC)* [5, 6] and at *CERN* [7].

For a qualitative overview of the physics accessible at HERA, we need to briefly sketch the quark-parton model of the proton.

Quark parton model

The concept of explaining the properties of all known hadrons through their *quark* constituents has been developed independent of measurements of the proton structure. Measurements of cross sections for lepton–proton scattering

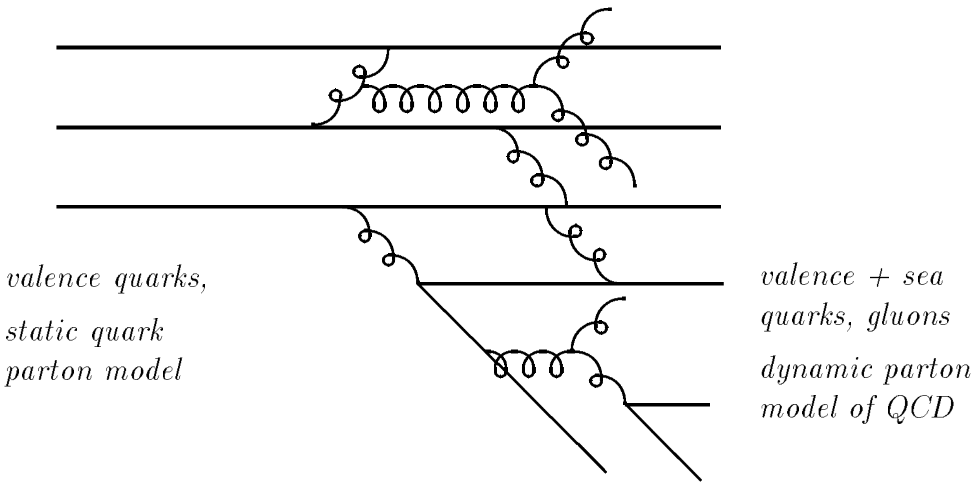

Figure 2.1: *Sketch of the splitting of quarks and gluons in the proton (see text).*

have on the other hand revealed that the proton is composed of smaller particles, which have been called *partons*. Only later it could be shown that both concepts involve the same particles and the partons have been identified with the quarks. In addition we find a large number of *gluons*, the intermediate bosons of the strong interaction, in the proton. These gluons must be regarded as partons, too.

In the *static quark parton model*, the proton is composed of three quarks. The charge of the proton equals the sum of the charges of these quarks. Are the other observable properties of the proton equally calculable from a sum over the properties of its quarks? For instance, does each quark carry a third of the momentum of a high–energy proton? Lepton–proton scattering experiments showed that the distribution of the parton momenta is smeared. The total momentum carried by the quarks amounts to only about half the momentum of the proton[8]. In addition, a large number of quarks and antiquarks with low momenta were observed. The reason for this is sketched in Figure 2.1: The strong interaction, which binds the quarks together, is mediated by gluons. The gluons couple to the *color charge (R,G,B)* of the quarks, carrying a color and an anticolor themselves. Virtually, the gluons may split into a quark–antiquark or a gluon–gluon pair. All these new partons again couple to each other and so forth. In the case of a high–energy proton,

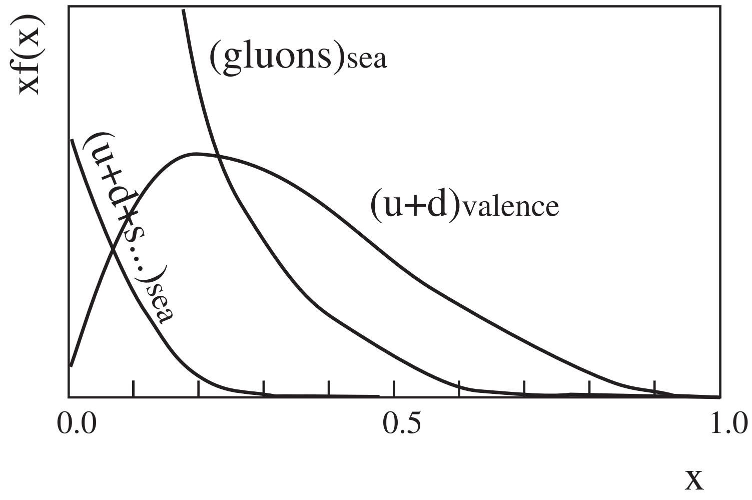

Figure 2.2: *Sketch of the parton densities.*

the momentum of each parton is distributed on two daughter partons at every splitting. Therefore all these virtual partons, called the *sea* of the proton, have low momenta, the sum of all the momenta carried by gluons however amounts to approximately half the proton momentum. The variable x denotes the fraction of the proton momentum carried by a parton. Figure 2.2 shows a sketch of the distributions of the quarks and gluons as a function of x. The quark distributions are separated into a *valence* contribution (the three quarks of the static model) and the *sea* quark contribution (the quarks virtually generated from the splitting of gluons).

Kinematic range accessible at HERA

Depending on the negative four-momentum transfer (Q^2) between positron and proton, we can define three different domains. The cross sections decrease rapidly with increasing Q^2. The kinematical variables are correlated, such that high Q^2 corresponds to high x.

- $Q^2 \geq 100$ GeV^2 : *Deep Inelastic Scattering (DIS) at high* Q^2. These events are due to interactions between the positron and a high–momentum parton out of the proton. They are therefore mostly induced by scattering off a *valence quark*. At the highest center–of–mass energies of the photon-parton system, these events might reveal new

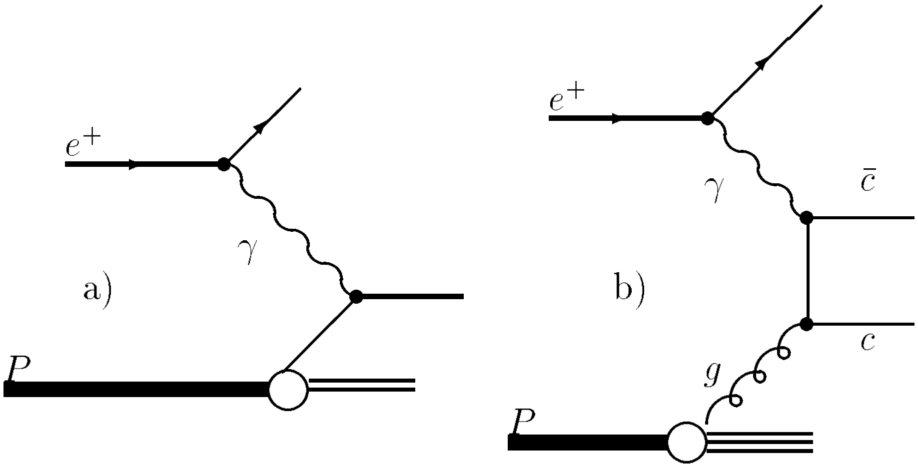

Figure 2.3: *a) Lowest Order DIS scattering process at HERA: the photon couples to one of the quarks in the proton. b) The* γ–gluon *fusion process has an additional vertex and is suppressed. It is however the simplest possible process leading to charmed mesons in the final state.*

physics beyond the *standard model*. For $Q^2 = \mathcal{O}(M_Z^2)$, the electroweak interactions between positron and parton mediated via a photon or a Z^0 boson (*neutral currents*) and $W^\pm$ exchange (*charged currents*) attain comparable strength. The events are experimentally characterized by very high transverse momenta [9].

- $0.35\ \mathrm{GeV}^2 \leq Q^2 \leq 100\ \mathrm{GeV}^2$: *DIS at low and moderate* Q^2. In this domain the positron–parton interaction is predominantly mediated by a virtual photon. We observe the partons which have only very small momenta, i. e. *sea* partons at low x [10, 11]. This kinematical regime will be discussed in some more detail in the following sections since the present analysis deals with a subclass of these *DIS* events. Experimentally, these events are characterized by the detection of the scattered positron in a calorimeter around the outgoing positron beam.

- $Q^2 \approx 0\ \mathrm{GeV}^2$: *Photoproduction.* The photon emitted by the positron is almost on-shell. It is emitted collinear with the positron and carries an energy of several GeV in the laboratory frame. The analyses of photoproduction at HERA deal mostly with the hadronic structure of these photons. [12, 13, 14]. Photoproduction can be tagged through the detection of the positron at very low scattering angles.

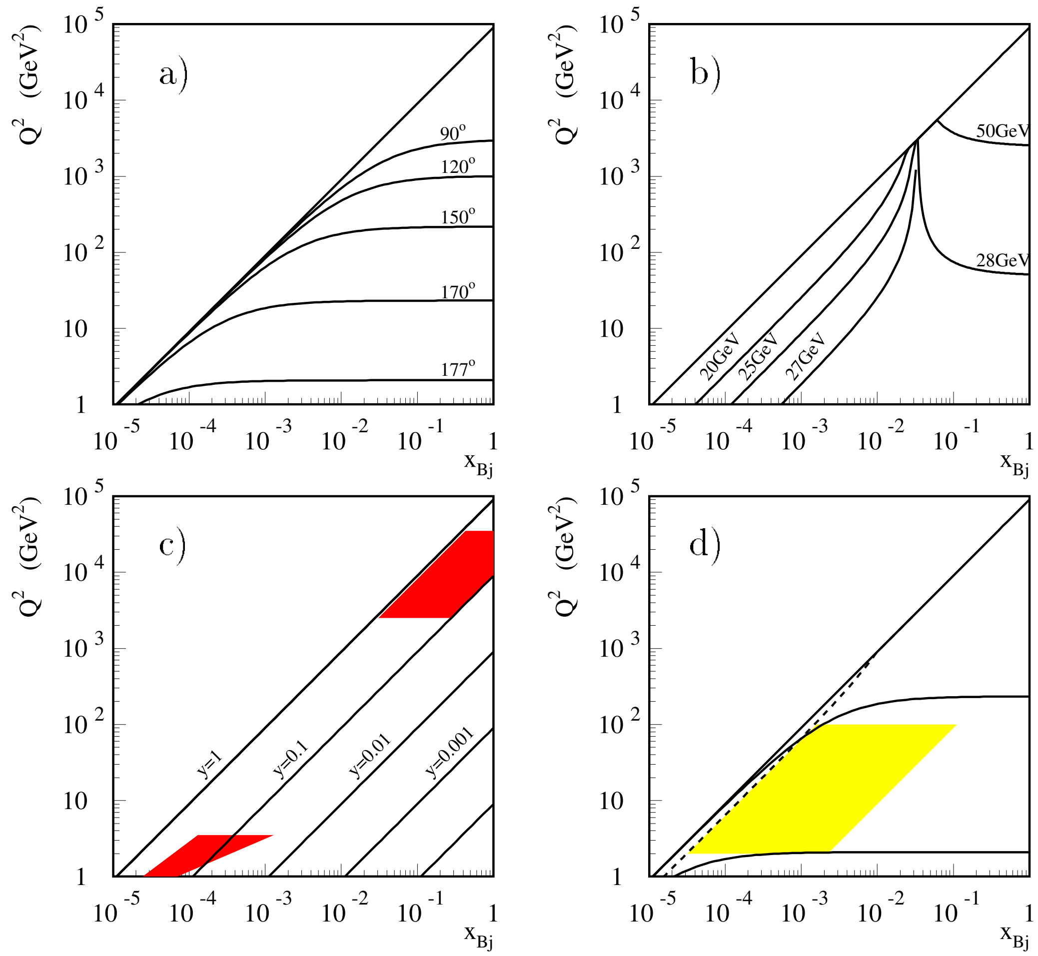

Figure 2.4: *Variables of the scattered positron in the (x_{Bj}, Q^2) – plane. (See Table 2.2) Only the lower triangle is kinematically possible. Figure a) shows lines of constant scattering angle (for the definition see Figure 2.5). Lines of constant positron energies are shown in b). The lines with constant y (see Table 2.2) are shown in c). The latter figure also illustrates the outer ends of the range accessible with the H1 detector: the lower area indicates the region investigated in a recent low Q^2 DIS analysis [10], the upper field has been covered by the very high Q^2 analysis [9]. The kinematical range selected in the analysis presented here is shown in plot d) (see also Section 4.1). The solid lines indicate the experimental cuts applied for the positron scattering angle, the dashed line corresponds to the selected positron energy. (See Section 4.3.1)*

2.2 Deep inelastic scattering at moderate Q^2

2.2.1 Kinematical variables

In lowest order, *DIS* scattering at HERA arises in the quark parton model when a photon emitted by the positron scatters off a quark of the proton (see Figure 2.3 a)). The recoil of the struck quark is hard enough that the proton breaks apart. The four–momenta of the particles involved are defined in Table 2.1 . The right-handed coordinate system used at H1 is shown in Figure 2.5 . The proton beam enters the detector along the z axis. All polar angles are called θ and are measured with respect to the positive z axis. Weakly scattered positrons will therefore emerge with θ_e close to 180°. The azimuthal angle ϕ in the xy plane is measured with respect to the x-axis.

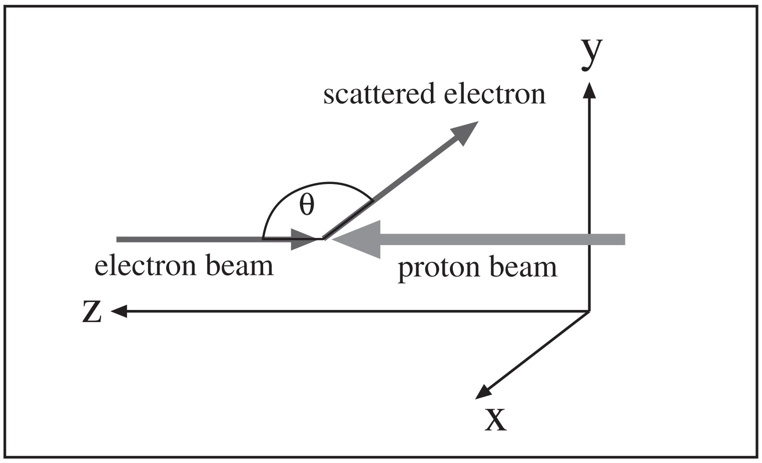

Figure 2.5: *Definition of the coordinate system.*

The pseudorapidity η as defined below varies between $\eta = 1.5$ at $\theta \approx 20°$ and $\eta = -1.5$ at $\theta \approx 160°$.

$$\eta = -\ln\left(\tan\left(\theta/2\right)\right) . \tag{2.1}$$

In addition, we will use in the following several scalar variables as defined in Table 2.2 . In the *photoproduction limit* of very small Q^2 where $\theta_e \to 180°$, $y = (1 - E_{e'}/E_e)$ holds. In this case y therefore denotes the fraction of the positron momentum carried away by the collinear photon. Similarly, x_{Bj} can be interpreted in the leading order quark parton model as being the

Particle	four–momentum	in H1 coordinates ($m_e \equiv m_p \equiv 0$)
Incoming Positron	k	$(E_e, 0, 0, -E_e)$
Scattered Positron	k'	$(E_{e'}, ., ., E_{e'}\cos(\theta_e))$
Photon $\gamma^\star$	$q = k - k'$	$(E_e - E_{e'}, ., ., .)$
Incoming Proton	P	$(E_P, 0, 0, E_P)$
Incoming Parton	p	$(E_p, 0, 0, E_p)$
Scattered Parton	$p' = p + q$	

Table 2.1: *Definition of four–vectors in DIS*

fraction of the proton momentum carried by the colliding quark. In general, x denotes the momentum fraction of the initial state parton, whereas x_{Bj} is defined kinematically as in Table 2.2. Note that all formulae given hold only for the case that the energies of the particles are much higher than their masses. Transverse momenta of the incoming partons are neglected as well. The accurate determination of Q^2 and x_{Bj} from the data is one of the major challenges for every DIS analysis and will be explained in Section 4.3.

2.2.2 Parton densities

Asymptotic freedom

The wavelength of the considered photons $\Delta = \hbar/|Q| \approx 0.02$ fm, is smaller than the radius of the proton. The interaction time (i. e. the time it takes the photon to travel through the proton) is much shorter than the time scale of the interactions between the quarks of the proton. The hard interaction therefore does not couple to the proton as a whole, but only to one parton. On this time scale the struck quarks or gluons can be regarded as free particles. The term *asymptotic freedom* refers to the concept that quarks become more and more independent of their hadronic environment, when Q^2 increases and the time scale becomes shorter. This effect is described in QCD through the running of the strong coupling constant $\alpha_s \sim (\log(Q^2/\Lambda^2_{QCD}))^{-1}$. α_s increases towards infinity when Q^2 approaches Λ^2_{QCD} (i. e. large distances) but decreases to zero when the momentum transfer becomes very large. The

Quantity	Definition
negative square of four–momentum transfer	$Q^2 = -q^2 = (k-k')^2 = 2E_eE_{e'}(1+\cos\theta_e)$
ep center–of–mass energy	$\sqrt{s} = \|(k+P)\| = 4E_eE_P$
mass of the hadronic system	$W = \|(P+q)\| = \sqrt{m_P^2 - Q^2 + 2P\cdot q}$
	$y = \frac{q\cdot P}{k\cdot P} = 1 - \frac{E_{e'}(1-\cos\theta_e)}{2E_e}$
Bjorken scaling variable	$x_{Bj} = \frac{Q^2}{ys} =^1 \frac{E_p}{E_P}$

Table 2.2: *Definition of kinematical variables.*

parameter Λ_{QCD} has to be determined from data and is found to be in the order of 225 MeV. This scale dependence of the coupling constant can be explained by the presence of a cloud of virtual gluons that surrounds any particle which carries color charge (see e. g. Reference [3]).

Factorization

The cross sections for hard photon-parton scattering are calculable in perturbative QCD. In the experiment however, we measure positron–proton cross sections. While the positron is a point–like particle, the proton needs to be understood as a cloud of partons with different momenta. Mathematically this can be expressed by writing the ep cross section σ as the convolution of the positron–parton cross section $\hat{\sigma}_i$ with a parton density function f_i. This formulation is know as *factorization*. The sum runs over all partons i [2].

$$\sigma(k,P) = \sum_i \int f_i(x,\mu_f^2)\cdot\hat{\sigma}_i(k, x\cdot P, \mu_f^2)dx \; . \tag{2.2}$$

A new variable, the *factorization scale* μ_f^2 has to be introduced in equation 2.2. Figure 2.6 illustrates for the example of gluon emission why this is necessary. Gluon emission can be regarded as a higher order effect of the photon–quark scattering and hence would need to be taken into account

[1]This identity is an interpretation of x_{Bj} in the quark parton model and only holds for the case of leading order photon–quark scattering.

[2]In this thesis, the gluon density will usually be called $g(x_g)$ rather than $f_g(x_g)$.

by the hard cross section $\hat{\sigma}_i$. It can also be considered as a part of the 'internal life of the proton'. The density function f_i should then include this process which shifts the quark to lower values of x. The factorization scale μ_f^2 sets the threshold, which of the two possibilities is chosen. If the transverse momentum squared of the gluon is smaller than μ_f^2, the gluon is considered to be part of the long-distance physics and is absorbed in the density function. If the gluon transverse momentum exceeds the factorization scale, it is considered to be part of the short–distance physics of the hard photon quark scattering process and hence absorbed in $\hat{\sigma}_i$. Variations of the factorization scale should not affect the result, since contributions to the hadronic cross section are simply shifted from one mathematical term to the other. The hardest scale of the event, typically the maximal $p_\perp^2$ or Q^2, is used. In charm quark production, the mass of the generated quark gives a more reliable scale and one uses $4 \cdot m_c^2 + Q^2$ or $4 \cdot (m_c^2 + p_\perp^2)$. For our measurement, it is necessary to repeat the theoretical calculations varying μ_f^2 within a reasonable range[3]. Differences of the results are treated as systematic errors of the calculation since they reflect the importance of terms of even higher order.

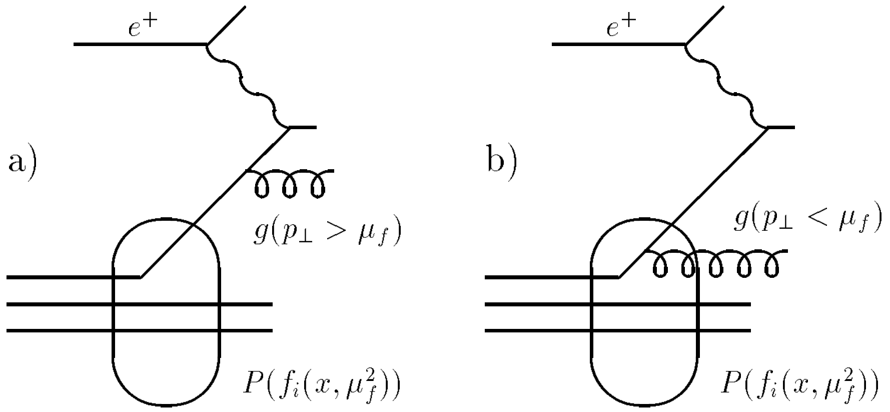

Figure 2.6: *Gluon emission, a) interpreted as part of the hard scattering process, b) absorbed in the parton density function.*

[3]With this variation one must of course remain in the range where the concept of perturbative QCD can be applied i.e. where α_s is sufficiently small.

Leading and higher order contributions

The example of gluon emission illustrated that processes with different numbers of vertices may lead to the same scattered positron in the final state. All such processes must be included in the calculation of the partonic cross sections $\hat{\sigma}_i$. This is of course impossible since it would mean that not only the emission of one gluon, but also the cases with any large number of gluons would have to be calculated. It is therefore necessary to determine which processes are dominating and which processes can be neglected. A very useful scheme is to apply an ordering in α_s : if the phase space factors are comparable for the different processes, higher numbers of emitted gluons are still suppressed by the fact that a factor α_s enters in the amplitude of the process with every additional vertex. Hence more vertices mean less importance for that effect.[4] In many of the processes observed at HERA the lowest order α_s contribution (*Leading Order, LO*) and contributions with one additional vertex (*Next–to–Leading Order, NLO*) have been calculated.

It is important to stress in this context, that the parton density functions themselves are not observables but purely theoretical concepts. The only measurable quantities are the cross sections on the hadron level. Depending e. g. on the order of the calculation and on the value of α_s used, the partonic cross sections $\hat{\sigma}_i$ will be different and therefore a different parton density will be derived from a measured hadronic cross section. However the parton density functions still are universal in the sense that e. g. a quark density measured in NLO at a given μ_f^2 at HERA can be used to calculate proton–proton cross sections at the same factorization scale in NLO.

Even though the task of counting vertices (or powers of α_s) may seem straightforward, it can sometimes lead to confusion. The lowest order process with charmed particles in the final state has one vertex more than the lowest order DIS (see Figure 2.3). For an *inclusive* measurement (requiring nothing but the scattered positron) this process is therefore NLO whereas it is LO in the context of our *exclusive* measurement requiring the charmed meson in the final state.

[4]This ordering has been used first in the framework of perturbative QED where contributions are ordered by the powers of α. Note that in the case of QCD the difference between different orders is much less pronounced since $0.1 \leq \alpha_s \leq 1$ in the range of our measurement.

Fragmentation and renormalization

Up to now we have considered the outgoing quarks as the final state particles of the scattering process. This is of course not true, only hadrons with no net color charge can be observed in a detector. After the hard scattering process a color field exists between the struck quark and the proton remnant. With increasing distance between quark and remnant, the energy of the field becomes large enough to generate additional $q\bar{q}$ pairs. This process is called *fragmentation*. It stops when all the generated quarks are bound in colorless hadrons.

If the initial energy of the quark is high enough, the secondary particles generated will form a well defined jet, i. e. a narrow bundle of particles visible in the detector. The momentum of the primary quark can then be very well approximated by the sum of the momenta of these particles in the final state. In Section 2.3.2 we will discuss the situation if only the heaviest particle of the final state instead of the jet is used for approximating the quark momentum.

The possibility that the outgoing quark emits additional gluons requires special treatment since the corresponding probability becomes infinite for vanishing momenta (*soft divergences*) and gluon emission parallel to the quark (*collinear divergences*). The emission of *real* gluons and *virtual* internal loops however destructively interfere. With appropriate mathematical treatment, *renormalization*, these divergences can be controlled. Renormalization however introduces an additional cutoff parameter, the so–called *renormalization scale* μ_r^2. Its implications on experimental problems are very similar to those imposed by the factorization scale μ_f^2 and in most cases it makes sense to choose $\mu_r^2 = \mu_f^2$.

2.2.3 The structure function F_2

The structure functions are defined as parametrizations of the observed cross sections for neutral currents via

$$\frac{d^2\sigma(x_{Bj}, Q^2)}{dx_{Bj}dQ^2} = \frac{4\pi\alpha^2}{x_{Bj}Q^4}\left(y^2 x_{Bj}F_1 + (1-y)F_2 - (y - \frac{y^2}{2})x_{Bj}F_3\right) \quad . \tag{2.3}$$

All the functions F_i depend on x_{Bj} and Q^2. The term F_3 describes the interferences between the exchange of a photon and a Z^0 boson. At moderate values of Q^2 this term is heavily suppressed due to the high mass of the Z^0 and can therefore be neglected.

Interpretation in the quark parton model

If the differential cross section of Equation 2.3 is calculated under the assumption that the proton is composed of quarks, one obtains:

$$F_2(x, Q^2) = \sum_{a=u,\bar{u},d,\bar{d},s,\bar{s}} e_a^2 x f_a(x, Q^2) \ , \tag{2.4}$$

$$F_1(x, Q^2) = 0 \qquad \text{(for spin-0 quarks)} \ , \tag{2.5}$$

$$F_1(x, Q^2) = \frac{1}{2x} F_2(x, Q^2) \qquad \text{(for spin-1/2 quarks)} \ . \tag{2.6}$$

The latter formula is called *Callan-Gross relation* and was used to prove that the quarks are spin-$\frac{1}{2}$ particles. The formula for F_2 gives us a prescription how to relate the observed cross section to the quark densities. The problem that the sum runs over all different flavors $(u,d,s,\dots)$ of quarks *and* antiquarks can be overcome by considering neutrino–proton scattering experiments too, which will not be discussed here.

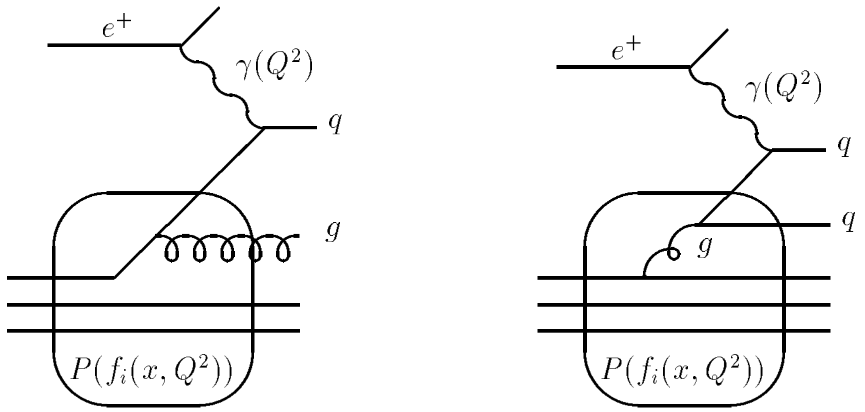

Figure 2.7: *Processes leading to scaling violations of F_2.*

Bjorken scaling and scaling violations

In Equation 2.4 we have written the quark densities f_a as functions of x and Q^2, which is on the first sight counter–intuitive since we have introduced the parton densities as *'the probability to find a parton with the momentum fraction x inside the proton'*. This should obviously not depend on Q^2. The

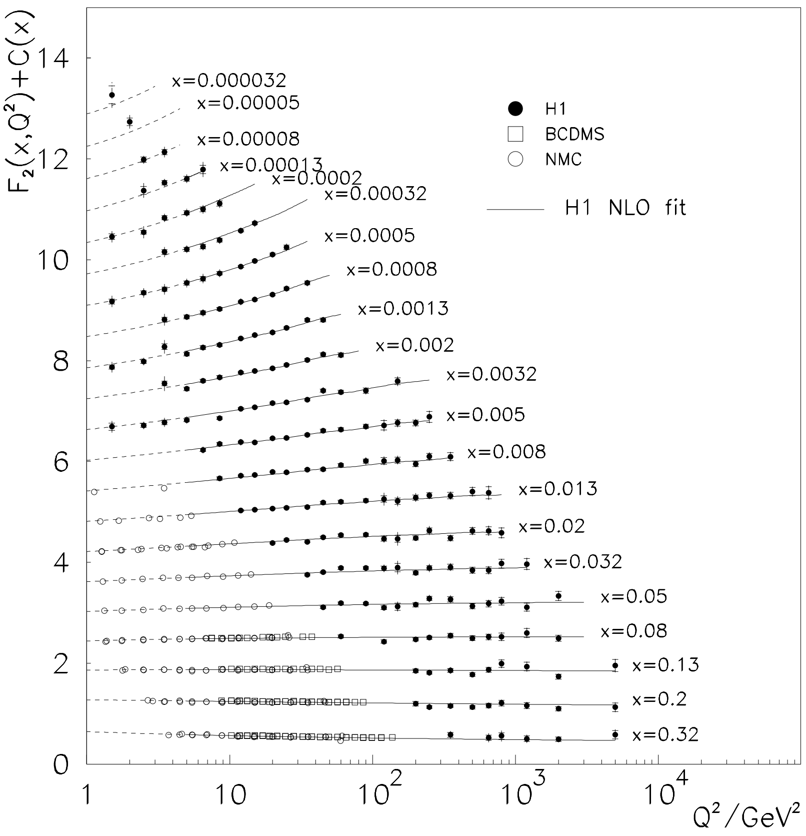

Figure 2.8: *Scaling violation of* F_2 *[15].*

expected independence of the parton densities from the energy scale of the experiment is called *Bjorken scaling*. Precision measurements as shown in Figure 2.8 have however revealed slight deviations from this scaling which are very well described by perturbative QCD. The reasons are sketched in Figure 2.7 a) with a process we have encountered already: if a quark emits an additional gluon before it couples to the photon, some of the quark momentum gets lost. The quark is therefore shifted to lower values of x. This emission violates energy and momentum conservation, in the absence of the photon it occurs therefore only virtually. The higher the energy scale Q^2 of the photon is, the more probable it will be that this gluon emission is resolved by the measurement. Therefore $f_a(x, Q^2)$ rises with Q^2 for low values of x whereas it drops with Q^2 for large x. In the process shown in Figure 2.7 b) a gluon of the sea splits into a $q\bar{q}$ pair and the photon couples subsequently to one of these sea–quarks. This process is sensitive to the gluon density of the proton and raises the parton densities at low values of x with increasing Q^2. The variations of the parton densities with Q^2 are coupled to all parton densities, which is described by the *DGLAP evolution equations* (see e. g. Reference [3]). Presently, the most precise measurements of the gluon density are derived from the analysis of the scaling violations of F_2. These analyses use an ansatz of the parton densities at a starting scale Q_0^2 and evolve to higher values of Q^2 according to the *DGLAP* evolution equations. The parameters of the ansatz functions are determined from a fit to the large number of data points of F_2. This procedure does not 'translate' the measured cross sections point per point into gluon densities but produces a smooth function with an error band. A cross check of this rather indirect method with an independent measurement is therefore desirable and will be done in the conclusions of this thesis.

2.3 D* production in DIS

2.3.1 Charm production mechanisms

If we observe charmed mesons in the final state of a *DIS* event, the charm quarks may have come from two sources:

- The photon may have coupled to a charm quark in the sea of the proton (*intrinsic charm*).
- Charm may have been generated dynamically through *photon-gluon (boson-gluon) fusion* as illustrated in Figure 2.3 b)

Both mechanisms are predicted to occur at HERA. Their relative contributions depend strongly on the energy scale of the experiment. For Q^2 in the order of m_c^2 photon-gluon fusion dominates. In theoretical calculations of this process, the proton sea is assumed to consist of the three light quark and antiquark flavors *(u,d,s)* and gluons only. Charm quarks are treated as *massive* particles. With increasing momentum transfer, terms proportional to $\ln(Q^2/m_c^2)$ gain importance and a different scheme has to be used in the calculations. For $Q^2 \gg m_c^2$ charm must be treated as a *massless* quark. Through that, it will occur as part of the proton sea and we expect the production of charmed mesons to be dominated by the photon coupling to one of these sea quarks or antiquarks. Descriptions for the transition from the massive to the massless case are being developed in References [16, 17, 18, 19].

A measurement which discriminates between intrinsic charm and the boson–gluon fusion process has been published by H1 [20]. Figure 2.9 shows the differential cross section for charm production in the range of $10\ \mathrm{GeV}^2 \leq Q^2 \leq 100\ \mathrm{GeV}^2$, at $\langle W \rangle \approx 125$ GeV as a function of x_D, defined through $x_D = |\vec{p}^{\,*}_{D^0}|/|\vec{p}^{\,*}_P|$. The stars indicate that the D^0 and proton momentum are defined in the γp center-of-mass system. A fit of the sum of the predictions for *BGF* and *intrinsic charm* with free normalizations showed, that the charm sea contributes less than 5% at the 95% confidence level. From this measurement we may conclude that for the analysis presented here — at an even lower value of $\langle Q^2 \rangle$ — only γ–*gluon* fusion needs to be considered.

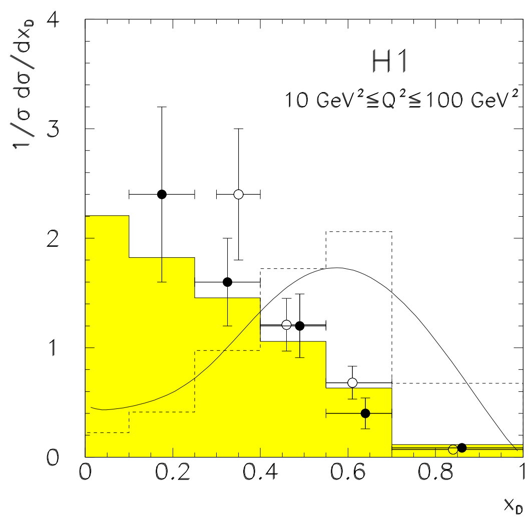

Figure 2.9: *The differential charmed mesons production cross section $d\sigma/dx_D$. x_D is defined as $|\vec{p}^{\,*}_{D^0}|/|\vec{p}^{\,*}_P|$. The open points are obtained from a $D^0(\bar{D}^0)$ analysis, the full points from $D^{\star\pm}$ decays. The shaded histogram shows the prediction of the AROMA[21] MC program based on γ-gluon fusion. The dashed histogram is obtained from a MC program [23] forced to simulate contributions from sea charm quarks only. The solid line is a QCD evolution of the results of $\nu N(\bar{\nu}N)$ scattering experiments where charm production is expected to proceed mainly via $W^\pm$ scattering off strange sea quarks. All histograms are normalized to one.*

2.3.2 Fragmentation of charm quarks

All the available measurements of the fragmentation process have been carried out at e^+e^- colliders, where the momenta of the charm quarks and their fragmentation products can be measured simultaneously [24, 25]. Since the gluon momentum is not known a priori, the center-of-mass energy of the γ–*gluon* system is not known at HERA. The fragmentation process is therefore much more difficult to measure at H1 and we have to rely on theoretical calculations. A consistent *NLO* adaption of the results gained at e^+e^- machines is however very delicate since the *ep* system at HERA is much more complicated than the e^+e^- system as different energy scales are present at the same time.

An elaborate simulation of the fragmentation process is implemented e.g. in the *AROMA MC* generator, the so-called *Lund String Model* where the breaking of the color field between the quarks and gluons is simulated in many steps. A much simpler description is available by using a *Peterson fragmentation function.* Comparisons of the results in *MC* have shown that the differences between the two models are very small [27]. In the Peterson model, the momenta of the final state mesons are obtained as a convolution of the charm quark distributions with the Peterson fragmentation function, defined through

$$D(z) = N \cdot \left(z(1 - \frac{1}{z} - \frac{\epsilon_c}{1-z})^2 \right)^{-1} \quad . \tag{2.7}$$

Here z denotes the fraction of the charm quark momentum carried by the charmed hadron and ϵ_c is a free parameter. Different values of ϵ_c have been determined experimentally, the extrema of the published values are shown in Figure 2.10 .

The fragmentation function is a phenomenological description and different implementations have been used:

- The four–momentum of the quark is multiplied by z. This scheme has the advantage that it is Lorentz invariant, however bears the problem that the mass of the meson comes out as $z \cdot m_c$, which is obviously wrong.

- The momentum three–vector in the lab frame is multiplied by z, the energy is set such that the resulting mass of the meson is correct.

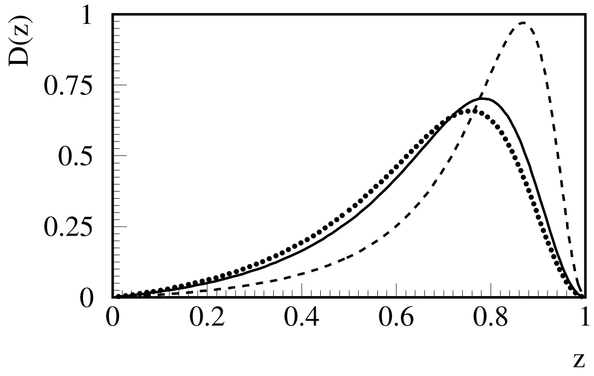

Figure 2.10: *Peterson fragmentation function for $\epsilon_c = 0.02$ (dashed) [29], 0.06 (solid) [25] and 0.078 (dotted) [24].*

- The momentum three–vector in the γp system is scaled. The argument for this procedure is that the color field spans between the outgoing partons and the proton remnant and that this treatment should therefore be closest to the e^+e^- situation.

- In reality the $D^\star$ meson will of course not be perfectly collinear with the initial charm quark. It therefore makes sense to add a contribution perpendicular to the charm quark direction to the $D^\star$ momentum.

If one wants to use a Peterson fragmentation, it is of course very important to use an ϵ_c which has been determined by a calculation which is consistent with the one it is applied to.

2.3.3 Reconstruction of x_g from the final state

Assuming that $D^\star$ mesons are predominantly produced by γ–*gluon* fusion we can — based on the leading order process — approximate the momentum of the incident gluon from the parameters measured in the detector [26] . Fragmentation and higher order effects are partly compensated by an empirical correction factor in the following formulae. The remaining differences between the reconstructed variable x_g^{obs} and the actual momentum of the gluon, denoted x_g^{true}, are in the end corrected by unfolding the measured cross section $d\sigma/dx_g^{obs}$.

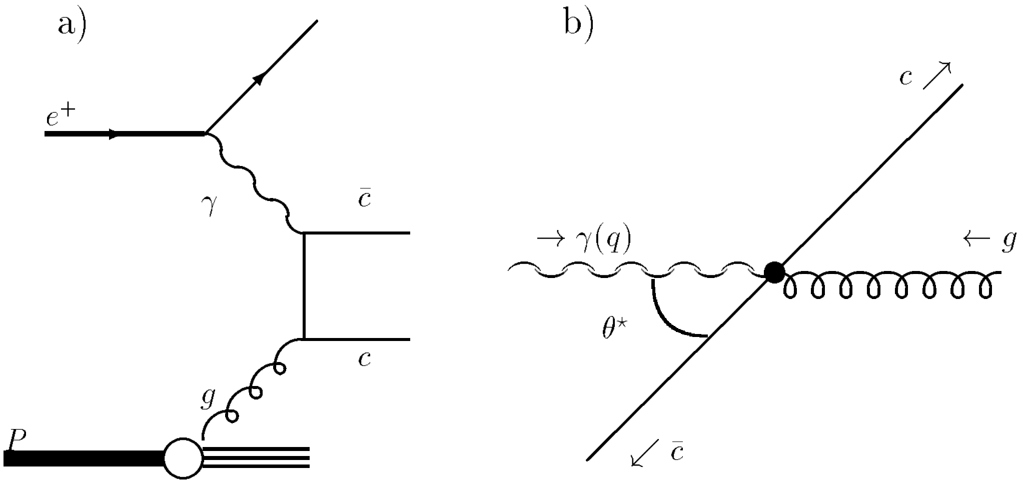

Figure 2.11: *a) Lowest order* γ–gluon *fusion process. The right picture illustrates the kinematic situation in the* γ–gluon *center-of-mass system.*

The kinematic configuration of the ($\gamma g \rightarrow c\bar{c}$) process in its center-of-mass system *(CMS)* is indicated in Figure 2.11 b), where the angle $\theta^\star$ is defined as well. The photon is described by the four-vector q, whereas we will use the terms g, c and $\bar{c}$ for the four-vectors of the according particles in the following, with e.g. $\vec{c^\star}$ being the charm quark momentum measured in the γp system. The z axis in the γp system is defined by the proton direction. Let us define j as the four-momentum of the γ–*gluon* system and $\hat{s} \equiv j^2$. The energy carried by any of the four particles in the *CMS* is equal to $E^\star = 1/2 \cdot \sqrt{\hat{s}}$. The elasticity z_c is defined as follows:

$$z_c \equiv \frac{P \cdot c}{P \cdot q} = \frac{E_P^\star E^\star - \vec{P^\star} \cdot \vec{c^\star}}{E_P^\star E^\star - \vec{P^\star} \cdot \vec{q^\star}} = \frac{E^\star - \mid \vec{c^\star} \mid \cos\theta^\star}{2E^\star} = \frac{E^\star - c_z^\star}{2E^\star} \ . \tag{2.8}$$

Since z_c is a Lorentz invariant, we can calculate it as well in the laboratory frame, where it can be reduced to

$$z_c = \frac{E_c - c_z}{E_\gamma - q_z} \equiv \frac{(E - p_z)_c}{(E - p_z)_\gamma} \ . \tag{2.9}$$

In the *CMS* we can further calculate

$$z_c(1-z_c) = \frac{E^{\star 2} - c_z^{\star 2}}{4E^{\star 2}} = \frac{m_c^2 + c_\perp^{\star\,2}}{\hat{s}} \,, \tag{2.10}$$

$$\Rightarrow \hat{s} = \frac{m_c^2 + c_\perp^{\star 2}}{z_c(1-z_c)} \,. \tag{2.11}$$

The four-momentum of the incident gluon is defined as $g = x_g P$. The four-momentum of the γ–*gluon* system can therefore be written as $j = x_g P + q$, and its invariant mass as

$$\hat{s} = x_g^2 P^2 + 2x_g P \cdot q + q^2 \approx 2x_g P \cdot q - Q^2 \,. \tag{2.12}$$

We have neglected the first term since $P^2 = m_P^2 \approx 0$ and $x_g \ll 1$. From this we derive

$$x_g^{LO} = \frac{Q^2}{2pq}\left(\frac{\hat{s}}{Q^2} + 1\right) = x_{Bj}\left(\frac{\hat{s}}{Q^2} + 1\right) \,. \tag{2.13}$$

Of course this calculation only holds in the case of leading order BGF. In addition, we cannot measure the charm quark momentum but only the resulting $D^\star$ kinematics. We therefore use the following approximation of z_c:

$$z_c \approx z_{D^\star} = \frac{(E-p_z)_{D^\star}}{(E-p_z)_\gamma} = \frac{(E-p_z)_{D^\star}}{2yE_e} \,. \tag{2.14}$$

The equivalence between $(E-p_z)_\gamma$ and $2yE_e$ follows from the definition of y given in Table 2.2 and will be extensively used in Chapter 4.3.2.

The transverse momentum of the charm quark in equation 2.11 must be approximated by the transverse momentum of the $D^\star$ meson in the γp CMS frame, $p_\perp^\star$. From the studies summarized in Table 2.3 we concluded that it is preferable to scale $p_\perp^\star$ by a factor $s = 1.2$. Therefore, x_g^{obs} is defined as

$$\hat{s}^{obs} = \frac{m_c^2 + (1.2 \cdot p_\perp^\star)^2}{z_{D^\star}(1-z_{D^\star})} \,, \tag{2.15}$$

$$x_g^{obs} = x_{Bj}\left(\frac{\hat{s}^{obs}}{Q^2} + 1\right) \,. \tag{2.16}$$

s	Mean	Width
1.0	-0.073	0.053
1.2	-0.008	0.052
1.4	0.051	0.082

Table 2.3: *Difference between* $log(x_g^{true})$ *and* $log(x_g^{obs})$ *for different values of the parameter s, determined using the program HVQDIS (see Section 2.3.5). The values shown for the mean and the width of the distributions are determined from a fit to a Gaussian distribution.*

2.3.4 The Monte Carlo generator AROMA

A leading order calculation of the *BGF* process is implemented in the program *AROMA* [21]. Higher order contributions are partly simulated by the parton shower model. This does not correspond to the full Next–to–Leading Order contributions. Therefore we have not used it for the extraction of the gluon density from the measurement. The program however incorporates a complete description of the hadronization step and generates all the particles found in the final state. This is achieved using the Lund string model. The resulting list of final state particles can subsequently be fed into a full simulation of the H1 detector.

For the present analysis, a *MC* simulation of H1 and the *AROMA* generator have been used to correct the data for detector inefficiencies, resolution effects and event losses due to the analysis cuts (see Sections 4.3.1, 4.4.1). Even though we know that this *LO* calculation describes the partonic processes only with limited accuracy, we may still use it to determine correction factors since the calculation reproduces all the important distributions of the data reasonably well and there is no significant indication that event losses in the data differ from those in the simulation (see Section 4.4.2).

2.3.5 A full NLO calculation of BGF

General remarks

A full *NLO* description of the *BGF* process has been made available through the program *HVQDIS* [27, 28]. It is a massive calculation which starts from a description of the proton containing u, d, s quarks and antiquarks and gluons only (*three flavor number scheme*). Renormalization of terms due to light quarks has been done using the $\overline{MS}$ scheme, divergences coming from heavy quark loops were subtracted at zero external momenta.

The program generates the final state charmed mesons using Peterson fragmentation. It does however not describe the entire final state of the event and can therefore not be linked to a full detector simulation. The program could therefore not be used to correct the measured data for detector effects. It however provides the information needed for the step from the measured cross section down to the parton level and to the extraction of the gluon density. To all 'events' generated by $HVQDIS$ weight factors are attributed, which may even be negative. These weights result from the numerical integration techniques used. Allowing additional NLO processes in the calculation may even reduce the predicted differential cross sections at some regions of the phase space. This reflects the canceling of contributions from real and virtual corrections.

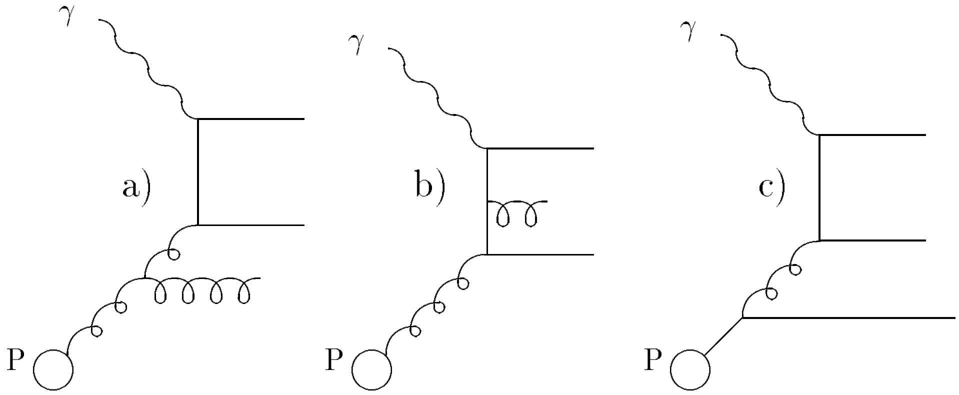

Figure 2.12: *Three examples of* NLO γ–gluon *fusion processes; the first two graphs lead to a distortion of* x_g^{obs}. *The third process is quark induced.*

The BGF process

Some of the NLO processes included in $HVQDIS$ are indicated in Figure 2.12. Besides different graphs with additional gluon emission and virtual loops, we also find a quark induced process. The latter is relatively unimportant and its contribution to the visible cross section can therefore be subtracted before the unfolding step.

HVQDIS was run using the *CTEQ4F3* [30] parametrization of the parton densities of the proton. The choice of this parametrization has been motivated by the fact that it is consistent with existing F_2 data and uses the *three flavor number scheme* used in *HVQDIS* as well. As a cross check, other parametrizations of the parton densities have been used. The charm quark mass has been set to a central value of 1.5 GeV/c^2 and was varied from 1.3 GeV/c^2 to 1.7 GeV/c^2 . This variation gives rise to the main systematic uncertainty of the measurement. Factorization and renormalization scales have been set to $\mu_f^2 = \mu_r^2 = 4{m_c}^2 + Q^2$. The program was run using $\alpha_s(M_Z) = 0.118$ [24] as described by $\Lambda^{(5)}_{QCD} = 225$ MeV , which is consistent with the *CTEQ4F3* parton densities.

Fragmentation

Fragmentation of the charm quark has been simulated using the Peterson model in the laboratory frame. Differences of the results using different values for the fragmentation parameter ϵ_c gave rise to an additional systematic error of the measurement (see Sections 2.3.2, 4.5). For the measurement of visible $D^\star$ cross sections the branching ratio $BR_{D^\star - K\pi\pi} = 0.0262 \pm 0.001$ [24] was used. For the final step down to the parton level and the gluon density, the best measured value of the overall branching ratio $BR_{c-K\pi\pi} = 0.0071 \pm 0.0005$ [32] was applied.

Chapter 3

The H1 Detector

3.1 The HERA storage ring

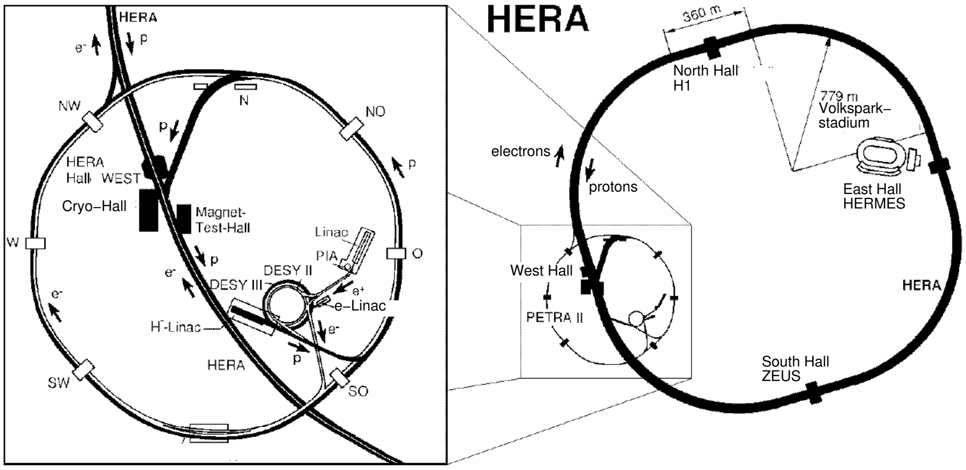

Figure 3.1: *Layout of HERA and its pre-accelerators PETRA, DESY and the Linacs*

The HERA (*Hadron Electron Ring Anlage*) particle collider at DESY (Hamburg) with its asymmetry is a unique machine: protons and positrons are circulated at high energies in opposite directions and brought to collision. This setup requires two independent accelerators built in one common tunnel. The energy of the positrons (or alternatively electrons) is limited by the strong increase in the synchrotron radiation power at highly relativistic velocities. The energy of the proton beam is limited by the strength of the magnets needed to bend the beam on its orbit. The HERA proton ring consists of superconducting magnets which produce a field of 4.6 T.

With a circumference of 6.3 km, HERA can store electrons or positrons at an energy of 27.5 and protons at 820 GeV. The currents of the beams have been increased from year to year, in 1995 when the data analyzed here were recorded, the machines were usually filled with $\approx$ 30 mA of positrons and $\approx$ 60 mA of protons. The lifetimes of the positron beams were around 8 h [1], the proton beam could in principle be kept for several hundred hours.

Two detectors, H1 and ZEUS, are built around the HERA collision points. The asymmetry between the colliding beams is reflected by the layout of the detectors: the ep system is strongly boosted in proton beam (*forward*) direction leading to a strong increase in particle multiplicities in forward direction. A third detector, HERMES, records the scattering of the polarized positron beam on polarized gas targets. In the fourth experimental hall, the HERA-B experiment is being built, aiming to measure CP violations in $B^0 - \bar{B}^0$ systems generated through collisions of beam protons with a wire target.

Both beams consist of 180 packages (*bunches*) containing in the order of a few times 10^{10} particles each, with a length of $\approx$ 110 (8) mm for the proton (positron) bunches. The width of both beams at the interaction–points is $\approx$ 0.18 mm and the height $\approx$ 0.05 mm. Every 96 ns two bunches intersect inside the H1 experiment. Due to the low cross sections for ep interactions, the rate of genuine events is below 1 kHz, much smaller than the rates for background processes such as collisions between beam protons and rest gas in the vacuum pipes, scattering of off–momentum protons or positrons on beam apertures or scattered synchrotron radiation from the positron beam. The HERA experiments therefore need to rely on sophisticated triggering systems, selecting the good events very quickly.

[1]Electron beams showed much shorter life times and were therefore not used at that period.

3.2 Overview of the experimental setup

The main subdetectors of H1 will be mentioned here, systems of special importance to the presented analysis are discussed in more detail in the following sections. The list is ordered according to the distance of the detectors to the interactio–point; numbers in the text refer to Figure 3.3. The term *forward* will be used for directions close to the proton beam direction, *backward* accordingly (see Figure 2.5 for the H1 coordinate system). A detailed description of the detector as of 1994 can be found in Reference [33].

- The central silicon detector (*CST*) has been designed to measure secondary vertices of heavy quark decays. In 1995 the *CST* was still being commissioned and could not be used for analysis. A second silicon detector, the *BST*, covers the backward direction and improves the measurement of the scattered positron.

- The central tracking system (2) is one of the main backbones of this analysis, see Section 3.4.

- The three modules of the forward tracker, (3), contain different drift and a double–layer of proportional chambers each. Tracks measured by the forward tracking system have not been used in this analysis. The first double–layer of the forward proportional chamber *(FPC)* is, together with the central proportional chambers, used by the *zVtx*–trigger.

- The main calorimeter is based on measuring the ionization due to particle showers in liquid argon. It starts with an electromagnetic section (4) where the *LAr* is filled between lead plates. The material in that section amounts to $20-30$ radiation lengths for positrons, their energies are therefore almost completely contained. In the hadronic part (5), the absorption of the particles is done by steel plates with a depth of $4.5-7$ absorption lengths. For this analysis, the *LAr* calorimeter has been used to measure the hadronic energy flow of the final state, needed to calculate the kinematical variables of the photon.

- The backward detectors (12) are mainly designed to measure the scattered positron. A drift chamber (*BDC*) is located in front of the calorimeter *SpaCal*. These detectors are of great importance to the present analysis and will be introduced in Section 3.5.

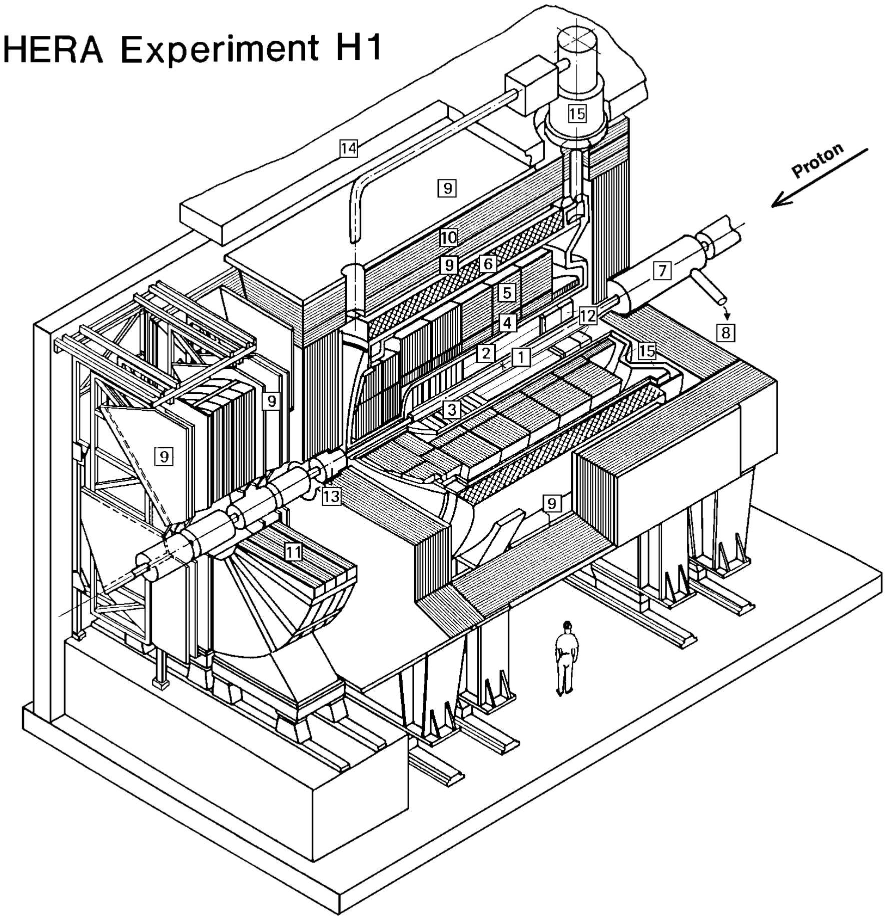

1	Beam pipe, interaction point	2	Central track detectors
3	Forward track detectors	4	*LAr* calorimeter, electromagnetic part
5	*LAr* calorimeter, hadronic part	6	Superconducting magnet coil
7	Compensator magnet	9	Muon chambers
10	Instrumented iron yoke	11	Forward toroid magnet
12	Backward calorimeter (*SpaCal*)	13	PLUG calorimeter
14	Concrete shielding	15	Liquid argon cryostat

Figure 3.2: *Overview of the H1 detector.*

- The superconducting magnet (6) generates a homogeneous field of 1.15 T, allowing the determination of the particle momenta through their curvature measured in the drift chambers. Disturbances of the beam induced by this magnetic field are compensated by an additional magnet (7).

- Energy leakage from the *LAr* calorimeter and high momentum muons which pass essentially unscattered through the detector are measured by streamer tubes installed between the plates of the iron yoke of the magnet and in forward direction (9,10).

- *ToF* (*Time–of–Flight*) scintillators are mounted around the beam pipe at both ends of the detector. Their timing information allows a powerful rejection of events originating from vertices outside the detector.

- The luminosity of the beams is measured using the Bethe-Heitler scattering process $ep \to ep\gamma$ with its well known cross section. Both, the scattered positron as well as the emitted photon, are measured by detectors installed around the positron beam downstream in the tunnel. The *electron tagger* is not only used for the luminosity determination, but also for measuring y in photoproduction events (see page 15).

- Detectors to measure protons and neutrons leaving the detector very close to the proton beam direction are installed in the tunnel.

Monte Carlo simulation of the detector

For the understanding of the data, it is of course vital to have a good description of the expected detector response. Simulation programs for the different physics processes produce lists of the long lived particles of the final state. The scattering and the absorption of these particles in the detector material is simulated using the *GEANT* [22] program. For the resulting tracks, the response of all subdetectors — drift and proportional chambers or calorimeters as well as the triggers — is calculated. The simulated events are then subjected to the same reconstruction and analysis procedure as the real data. Careful checks on the agreement of the simulation with the response of the real detectors are repeated regularly (see e. g. Figure A.4 and Reference [12]).

3.3 Triggering and data acquisition

The H1 trigger system used for the online selection of genuine *ep* collisions consists of four levels, denoted *L1* to *L4*. Only after an event has been accepted by all these four systems, it is written to tape and analyzed by the offline reconstruction computer (often referred to as fifth level, *L5*).

First trigger level

A priori every HERA bunch crossing could lead to *ep* interactions, i. e. a decision needs to be taken every 96 ns. During the evaluation of the trigger data, the full information of all subdetectors needs to be kept available in the according front–end electronics. The data acquisition (*DAQ*) system of H1 therefore starts with front–end buffers (*pipelines*) where all data recorded during the last 25 bunch crossings (2.4 μs) is stored. After this time the data is overwritten unless an '*L1 keep*' signal has been sent by the central *L1* trigger logics (*CTL*). If this signal appears, no new data is taken from the detector any longer, the pipelines are read out and the information transferred to the memories of the readout processors. Only after all subsystems have indicated that their front–end buffers have been read, the *CTL* removes the *L1 keep* signal and new detector data can be recorded. Since this reading of the pipelines introduces a deadtime of 1–2 ms, the *L1 keep* rate should not exceed 50 Hz in order to keep the primary deadtime below 5–10 %.

The *L1* trigger system consists of a series of independent subsystems, each of them based on the information of a specific subdetector, e. g. the *MWPC*, the *LAr* or the *ToF* system. Every one of these systems delivers a set of eight bits, called *trigger elements (TE)*, representing e. g. the signals of different *ToF* devices, or encoding the highest energy threshold exceeded in a calorimeter. In the *CTL* almost any logical combination of a total of 192 *TE* can be achieved through a combination of look–up–tables and coincidence gates. 128 different combinations, called *subtriggers (ST)*, can be formed in parallel. [34]

A subtrigger can contain information of any of the subsystems, e. g. it may be a combination of an energy deposition in the *SpaCal* in coincidence with the presence of track candidates in the *MWPC* and in the *CJC*, requiring in addition that no *out–of–time* signal has been detected by the *ToF*. Every subtrigger is designed to have maximal efficiency for a specific class of physics events while keeping the background rate as low as possible. The subtrigger just described as an example meets the needs of an analysis of $D^\star$ production in *DIS*, since it requires the positron being scattered into the *SpaCal* and at the same time requires tracks, possibly due to the decay products of the $D^\star$. This combination of *TE* from completely independent systems is very stable against background [44]. The timing vetos help to reject fake events triggered by upstream proton interactions.

The following list of *L1* trigger subsystems is not complete, but contains all the subsystems of importance for the present analysis:

- The *SpaCal IET*–trigger will be explained in a few details in Section 3.5 .

- The *zVtx*–trigger is based on signals from the multiwire proportional chambers *(MWPC)*. As every particle track in the central rapidity region passes through at least four layers of *MWPC*, track candidates *(rays)* can be formed from the chamber signals and allow a fast determination of the event vertex. All the rays corresponding to real tracks have a common vertex, whereas the origins of rays formed by random coincidences are distributed along the z-axis. The *zVtx*–trigger allows a reliable assignment of the event to its HERA bunch crossing. Different trigger elements are derived from the rays:

  - t_0: At least one ray fired.
  - σ: Significance criteria, based on the number of rays from a common vertex compared to the total number of active rays.
  - *Multiplicity*: Encoding of the total number of active rays.
  - *Cluster*: The origins of all active rays are not more than $\approx$ 20 cm apart from each other.

  The *zVtx* trigger has been discussed in detail in [12, 69], some additional technical details will be given in Appendix A.

- The $r\phi$–trigger uses the signals of the *Central Jet Chamber CJC* (see Section 3.4). Parallel to the readout chain, the *CJC* signals are discriminated for triggering purposes. Track candidates are formed from the signals of seven layers of wires in *CJC* 1 and three layers in *CJC* 2. Since the drift times in the *CJC* extend up to $\approx$ 1 μs, the signals reach the input of the $r\phi$–trigger electronics at different times. Their combination is achieved by feeding them into shift–registers and applying masks requiring coincidences between signals at different steps in the registers. [35]

The $r\phi$–trigger elements count the number of track candidates with a transverse momentum above 400 MeV/c *(thresholds a,b,c)*. The *TE threshold high* is released by tracks with $p_\perp > 800$ MeV/c, *threshold low* is efficient for tracks with 400 MeV/c $< p_\perp <$ 800 MeV/c.

- *SpaCal Time–of–Flight* information is available from the electromagnetic as well as from the hadronic section. These vetos are very powerful in rejecting upstream interactions of the protons with the gas and the beam pipe. Secondary particles from these sources arrive with a different phase relative to the HERA bunches in the *SpaCal* compared to particles from an *ep* interaction. The *SpaCal ToF* however cannot reject upstream background from protons with a wrong beam timing (*satellite bunches*).

- Similar to the $r\phi$–trigger, the rz–trigger scans the hits of the z–drift chambers *CIZ* and *COZ* for possible track candidates. Only the *rz upstream veto* has been used in the subtriggers of importance here. Based on *CIZ* hits, track candidates originating from upstream vertices (proton–gas interactions) release a veto. The veto is however not set if at the same time the rz–trigger logics detect a vertex candidate at the nominal place.

- The *CIP backward veto* rejects events with high track multiplicities in the rearmost quarter of the inner proportional chamber. This *TE* helps to reduce upstream background, no matter whether it originates from the main proton bunches or from the out of time satellites. The veto however shows some inefficiencies for physics events with large hadronic activity in the backward direction (high y). It has therefore been suggested to replace it by new electronics which use the angular information that can be gained from comparing the two layers of *CIP* [36].

Second and third trigger level

For the intermediate trigger levels, a dedicated readout system has been built, collecting the most important information from the subsystem triggers. The *L2* triggers are able to combine tracking and calorimetric information locally. This allows a much more specific use of the information than the combination of trigger elements on *L1*. The *Topological Trigger (L2TT)* [37] and a system using *Neural Networks (L2NN)* [38] work in parallel, calculating different *L2 trigger elements* each. Every *L2 TE* acts on a well defined set of *L1* subtriggers only, reducing their rate heavily while retaining high efficiency for the selected physics processes. Many *L1* subtriggers — for instance the one used for this analysis — have no *L2* requirement at all. The *L2* decision is calculated during the first 20 μs after the *L1 keep* signal. If this decision is negative, the readout is aborted and the data taking is resumed immediately. *L1* subtriggers with an *L2* condition may therefore run with up to a few hundred Hertz.

The level 3 trigger has not yet been used.

Level 4

The fourth trigger level consists of an array of processors which have access to the entire event information after being collected from the subsystems by the central event builder. Data is not written to tape before the *L4* step, which therefore runs parallel to the data taking. A fast version of the reconstruction software allows to apply relatively tight cuts on physical quantities such as invariant masses or the identification of the scattered positron. Until 1996, the philosophy of the *L4* programming was to reject non-*ep* background [39], for data taken from 1997 on, the higher luminosities reached in HERA forced to reject a part of the *ep* events as well [40]. This rejection should of course only affect physics classes where sufficiently large event samples are already recorded — a $D^{\star}$ finder therefore protects candidates in different decay channels from being rejected [14].

In addition, *L4* allows the online monitoring of the performance of all subdetectors.

Level 5

Only very few events are rejected at the final reconstruction step. The reconstruction is repeated, using the full version of the programs and calibration constants which were updated on the *L4* step. The same $D^{\star}$ selection procedure as on *L4* is perfomed on *L5* with slightly tightened cuts, flagging all candidates which are then written to the *Data Summary Tapes, DST*[2], which can then be accessed for analysis.

[2]In fact the data volume of the *DSTs* is reduced so far that it can be kept available on harddiscs.

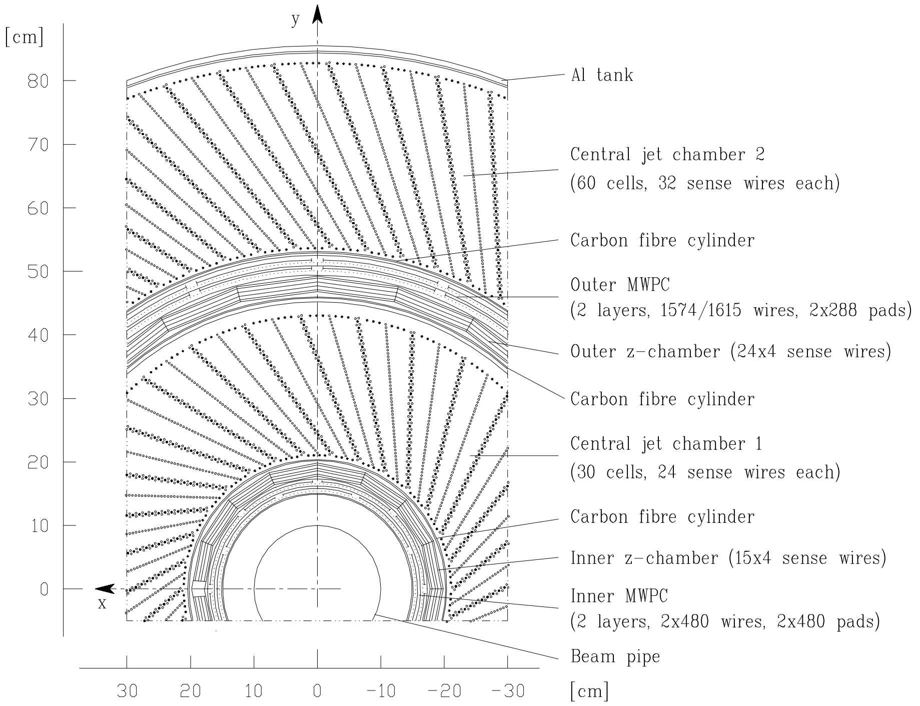

Figure 3.3: *Cut perpendicular to the beam direction through the central tracking system.*

3.4 The central tracking system

The central tracking system consists of several cylindrical drift and proportional chambers fitting into each other. The main pattern is repeated twice:

- Proportional chambers (*MWPC*), *CIP* (*Central Inner Proportional chamber*) starting at a radius of 150 mm and *COP* at $\approx$ 500 mm. Both chambers consist of an inner and an outer layer. The cathodes of *CIP (COP)* are 8- (16-) fold segmented in ϕ with 60 (18) pads along the z-axis. The signals from these pads are read out and used by the *zVtx*–trigger.

- The main tracking devices are the two volumes of the *CJC (Central Jet Chambers)* . With wires parallel to the beam they allow an optimal measurement of the $r\phi$ projection of the particle tracks. For single hits, resolutions of $\approx$ 170 μm in the $r\phi$ projection have been achieved. The

CJC has been designed to measure charged particle momenta at an accuracy of $\sigma_p/p^2 \approx 3 \times 10^{-3}$ GeV^{-1}.

- Two thin drift chambers with wires strung around the beam achieve an accurate measurement of the z–position of the tracks *(CIZ and COZ)*. The resolution of the z–chambers is typically 300 μm. *COZ* suffered in 1995 from high voltage instabilities, the z-hit information has therefore not explicitly been required in the analysis.

All drift chambers are read out by *Flash ADCs*, digitizing the signals at ten times the HERA bunch crossing frequency, i. e. 104 MHz with a resolution of eight bits. Both ends of the wires are read out, allowing a rough determination of z *(ϕ)* in *CJC (CIZ, COZ)* of about 1 % (2–2.5 %) of the wire lengths. This additional information is needed for the first step of the reconstruction (done with *CJC* information only) as well as for the linking of the hits of the z chambers to the *CJC* tracks. (A short description of the track finding is given in Section 4.4.1.)

3.5 The backward detectors

The backward region of the H1 detector has been upgraded with entirely new detectors during the shutdown 1994/95. These devices were explicitly designed for the needs of *DIS* analyses and will shortly be described here (see References [41, 61] for more details).

- The energy of the scattered positron is measured by the first section of the *SpaCal* calorimeter. Its name *Spaghetti Calorimeter* reflects the physical layout with scintillating fibers of 0.5 mm diameter inserted into the absorbing lead. The electromagnetic *SpaCal* is divided into 1192 cells of 4.05 $\times$ 4.05 cm^2 area with an active depth of 25.0 cm. It extends from an inner radius of 6.5 cm out to 80.0 cm with a slightly more restricted fiducial region for the measurement. The energy resolution for positrons (σ_E/E) is $7.5\%/\sqrt{E[\mathrm{GeV}]} \oplus 2\%$ [42], the energy scale has been determined to 0.7% at 27.5 GeV [3]. The spatial resolution is $\approx$ 3.5 mm, the timing of the signals can be measured with an accuracy of about one nanosecond.

[3] We have to quote a larger uncertainty in this analysis because the final calibration has only been achieved after the data analyzed here have been recorded, see also Appendix C.

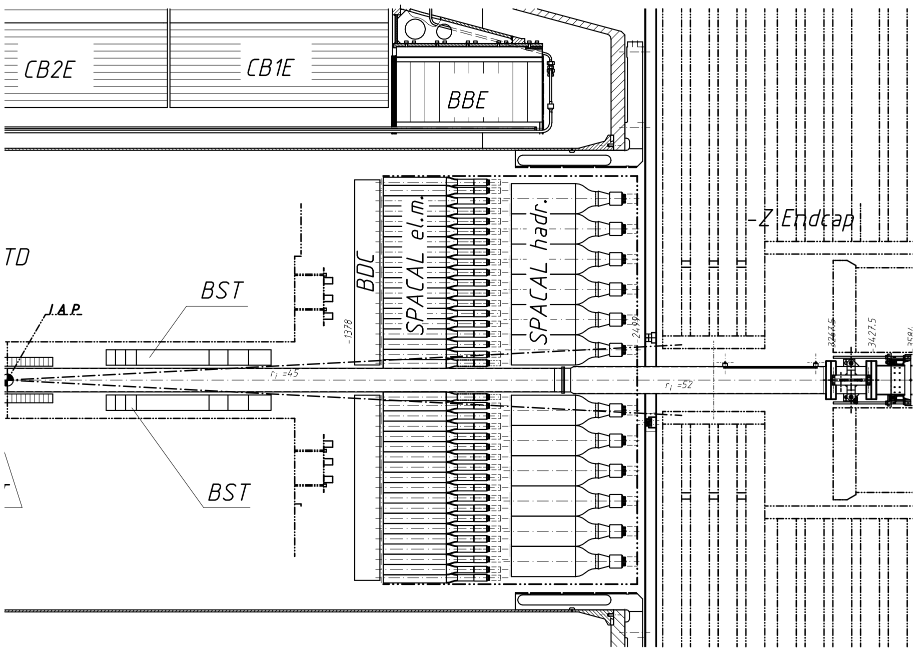

Figure 3.4: *Side view of the backward detectors* BDC *and* SpaCal.

The *Inclusive Electron–Trigger (IET)* of *SpaCal* is designed to reach highest efficiency for detecting the scattered positron. 320 arrays of 4×4 cells (*IET windows*) are defined. The centers of the windows are shifted by two cells with respect to each other, the resulting overlap *(sliding windows)* guarantees that — no matter where it enters the *SpaCal* — the shower of a positron is well contained in one of the *IET* windows. The *IET*–trigger element is released if the energy in one window exceeds a given threshold and if the timing is consistent with an *ep* interaction. Three different thresholds are available. [43]

- The hadronic section of *SpaCal* has a structure similar to the electromagnetic one with coarser granularity and a thickness corresponding to about one hadronic interaction length. The hadronic energy measurement with *SpaCal* is rather important, since in the sum $\sum_i (E-p_z)_i$ the particle energies are weighted with a factor of $(1-\cos\theta_i)$, i. e. the more backward the energy is deposited, the more in contributes.

This sum is used to reconstruct the kinematics of the scattering process (see Section 4.3.2).

- The *Backward Drift Chamber (BDC)* is mounted in front of *SpaCal*. It consists of four thin double-layers with wires strung octagonally around the beam axis. For radii smaller than ≈ 23 cm the drift distances extend up to 0.5 cm, for larger radii their range is increased to up to 1.5 cm. The *BDC* is designed to
  - improve the measurement of the positron scattering angle θ_e to $\mathcal{O}(0.5\ \mathrm{mrad})$ [61];
  - allow to recognize photons faking a positron in the *SpaCal* by tagging electromagnetic showers with no associated charged particle track;
  - allow a correction for energy losses of the positron due to showering in the dead material between interaction point and *SpaCal*.

Chapter 4

Cross Section Measurement

In the present analysis, charm production has been tagged through the reconstruction of the invariant mass of $D^{\star\pm}$ mesons in the decay channel $D^{\star +} \to D^0 {\pi_s}^+ \to (K^-\pi^+){\pi_s}^+$ (+ charge conjugate). Due to the small mass difference between $D^\star$ and D^0, the emitted pion has a very low momentum in the $D^\star$ system and carries typically less than 10 % of the $D^\star$ momentum in the laboratory frame (Figure 4.2 a)). The subscript indicates this slow or soft property. The particles from the D^0 decay have typically much higher momenta in the laboratory frame. Uncertainties of the reconstruction of the particle momenta cancel to a large extent, if we inspect the mass difference Δm between the $D^\star$ and the D^0 rather than the reconstructed $D^\star$ mass itself.

The kinematics of the photon can be reconstructed from the scattered positron alone *(electron method)* or using information of the entire hadronic final state as well *(eΣ method)*. The electron method has very good accuracy at large values of y. The $e\Sigma$ method has the advantage of nearly constant resolution over the entire kinematical range considered here and requires only small corrections due to additional radiation from the positron.

The kinematics of the selected final state restrict the accessible range of the gluon momentum to $-3.125 < log(x_g^{obs}) < -1.625$ as can be seen in Figure 4.1 . Figures 4.2 b) - d) show correlations between the properties of the photon or the scattered positron and the $D^\star$ meson. From Figures 4.2 b) and c) we may conclude that a good fraction of the $p_\perp^{D^\star}$ originates from the recoil of the positron.

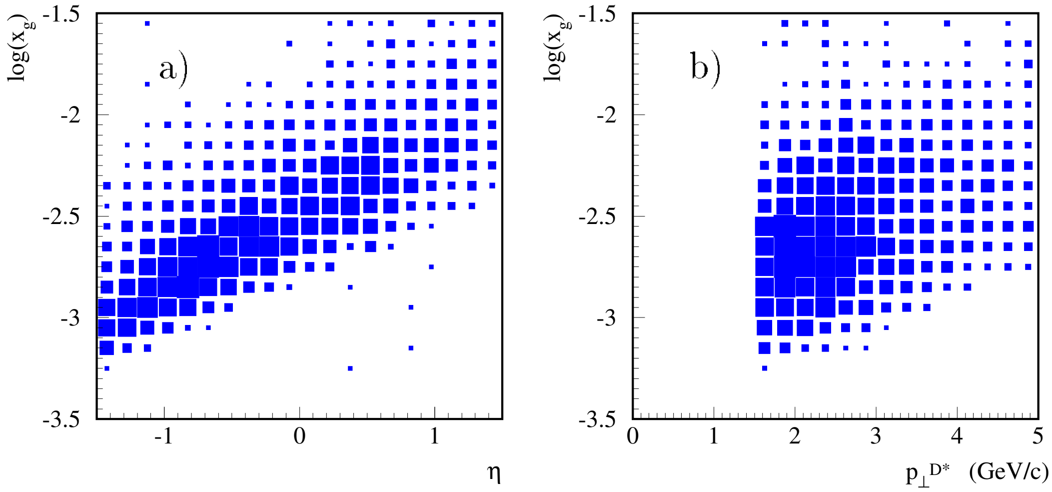

Figure 4.1: *Correlation between different kinematical variables as predicted by the AROMA simulation (part I). a) Events with high x_g are boosted in the proton direction ($\eta_{D^\star} > 0$). b) Increasing x_g means increasing center–of–mass energy of the hard partonic system and is therefore correlated to increasing momentum of the $D^\star$.*

4.1 Definition of the visible cross section

Due to the geometrical acceptance of the detector, the cross section could only be measured in a restricted kinematical range. We chose not to extrapolate to the full phase space, but rather to compare the measured cross sections to theoretical predictions constrained accordingly. The four cuts defining our visible range are listed below. Event losses due to all the additional cuts are explained in Sections 4.3.1 , 4.4.1 and have been corrected for.

- The pseudorapidity η of the $D^\star$ candidate is required to be $-1.5 \leq \eta \leq 1.5$. This cut corresponds to the limitation in the polar angle of the central tracking chambers of H1.

- The transverse momentum of the $D^\star$ candidate must be greater than 1.5 GeV/c. This cut suppresses combinatorial background of low $p_\perp$ tracks and eliminates π_s candidates with a very low $p_\perp$.

- The range in momentum transfer has been chosen to be 2 GeV$^2 \leq Q^2 \leq$100 GeV^2. This corresponds to the angular acceptance

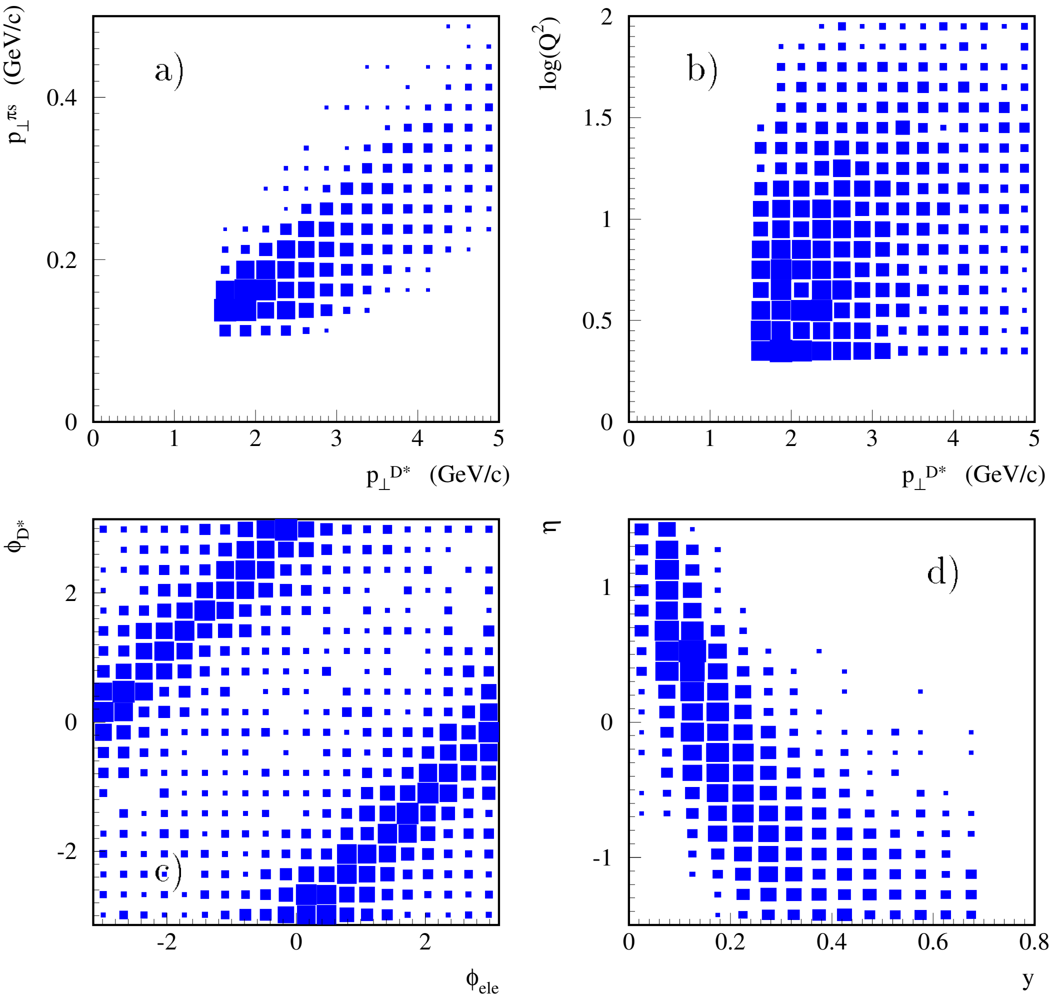

Figure 4.2: *Correlation between different kinematical variables as predicted by the AROMA simulation (part II). a) the slow pion carries typically less than* 10% *of the* $D^\star$ *transverse momentum. Correlations between the scattered positron and the* $D^\star$*: b)* $p_\perp^{D^\star}$ *increases slightly with increasing* Q^2*. c) The back–to–back configuration in the plane perpendicular to the beams can be seen as a strong correlation between the azimuthal angles of the scattered electron and the* $D^\star$ *meson. d) Low values of* y *mean that the photon carries only little longitudinal momentum and therefore the* $D^\star$ *goes predominantly in forward direction, i. e.* $\eta_{D^\star} > 0$ *whereas high* y *events are rather boosted in the backward direction.*

of the *SpaCal* and tracks to a mean Q^2 of 15 GeV^2 . In this range, the used NLO calculation is expected to be reliable.

- In order to guarantee an accurate measurement of the DIS kinematics and to suppress background, y was limited to $0.01 \leq y \leq 0.7$ for the Σ and the $e\Sigma$ method. For the electron method, the lower cutoff had to be raised to 0.05 (see Sections 4.3.1, 4.3.2).

4.2 Event selection

4.2.1 Run selections

Runs were selected for this analysis only if all subdetectors used were at nominal voltage (CJC, BDC, CIP, COP, liquid argon calorimeter, SpaCal, luminosity–system and veto–counters). If detectors are missing for part of a run only (e. g. HV–trips in track detectors), the luminosity of that run is scaled accordingly. In addition, runs with known hardware problems of some subdetectors have been excluded from the analysis:

- A special run selection was needed for the *SpaCal*. Especially at the beginning of 95 the detector was still commissioned. A selection routine [41] rejects most of the bad runs. This procedure guarantees
  - a valid calibration by requiring the mean energy of the positron candidates to be within 1σ around the nominal value.
  - operating trigger electronics by requiring the number of selected events per luminosity to be in a reasonable range.

  Both requirements are applied to a sample of inclusive DIS events. A minimal luminosity per run is required to guarantee a statistical significance of these criteria.

- For the $r\phi$–trigger a few runs had to be excluded from the analysis because of malfunction [47].

- Some runs were rejected because the response of the $zVtx$–trigger electronics did not match with what was expected, as explained in Section A.1.7 .

The selected subtriggers have seen a total luminosity of 3.68 pb^{-1} in 1995. After requiring the correct high voltages, 2.95 pb^{-1} was left[1], 2.42 pb^{-1} survived the *SpaCal* run selection, and lastly, when runs with known hardware problems are excluded, 2.40 pb^{-1} remain for the use in the analysis.

4.2.2 Trigger efficiencies

Trigger strategy in 1995

DIS events are selected on the first trigger level through the signal of the scattered positron in the *SpaCal IET*–trigger (see Section 3.5). During the 95 data taking, the trigger rates have often been saturated by minimum bias triggers based on the *SpaCal* alone. The reason for these high rates could never be traced completely. The high rates were concentrated in an isolated area (*Hot Spot*). They are related to the positron beam but could not be explained by synchrotron radiation. The definition of the subtrigger used in this analysis had therefore been changed several times in order to improve the running conditions. Efficiency losses due to different triggering conditions are weighted with the affected luminosity. Table 4.1 lists the efficiencies of all trigger elements used and the percentage of luminosity affected by these.

Trigger strategy in 1996

The subtriggers of 1995 were tightened with independent trigger elements such as the *zVtx*–*t*0 and an $r\phi$–trigger condition for the 96 data taking. A scenario based on two different subtriggers has been proposed in Reference [44].

- Subtrigger 1 (*ST_1*) was designed as minimum bias trigger. It uses only the weak *t*0 condition of the *zVtx*–trigger and the $r\phi$–trigger. A veto based on the *zVtx*–trigger has been applied to *ST_1* in order to suppress background originating from protons interacting upstream of the detector with gas or beam line material. This sort of background should in principle already be rejected by the timing vetos from the *SpaCal*. However protons with incorrect beam timing (*late*

[1]This difference is not only due to occasional trips of the tracking chambers, but can to a large extent be explained by the fact that the luminosity measurement starts immediately after the beams are at full energy whereas the trackers can only be switched on after the fine tuning of the beam optics has been finished.

trigger element	efficiency	affected luminosity	total event loss
IET	99.2%	100.0%	0.80%
SpaCal hadronic AToF	99.8%	75.0%	0.17%
SpaCal electromagnetic AToF	98 – 100%	1.0%	0.02%
rz (σ*_1* ‖!*non_vtx*)	99.4%	24.0%	0.15%
zVtx t0 from MC	100.0%	74.0%	0.45%
zVtx t0 from data	99.1%		
$r\phi$*_ta from MC*	98.8%	24.0%	0.20%
$r\phi$*_ta from data*	99.7%		
Total			$1.8^{+5.0}_{-1.8}$%

Table 4.1: *Trigger efficiencies as determined for the 95 data and percentage of data affected by these conditions. The errors of the values are large and the differences between data and* MC *for the track triggers are not significant. The large uncertainty on the total trigger efficiency has been dictated by the work going on on the* IET*–trigger during the data taking.*

satellite bunches) arrive just at the nominal time at these veto layers and are therefore accepted. Due to the huge amount of dead material between their vertex and the trackers, these events cause an enormous number of hits in the drift and proportional chambers and considerable deadtime. The *zVtx*–trigger veto rejects big events, with a sum of more than 250 entries in the histogram and saves first level readout time (see Section A.1.4).

To make the *ST_*1 condition robust against positron beam related background, an area around the beam pipe has been excluded from the *IET*–trigger. This area lies asymmetrically around the beam and covers the region where the rate was highest in 95. The resulting radial cutoff corresponds to a cut against the low Q^2 region where the statistics of the inclusive F_2 measurements was already high and no further data were needed. For our analysis, *ST_*1 was used as a monitor trigger for the tight track conditions imposed on subtrigger 2 .

- Subtrigger 2 (ST_2) was designed for the needs of heavy quark physics. These analyses were still limited by statistics, even at low Q^2. Therefore the entire acceptance of the *SpaCal* was used for ST_2, suppressing the background mainly with the tight track requirements $r\phi$–t_high and $zVtx$–σ_1.

For both subtriggers timing vetos based on the electromagnetic and the hadronic section of the *SpaCal* have been applied. Further timing vetos were based on smaller scintillators around the beam pipe on both sides of the experiment *(FToF & BToF)*.

SpaCal inclusive electron trigger

The energy threshold used in our subtriggers has been adjusted to 6.5 GeV and it was therefore expected to be fully efficient at 8 GeV, the cutoff applied offline in the analysis. For the 96 running, the threshold was adjusted even lower, which has been checked using independent subtriggers, mostly based on energy deposition of the hadronic final state in the *LAr*–calorimeter. No significant inefficiency could be found. For the data collected in 95, no completely independent subtrigger with sufficient statistics could be used. The energy dependence of the trigger could only be checked using events from a subtrigger based on a lower threshold of the *IET*–trigger (see Figure 4.3). This however leaves us with the uncertainty whether events are lost for all energy thresholds due to malfunction or miscalibration of the electronics. Since we used the entire statistics of the 95 running period, including the early periods where most of the fine tuning on the electronics was still going on, we added an additional uncertainty of 5% to the trigger efficiency [46]. This value can be considered as quite conservative, since runs with complete malfunction of the *IET*–trigger would have been discovered by the *SpaCal* run selection, wrong calibrations of the trigger input would have shown up in the efficiency curves.

zVtx–trigger

In 95 only the weak $zVtx$–$t0$ condition has been used in *DIS* triggers. The efficiency could be checked for the very first run periods using the *SpaCal* stand–alone trigger. It exceeds 99% which is in good agreement with the Monte Carlo description.

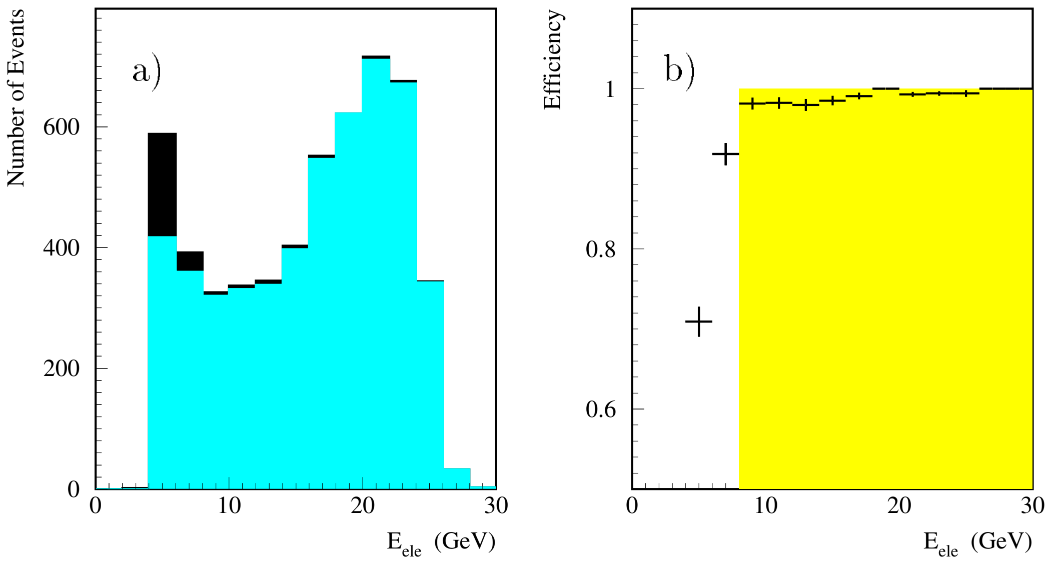

Figure 4.3: *Evaluation of the inclusive electron trigger efficiency a) Number of events selected in 95 by a lower energy threshold trigger of the* SpaCal. *In black are all events, in light grey those which would also have been triggered by our analysis subtrigger. The cuts on the $D^\star$ candidate have been opened, those on the positron (see Section 4.3.1) are standard. The increase of the number of events below* 7 GeV *indicates that fake positrons from photoproduction events enter in the statistics here. b) Trigger efficiency as a function of the measured energy of the scattered positron. The grey area indicates the desired 100% efficiency in the range analyzed.*

For the 1996 and 97 running periods the $zVtx$–trigger condition for $D^\star$ in DIS events has been iteratively optimized (see Section A.1.3 for more details).

$r\phi$–trigger

Changing criteria from the $r\phi$–trigger have been applied to the subtrigger used. These requirements are quite powerful in the rejection of electron beam related background. The efficiency for $D^\star$ events is very high since at least two high momentum tracks in the CJC are required for the offline reconstruction of the D^0 anyway. Additional tracks are usually present in the events, any of them may set the $r\phi$–trigger. The efficiency of the $r\phi$–trigger has been determined with both data and Monte Carlo. Both methods were in agreement within the available statistics and show an efficiency of $\approx 99\%$.

rz –trigger

The rz–trigger provides a veto against upstream proton background. It is based on track segments found in *CIZ* and *COZ* pointing to a vertex far from the nominal interaction region. This veto is not effective, if at the same time the rz–trigger vertex histogram shows a significant peak. For standard running, the losses due to this veto condition are minimal. The setup however failed in case of HV–trips in *CIZ* or *COZ*. A non negligible number of good ep events was rejected in these cases [45]. The inefficiency could however be determined from data, using an independent subtrigger in those run periods, where the rz veto was applied to the production trigger.

Timing vetos

The timing of the vetos based on both the electromagnetic and the hadronic sections of *SpaCal* has only been finally adjusted during the 95 data taking. It has therefore been necessary to estimate the number of events lost before these vetos were optimized. Especially the *AToF* condition derived from the hadronic *SpaCal* has been rejecting good events, in particular high y events, in which more final state particles head backwards into *SpaCal*. The total event loss has therefore been determined by a sample of independently triggered events, where statistical weights have been applied in order to reproduce the y distribution of the $D^\star$ sample.

4.3 Reconstructing DIS kinematics

4.3.1 Positron selection and photoproduction background

The selection of good positron candidates is the major criterion used to distinguish *DIS* from photoproduction (γp) events. Due to the much higher cross section for γp interactions at $Q^2 \approx 0$ we are very sensitive to misidentification of particles from the hadronic final state of γp events faking a scattered positron in the *SpaCal*. Several cuts on the data help to reduce this misidentification probability [10]. Further cuts are dictated by detector geometry.

- The scattering angle is required to be $153° \leq \theta_e \leq 177°$. This cut still covers the full range in Q^2 which defines the visible range (see Section 4.1).

- The distance r_{BDC} of the positron impact point to the beam axis is required to be larger than 8.7 cm. At smaller radii parts of the electromagnetic shower may leak out of the *SpaCal* and lead to incorrect measurement of both energy and position of the cluster. This cut is largely contained in the cut on θ_e. It is only important for events with a vertex relatively close to the *SpaCal*.

- Only positron candidates with an energy greater than 8 GeV are selected. This already reduces the probability that other particles fake a positron simply because there are almost no hadronic particles going backwards at these high energies. This cut corresponds approximately to the cut $y \leq 0.7$.

- The radius of the energy cluster in the *SpaCal* ($r_{cluster}$) is required to be less than 3.5 cm. Hadronic particles tend to spread their energy in a wider area.

- The distance Δ_{BDC} from the center of the energy cluster to the closest track in the *BDC* is required to be less than 2.5 cm. This cut mainly suppresses the misidentification of photons (e. g. from π^0 decays). The position of the track in the *BDC* is used for the calculation of the scattering angle θ_e of the positron.

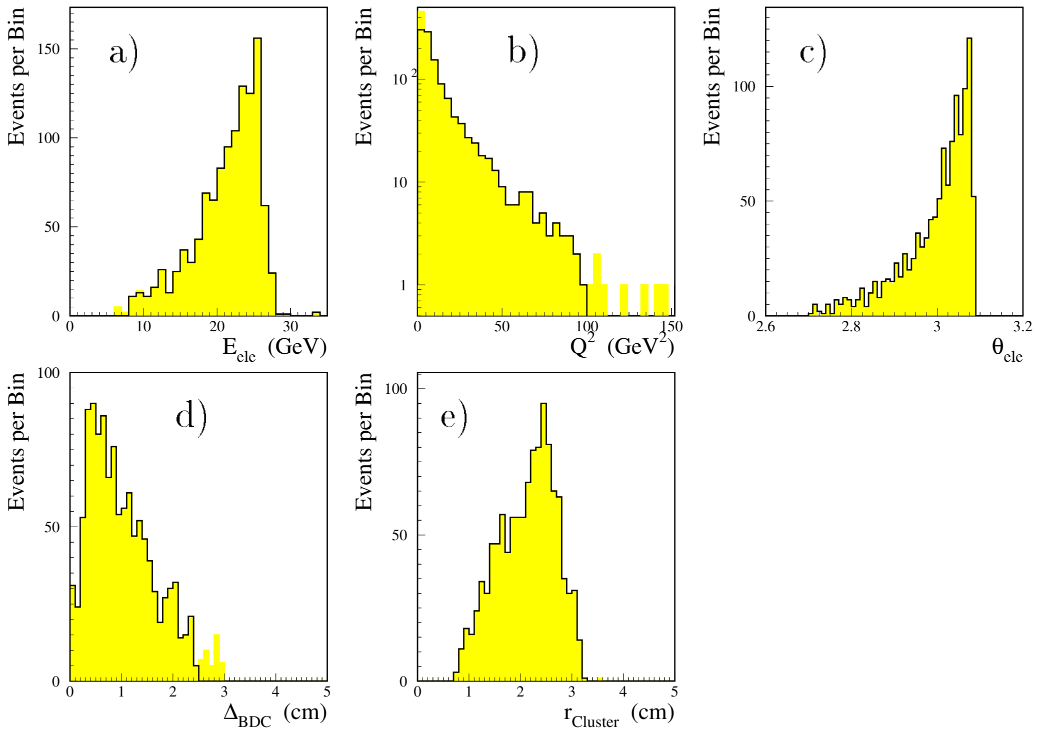

Figure 4.4: *Positron selection control plots: Distribution of* $E_{e'}$, Q^2, θ_e, Δ_{BDC} *and* $r_{cluster}$. *The solid line shows the standard selection of positron candidates. For the grey histogram, the cut on the plotted variable has been removed.*

- The cut on $z_{D^\star}$ has originally been introduced to suppress combinatorial background in the Δm–distribution (see Section 4.4.1). It has, as a positive side-effect, suppressed the number of events at low $E_{e'}$ and clearly helped against γp background.

The control plots in Figure 4.4 exhibit a smooth behavior of the distributions in the region of the cuts and indicate, that only few events are rejected.

No cut has been applied to the value of $(E - P_z)_{all}$ in the events. The sum defining this quantity extends over all particles in the final state, including the positron candidate:

$$\Delta \equiv (E - P_z)_{all} = \sum_{all\ particles} E_i - P_{zi} \ .$$

Usually all the central detectors (central trackers, *LAr*–calorimeter and *SpaCal*) are used. Δ is a conserved quantity and can be calculated from the initial state. Neglecting the proton rest mass, we expect Δ to be twice the energy of the positron beam, i. e. 55 GeV. Any deviations from this value indicate – apart from uncertainties of the energy and momentum measurements – losses of particles in the backward direction[2]. Events with initial state radiation (see Section 4.3.3) appear at $2 \times (E_e - E_{\gamma initial})$, where $E_{\gamma initial}$ is the energy of the emitted photon. For photoproduction events the scattered positron is not included in the sum since it escapes through the beam hole in the *SpaCal*. Δ is thus expected to be $2 \times (E_e - E_{e'})$. For the inclusive F_2 measurement [10] a cut of $\Delta \geq$35 GeV has been applied. As can be seen from Figure 4.5 a) no such cut was necessary for the $D^\star$ analysis as there are no events below the cut value.

A certain number of the selected events still showed an energy deposition in the electron tagger. This energy does however not come from photoproduction of charm, but rather from well measured *DIS* events overlapping with *Bethe–Heitler ep* scattering. This can be seen if we add for these events the contribution of the e-tagger to the Δ value (see Figure 4.5 a) full black histogram). The shift to values exceeding 55 GeV can only be explained by the fact that a second positron contributes. Since only the second positron, but not the emitted photon has been included in the total sum, it is still less than $2 \times 2 \times E_e$. The *Bethe – Heitler* process does not lead to $D^\star$ production and hence these events can be considered as good *DIS* γ*–gluon* fusion events.

The positron selection cuts have also been applied to samples of simulated $D^\star$ events from direct and resolved photoproduction. No event survived the imposed cuts.

4.3.2 Reconstruction of the kinematical variables

The determination of $log(x_g^{obs})$ requires a measurement of the $D^\star$ and the photon. Here we start with the variables x_{Bj}, y and Q^2. Since we measure angle and energy of both the scattered positron and the hadronic final state, the reconstruction of the kinematics is overconstrained, because in principle only two of these four quantities are needed. Some of the methods discussed

[2]Particles lost very close to the proton beam direction do not contribute since the lost energy is very well compensated by the lost longitudinal momentum.

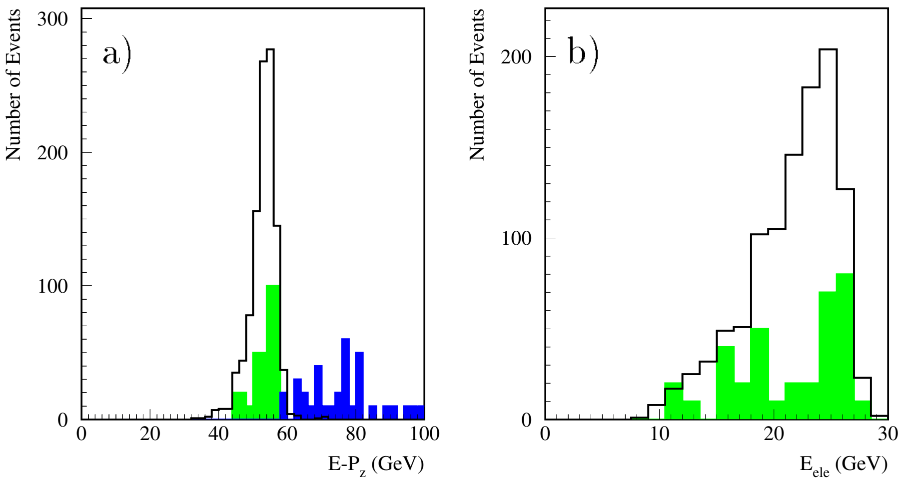

Figure 4.5: *a) Values of Δ as measured in 95 data. The solid line shows the entire dataset. The light grey area gives – enlarged by a factor of 10 – the values measured by the central detectors for events with energy deposited in the electron tagger. The black histogram shows these tagged events, if the energy measured by the tagger is included in the sum defining Δ. The values are clearly above 55 GeV then, which indicates that we observe the overlap of two ep interactions (see text). b) Energy spectrum measured by the* SpaCal *for all (solid line) and for the tagged events (grey histogram, enlarged by a factor of 10). The presence of an elastic peak in the tagged sample shows, that the positron candidates of these events are real DIS positrons.*

below use more than two variables in order to reach maximum accuracy over the entire kinematical range [48, 49].

- The *electron method* completely ignores the hadronic final state. It uses only the angle and the energy of the scattered positron.

- The Σ *method* is based on the energy flow of the final state and the scattering angle of the positron.

- The $e\Sigma$ *method* is a mixture between electron and Σ method.

- The *hadron method* is similar to the Σ method, however it uses the transverse momenta of the hadronic final state instead of the transverse momentum of the scattered positron. It is not used because of its inferior resolution.

- The *double angle method* starts from the measured polar angles of the scattered positron and of the struck quark. This method has a good resolution only at values of Q^2 much higher than selected for this analysis. It is therefore not used in the following.

The first three methods have been studied in detail for this analysis. They will be described in the following. The formulae used are listed in Table 4.3.2. The $e\Sigma$ method has been chosen for the final analysis; the electron– and Σ methods have been used for cross checks only.

The methods using the hadronic final state are essentially based on the value of $(E - P_z)_{all}$ as introduced before. Let us again define the following quantities of the final state:

$$\Delta = (E - P_z)_{all} = \sum_{all\ particles} E - P_z \ , \tag{4.1}$$

$$\Sigma = (E - P_z)_{hadrons} = \sum_{all\ hadrons} E - P_z \ . \tag{4.2}$$

The two values differ by the contribution of the positron to Δ:

$$\Delta = \Sigma + E_{e'} \times (1 - \cos(\theta_e)) \ . \tag{4.3}$$

It is obvious that the definition of these quantities is related to the scalar products $q \cdot P$ and $p \cdot P$ which occur in the definitions of y and x_{Bj} (see Section 2.2).

For the experimental measurement of Σ different methods have been tested. Best results are obtained with the simultaneous use of all available detector components, trackers and calorimeters. If a well measured track is found in the central or forward tracking system, the contribution to Σ of this particle is calculated from the measured momentum and polar angle of the track. The energy measured in the calorimeter cells around the impact point of the track is ignored in order to avoid double counting. If energy depositions without a corresponding track are found, the contribution to Σ is calculated from the measured energy. This combination is often called *'cells and tracks'*.

The electron method

This method is based on the measured positron candidate only, therefore straightforward to use. It depends however drastically on the good calibration

Method	y	Q^2	x_{Bj}
electron	$1-\frac{E_e}{E_{e'}}\sin^2(\frac{\theta_e}{2})$	$4E_{e'}E_e\cos^2(\frac{\theta_e}{2})$	$\frac{Q_e^2}{y_e \cdot s}$
Σ	$\frac{\Sigma}{\Delta}$	$\frac{E_{e'}^2\sin^2\theta_e}{1-y_\Sigma}$	$\frac{Q_\Sigma^2}{y_\Sigma \cdot s}$
$e\Sigma$	$\frac{2E_e\Sigma}{\Delta^2}$	$4E_eE_{e'}\cos^2(\frac{\theta_e}{2})$	$\frac{Q_e^2}{y_{e\Sigma}\cdot s} = x_\Sigma$

Table 4.2: *Determination of the DIS variables for the different reconstruction methods discussed in the text.*

of the *SpaCal* and shows large radiative corrections. At low values of y one obtains

$$\frac{\delta y}{y} \approx \frac{1}{y} \times \frac{\delta E_{e'}}{E_{e'}} \,. \tag{4.4}$$

Since $\delta E_{e'}/E_{e'}$ does not decrease drastically when $E_{e'}$ goes towards E_e, the absolute systematical error of y_e does not significantly decrease with decreasing y_e i. e. the relative uncertainty rises at low y_e. If this method is used, a cut of $y \geq 0.05$ is necessary in order to obtain reasonable accuracy.

The systematic uncertainty due to the error of θ_e is small compared to the contribution from the energy measurement.

The electron method is very sensitive to the radiation of additional photons from the positron, see Section 4.3.3.

The Σ method

This method is based on the three measured quantities Σ, Δ and θ_e as defined above. In that sense it is not independent of the measurement of the positron energy. The relative uncertainty of y_Σ is however always smaller than that of the positron energy. Uncertainties from the measurement of the hadronic energies (Σ) partly cancel between numerator and denominator. One obtains (neglecting again the contribution from the measurement of θ_e)

$$\frac{\delta y}{y} \approx (1-y) \times \left(\frac{\delta E_{e'}}{E_{e'}} \oplus \frac{\delta \Sigma}{\Sigma} \right) \,, \tag{4.5}$$

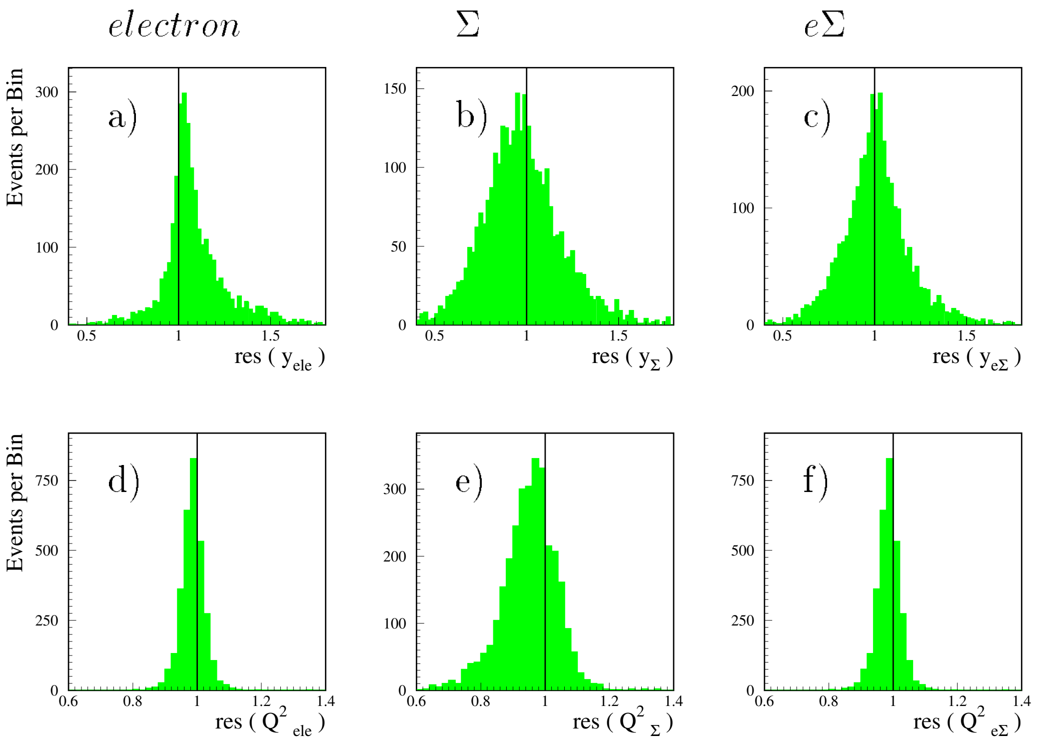

Figure 4.6: *Resolution of the different DIS reconstruction methods as determined from the* MC *simulation. The histograms show the distribution of* $res(val) = val_{rec}/val_{gen}$ *for val=y and val=*Q^2*. The selection cuts are standard, except that the lower cutoff for* y *has been raised to* $y \geq 0.05$*. For all the plots, the events have been selected using the e*Σ *method (continuation see Figure 4.7).*

where $\oplus$ stands for the quadratic sum. This uncertainty does — in contrast to the case of the electron method — not show any divergences. It is mostly dominated by the uncertainties of the hadronic energies.

Both the values of y and Q^2 are defined such that they are still correct in the case of initial state radiation. This advantage is compensated partly since one must rely on quantities with relatively large systematic errors[3].

The accuracy of Q^2 is however clearly poorer than in the case of the

[3]The value of Δ for instance could - in the case of no radiation - be determined much more accurately by using $\Delta = 2E_e$. Taking the measured energies of the final state instead, gives us the ability to calculate the scattering process correctly, even if the positron has lost momentum due to initial state radiation.

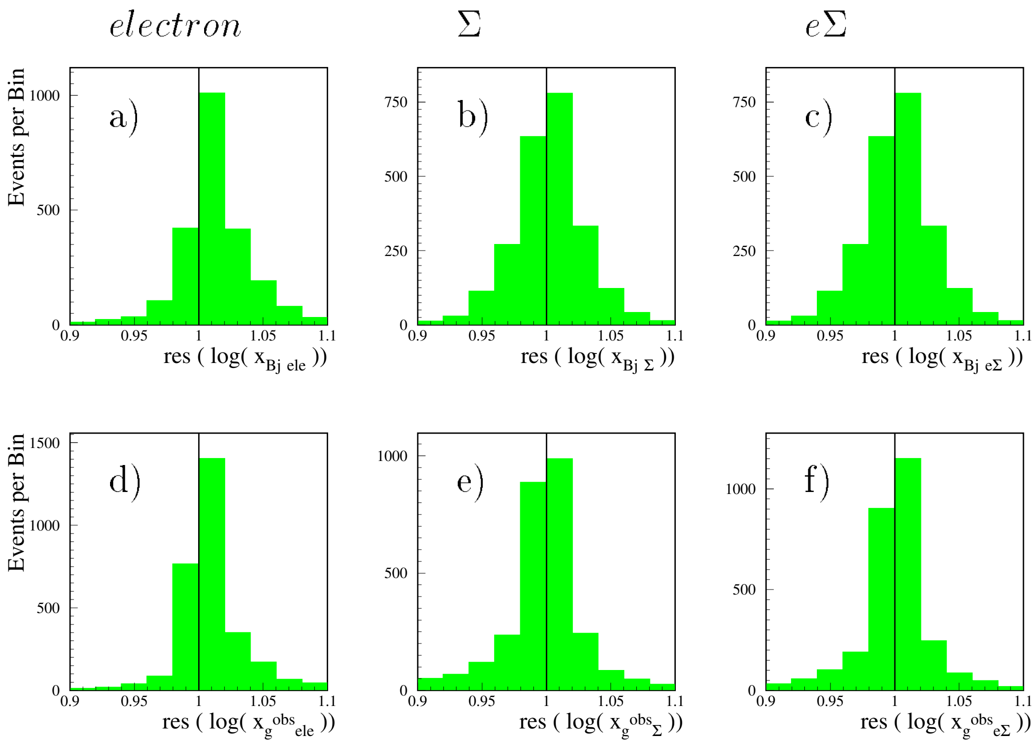

Figure 4.7: *Resolution of the different DIS reconstruction methods as determined from the* MC *simulation. The histograms show the distribution of* $res(val) = val_{rec}/val_{gen}$ *for val=log(*x_{Bj}*) and val=log(*x_g*). The selection cuts are standard, except that the lower cutoff for* y *has been raised to* $y \geq 0.05$*. For all the plots, the events have been selected using the e*Σ *method (see also Figure 4.6).*

electron method, which leads to the definition of the $e\Sigma$ method.

The $e\Sigma$ method

This method collects the best from the two previously defined methods: the x_{Bj} value is taken from the Σ method, Q^2 from the electron method; for $y_{e\Sigma}$ a somewhat more complicated value follows through the relation $Q^2 = xys$. Through the choice of Q^2_{ele}, a slight dependence on initial state radiation enters into the calculation. The systematic errors on $y_{e\Sigma}$ are moderate and do not show any divergences which makes this method very useful for a measurement which — like ours — relies on only one method for a large range in x_{Bj} and Q^2.

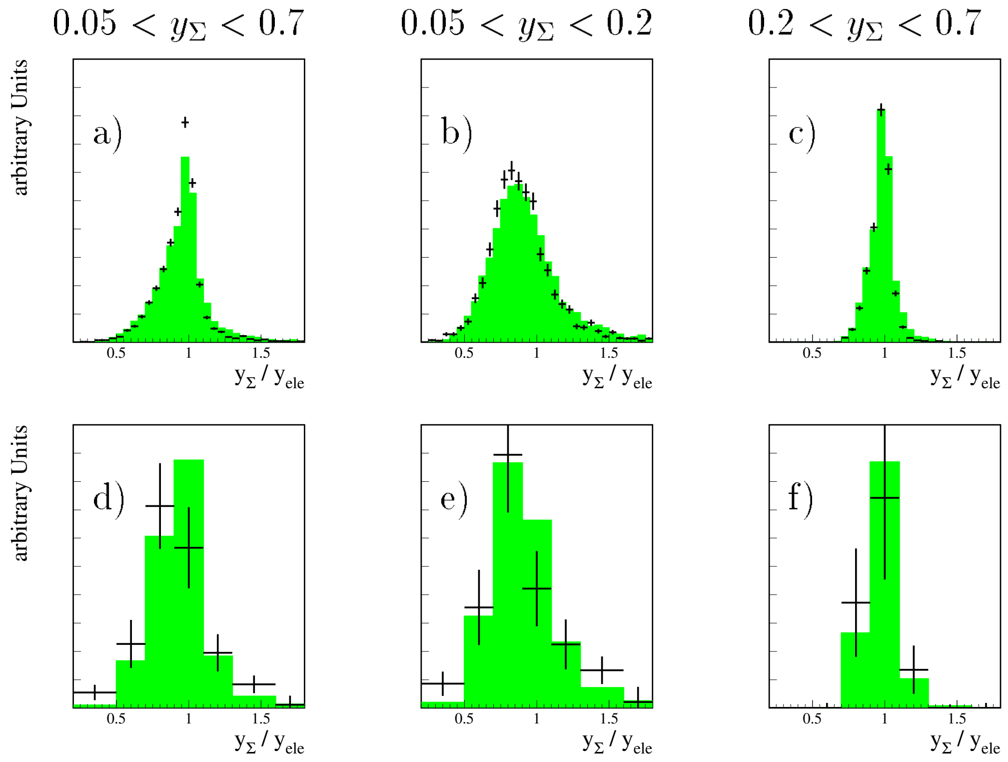

Figure 4.8: *Comparison between the values of y measured with the electron and with the Σ method. See text for further explanations.*

Comparison between electron and Σ method

Given two largely independent methods to reconstruct the kinematical variables of the events, it is of course important to check one against the other. Figure 4.8 shows the comparison between the y values determined using the electron and the Σ method. Histograms a), b) and c) show the number of positron candidates in data (black crosses) and *MC* (gray area). For Figures d) through f), a fit to the $D^\star$ signal in every bin has been used. The statistical error of the latter histograms are large and allow no statement about the calibration of the calorimeters. It is however not a priori clear that agreement must be found if only the number of accepted positrons is looked at: the topologies of the hadronic final states of background events may be quite different from those of $D^\star$ events and hence different sections of the hadronic calorimeters contribute.

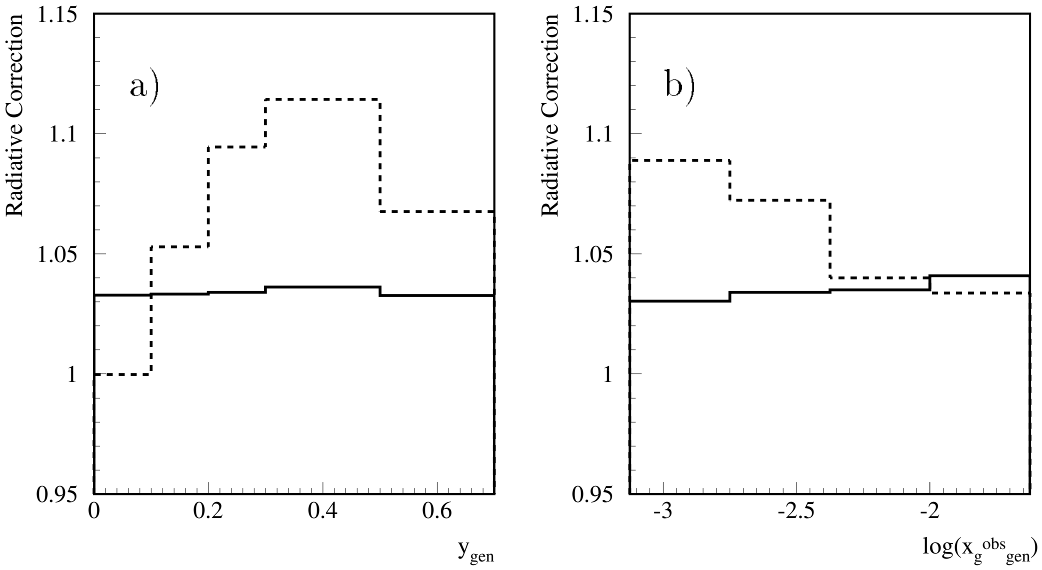

Figure 4.9: *Factors for radiative corrections. Corrected cross sections are obtained by* $\sigma^{corr} = \sigma^{measured}/C_{RaCo}$. *The solid line shows the correction factors for the e*Σ *method, the dashed line is calculated for the electron method. The applied cuts are standard, except for the lower boundary of the y range, which has been raised to 0.05. The advantages of the e*Σ *method are obvious: the corrections for the electron method are much larger and vary strongly.*

A selection cut of $0.05 \leq y_\Sigma \leq 0.7$ has been applied for all histograms. In addition, the data sets have been split at $y_\Sigma = 0.2$. At low values of y_Σ (b), e)) the width of the distribution is dictated by the resolution of the electron method. At higher values of y_Σ (c), f)) the electron method is very accurate and the uncertainty of the energy measurement of the hadronic final state dominates the width of the distribution.

4.3.3 Radiative corrections

In a considerable fraction of the *DIS* events not only the highly virtual photon couples to the positron, but in addition a quasi real photon collinear with the positron appears. Photons emitted by the incoming positron (*Initial State Radiation, ISR*) usually escape detection by the central detector components as they pass through the beam hole in backward direction. The energy of hard collinear photons radiated after the *DIS* scattering process

(*Final State Radiation, FSR*) is mostly contained in the energy cluster attributed to the positron. FSR does therefore not significantly affect the measurement of the DIS process, no matter which method is used to reconstruct the kinematics.

Unlike FSR, *initial state radiation* spoils the measurement: by emitting a hard photon, the positron looses momentum in the order of several GeV, and hence the center of mass energy of the ep system is significantly reduced. The electron method leads in this case to completely wrong measurements of x_{Bj} and Q^2, since it assumes the energy of the incoming positron to be exactly the energy of the beam. The Σ and the $e\Sigma$ methods are safe against that error, since the momentum of the scattering positron is reconstructed explicitly from the value of Δ as measured in the final state.

Correction factors to compensate the effect of ISR have been calculated [50, 51, 52] for the analysis presented. These corrections depend strongly on the allowed final states. The following cuts have been applied in addition to the standard cuts:

- Δ is required to be greater than 35 GeV. This cut forces the energy of the ISR photon to be below $\approx$ 10 GeV. This requirement is fulfilled implicitly by the data.

- The center of mass energy of the γp system, W, is required to be greater than 30 GeV, which is fulfilled approximately in data due to the threshold of the charm quark mass and corresponds to $y > 0.01$.

Both of these cuts have reduced the expected correction factors significantly, since they limit the allowed phase space of the ISR photons. As can be seen in Figure 4.9 , the corrections are below 5% for the $e\Sigma$ method and around $5 - 10\%$ for the electron method. The systematic error induced by this correction has been set to the size of to the correction itself.

4.4 D* reconstruction

The reconstruction of the invariant mass of the $D^\star$ candidates is done in two steps according to the consecutive decays of the charmed mesons through the chain $D^\star \to D^0\pi_s \to (K\pi)\pi_s$. All pairs of good tracks are given the mass hypothesis of being the K and the π from the D^0 decay and the invariant mass of the pair is reconstructed accordingly. If this mass is reasonably close to the mass of the D^0 meson, the list of the so far unused tracks is scanned for possible π_s candidates. The uncertainties of the measurement of the K and π momentum cancel to a good part if we do not calculate the reconstructed mass of the $D^\star$ candidates but rather the difference between the invariant masses of $D^\star$ and D^0

$$\Delta m \equiv m_{D^\star} - m_{D^0} = m(K\pi\pi_s) - m(K\pi)\ . \qquad (4.6)$$

The number of $D^\star$ mesons is determined by a fit of the Δm distribution as we will show in section 4.4.3 .

4.4.1 Selection cuts

Track Selection

Since the reconstruction of the $D^\star$ meson is based on invariant masses calculated from the momenta of reconstructed tracks, we need to start from a selection of well measured particle tracks. Only tracks from the central tracker (*CJC*) are considered, which restricts the analysis already to the central rapidity region[4].

The cuts will be described briefly in the following, after sketching the track reconstruction procedure used in H1. The cut values actually used in the analysis can be found in table 4.3 .

The track reconstruction [33] starts from the information of the *CJC*, when circle segments are fitted to the $r\phi$–projection of the measured hits [53]. The tracks are parametrized as helix. The parametrization is based on the point of closest approach of the helix to the beam axis with z–coordinate z_0 and the distance DCA from the z–axis. ϕ and θ define the direction of the

[4]The visible range of the analysis is defined by the rapidity of the $D^\star$ rather than by that of the daughter particles (see Section 4.1). Correction factors for losses due to secondary particles leaving the acceptance region even if the $D^\star$ is within bounds are calculated from *MC*.

track at the point of closest approach and therefore implicitly its xy–position. The momentum of the track is parametrized through the curvature of the helix, $\kappa \propto 1/p_{\perp}$.

All well reconstructed tracks of an event are used to determine a common vertex in the $r\phi$–plane as well as in z. Only then the information of the z–chambers enters, when their hits are linked to the existing tracks and improve the accuracy of the θ measurements of the track candidates[5]. Some tracks are now found to be inconsistent with the assumption that they originate from the common vertex. They are excluded from the sample of *vertex fitted tracks* and enter the search for secondary vertices. Even though all the hadronic particles used in this analysis originate from secondary vertices, they are all attributed to *vertex fitted tracks* since the typical decay lengths of the considered mesons are well below the vertex resolution of the tracking system which is in the order of 200 μm in $r\phi$ [6].

For all tracks a list of their properties is provided by the reconstruction program. It contains not only the geometrical description of the reconstructed helix of the particle trajectory, but also all the quality criteria. The greater the number of used *CJC* hits ($ncjc$) the better the measurement of the track and the smaller the probability that some short track segments are linked together randomly. To reject badly fitting track hypotheses a cut was applied to the χ^2 of every candidate. Every track had then to fulfill cuts on the total length of its measured segment (l_{track}) and its starting radius (r_{start}). The latter two cuts were adjusted such that the track needs to be a good combination of one track segment in the inner and another one in the outer chamber of the *CJC*. Tracks that leave the *CJC* at too small radii on either end are rejected by a cut on the polar angle of the track (θ_{track}). A cut on the DCA is very useful in order to reject tracks from proton interactions with the beam pipe, random fits and cosmics. In addition, every track is required to be linked to a vertex within the nominal interaction region in z.

In this analysis, these cuts on the track quality have already been applied on an early step of the event selection and are therefore implicitly included in the requirement that the tracks be found at all. In the very similar analysis presented in Reference [14], it has been shown that the chosen cuts do not

[5]For this analysis the link to the z–chambers was not required explicitly, in order not to loose too much luminosity due to HV trips. If the chambers were operational their information was of course used.

[6]This statement only holds for data taken before 1997 when the silicon vertex detector was commissioned.

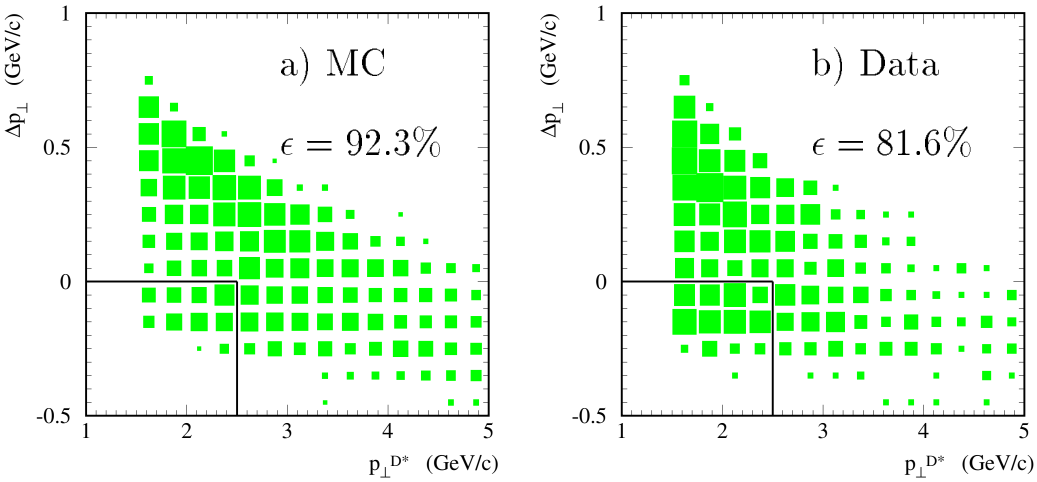

Figure 4.10: *Motivation for the $\Delta p_\perp$ cut. The* MC *simulation (a) shows that the number of events lost from a sample of generated good $D^\star$ events is small whereas a relatively large fraction of the $D^\star$ candidates in data (b) – presumably combinatorial background – is rejected.*

reject a sensible number of track candidates.

A few events get lost due to the cut on the z vertex. The vertex distributions in data and *MC* however agree very well and this effect is therefore contained in the calculated efficiencies.

$D^\star$ Candidate Selection

The cuts on the reconstructed $D^\star$ candidate have already been explained in Section 4.1. They restrict the range in pseudorapidity and transverse momentum.

A lower cutoff in the $p_\perp$ of all tracks is necessary since the H1 tracking system is not designed for tracks with a $p_\perp \leq 120$ MeV/c : Pions with such low momenta suffer from significant scattering on the dead material between interaction point and *CJC* and their momenta cannot be reconstructed. In addition, the track reconstruction is only reliable if $p_\perp^{\pi s}$ is high enough that the track reaches the outer *CJC*. The $p_\perp$ cut on the π_s track has been set to the lowest possible value. Since the π_s carries around 10% of the $p_\perp$ of the $D^\star$ (Fig 4.2 a)) this cut is kinematically bound to the cut on the transverse momentum of the $D^\star$.

The cuts on $z_{D^\star}$ and m_{D^0} were needed in order to improve the signal to

Block	Variable	cut value	Efficiency rel. to previous %	Efficiency total %
1	full sample after cuts on visible range			100
2	positron selection		93.5	93.5
3	polar angle θ	$20° \leq \theta \leq 160°$	87.3	81.6
	$p_\perp^{\pi s}$	≥ 120 MeV/c	84.3	68.8
	$p_\perp^{\pi}$,$p_\perp^{K}$	≥ 250 MeV/c	94.1	64.7
	$\Delta p_\perp$	≥ 0 MeV/c if $(p_\perp^{D^\star} < 2.5$ GeV/c$)$	92.3	59.8
4	K, π, π_s tracks reconstructed			
	radius at track start	≤ 35.0 cm		
	length of track	≥ 10.0 cm		
	z–vertex	$\|zVtx\| \leq 40.0$ cm		
	DCA	≤ 2.0 cm	80.0	47.7
	Reconstructed D^0 mass	1.7845 GeV/c^2 $\leq m_{D^0}$ $m_{D^0} \leq 1.9445$ GeV/c^2	97.6	46.5
5	$z_{D^\star}$	≥ 0.2	85.7	39.9
6	all cuts on reconstr. tracks		99.8	39.8
	fit to Δm		99.9	39.7

Table 4.3: *List of cuts used to select tracks for the $D^\star$ reconstruction. For a detailed definition of the different variables see in the text (Section 4.4.1). The numbers of the blocks correspond to the different histograms in Figure 4.11 .*

background ratio of the final sample. Higher thresholds on $p_\perp^\pi$ and $p_\perp^K$ have been applied for the same reason. In addition, the quantity $\Delta p_\perp$ has been defined as

$$\Delta p_\perp = p_\perp^{D^\star} - p_\perp^K - p_\perp^\pi \ .$$

At low values of $p_\perp^{D^\star}$, $\Delta p_\perp$ is required to be positive. The motivation for this cut is apparent from the distributions shown in Figure 4.10 .

4.4.2 Reconstruction efficiencies

The reconstruction efficiencies have been determined from the *MC* simulation based on the generator *AROMA*. The relative event losses at the different steps of the selection are given in Table 4.3 . The corresponding distributions for the different variables are shown in Figure 4.11 .

The cuts defining the visible cross section have been applied to the generated variables and define the ensemble of events we would like to reconstruct. A first reduction of the event sample is due to the cuts from the positron identification (Block 2 in Table 4.3 , black histogram in Figure 4.11 ; see also Section 4.3.1). The selection cuts on θ and the transverse momentum of the daughter particles have subsequently been applied (Block 3, upper light grey histogram). The ratio of events surviving these cuts compared to the previous sample defines the acceptance. The efficiency for finding three tracks has been estimated by requiring that the K, π and π_s candidates were found in the neighborhood of the generated tracks. The 'neighborhood' has been defined by a box of $\pm$ 0.05 (0.15) rad in θ and ϕ around the generated K, π (π_s). The cuts on the track qualities (Table 4.3) are already included in this step. The efficiency curves after applying the cut on the reconstructed D^0 mass (see Section 4.4.3) in addition are shown as the dark grey histogram (Block 4). The cut on $z_{D^\star}$ removed another 15% of the events, improved however the signal to background ratio in the data significantly (Block 5, light grey histogram). The number of accepted events was essentially unchanged, when all the cuts from Block 3 were applied on the reconstructed instead of the generated tracks. Lastly we checked that the fit to the reconstructed Δm distributions of the *MC* — as described in Section 4.4.3 — yielded a number of events equal to the number of generated $D^\star$ mesons. The final efficiencies (shown as points with statistical errors in Figure 4.11) are also influenced by the kinematical reconstruction because we have defined them as the ratio of the number of accepted events in a given bin of a *reconstructed* kinematical variable to the number of events generated in the same bin of the *generated* variable [4]. Migration effects are however found to be small as the comparison to the efficiency curves after the last cut shows (Figure 4.11). Since the efficiencies depend strongly on $p_\perp$ and η it is vital to confirm agreement between data and simulation in as many kinematical variables as possible. We do this comparison at the cross section level after radiative corrections have been applied to the data, background has been removed and the efficiencies have been accounted for. The quantity used for the comparison shown in Figure 4.12 is

$$\frac{N^{MC}_{gen,vis}}{\mathcal{L}_{MC}} \cdot C_{norm.} \Longleftrightarrow \frac{N^{MC}_{gen,vis}}{N^{MC}_{rec,vis}} \cdot \frac{N^{data}_{rec,vis}}{\mathcal{L}_{data}} \cdot C_{Corrections} \ . \tag{4.7}$$

In order to be more sensitive to differences of the shapes, the *MC* curves have been normalized through $C_{norm.}$ to reproduce the total cross section of the data. No significant deviations are found.

Reconstruction of the slow pion

The evaluation of the reconstruction efficiency as a function of the momentum of the slow pion π_s requires special attention. At the mimimum value of the transverse momentum accepted in our analysis, $p_\perp$ =120 MeV/c, the pion already loses a significant amount of energy between the interaction point and the CJC. In principle the reliability of the treatment of the slow pion can be tested by shifting the momentum cutoff upward, e. g. to 160 MeV/c, and then comparing the data from the region $120 < p_\perp < 160$ MeV/c to the data above 160 MeV/c. However the transverse momentum of the slow pion is strongly correlated with the transverse momentum of the $D^\star$, and hence such a comparison will reflect to a large extent how well the MC describes the $p_\perp^{D^\star}$ distribution found in the data and not only the treatment of the slow pion. As apparent from Figure 4.12 the MC simulation predicts less events at low $p_\perp^{D^\star}$ than found in the data. Therefore we restricted — at the cost of statistical accuracy — this check to the window $1.5 < p_\perp^{D^\star} < 2.5$ GeV/c. We found 44 ± 10 (29 ± 8) $D^\star$ candidates for the low (high) region of the slow pion transverse momentum, corresponding to 262 ± 59 (178 ± 51) after

[4]For the cross sections, the small statistical errors of the efficiencies have been added in quadrature to the statistical errors of the data points.

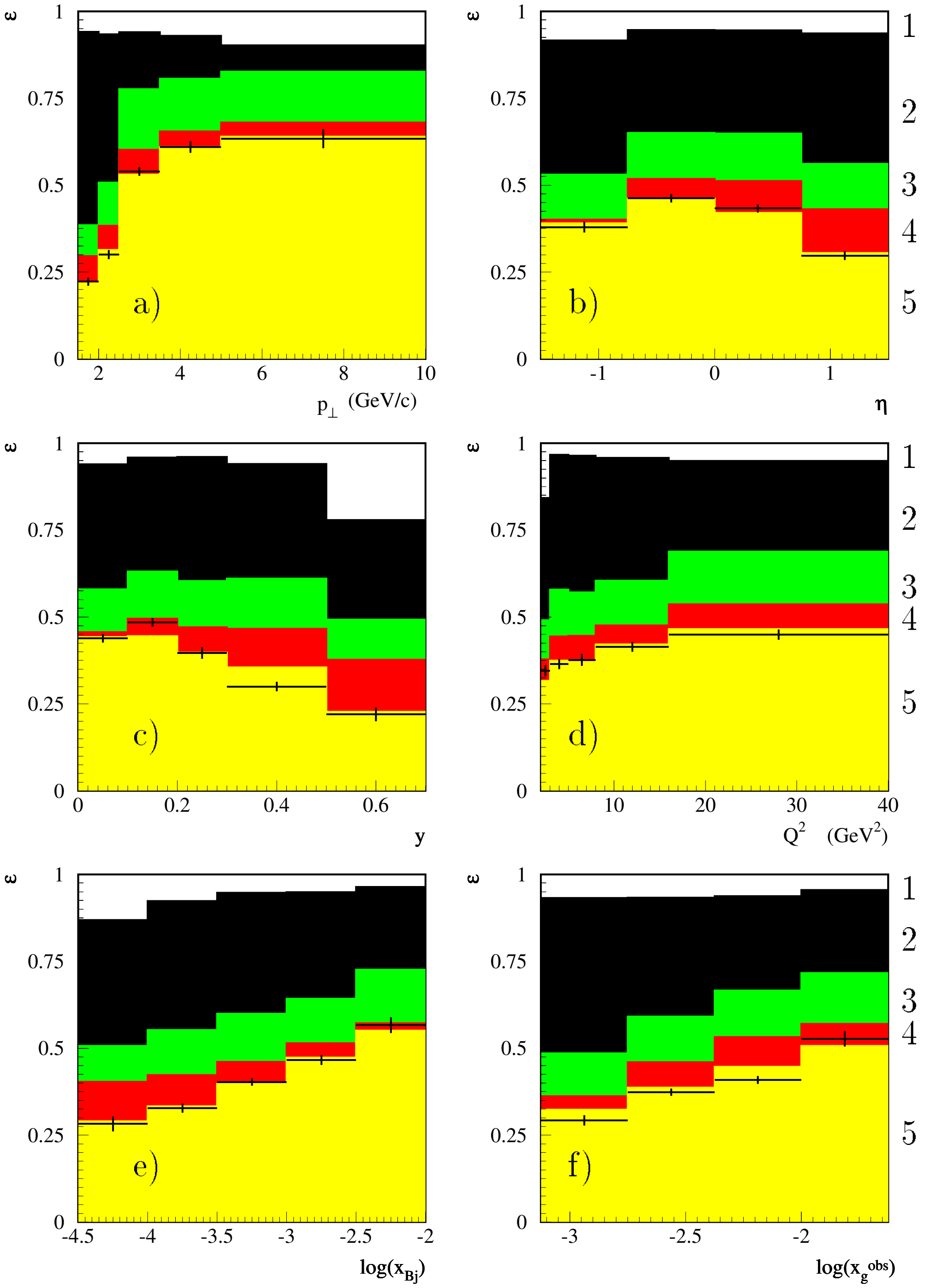

Figure 4.11: *Reconstruction efficiencies (ϵ) in function of different kinematical variables. The numbers on the right correspond to the sequence of cuts listed in Table 4.3 (see text for further explanations). as determined from MC, see text for further explanations.*

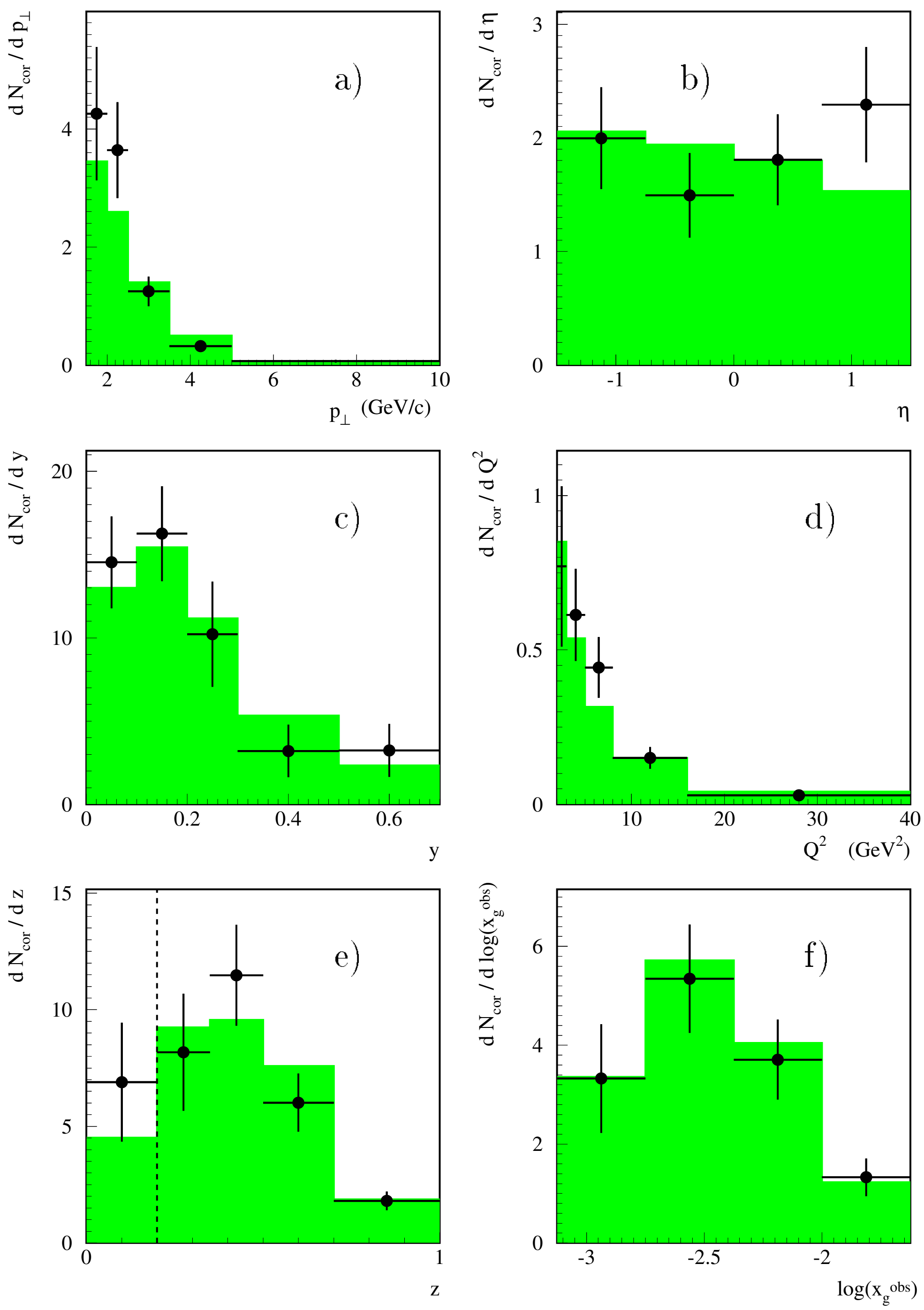

Figure 4.12: *Comparison between data and MC, see text for further explanations. For the number of events as a function of $z_{D^\star}$ the cut on that variable has been opened. The dashed line indicates where it is usually applied.*

acceptance corrections. These are equal within their albeit large statistical errors.

4.4.3 Mass reconstruction

Reconstructed D^0 mass

We apply a cut on the reconstructed invariant mass of the D^0 in order to suppress background. Figure 4.13 shows that the width of a Gaussian fitted to the D^0 peak in the data is 27.9 ± 5.9 MeV/c^2 while in the *MC* description a width of 23.2 ± 4.6 MeV/c^2 is found. All D^0 candidates with a reconstructed mass in the window 1864.5 ± 80 MeV/c^2 have been accepted, i.e. the cut has been set about 3σ away from the nominal D^0 mass.

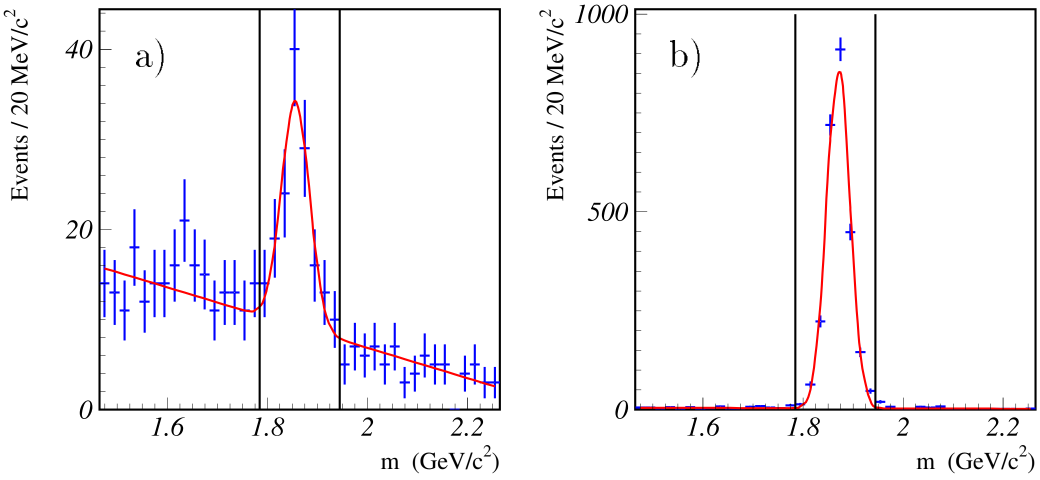

Figure 4.13: *D^0 mass peak as found in data and Monte Carlo, fitted by a Gaussian plus a linear description of the background. The vertical lines indicate the cut applied in the $D^\star$ analysis. In order to obtain a clear D^0 peak with low background, a tight cut on Δm of* 145.5 ± 1.0 MeV/c^2 *has been applied for the plots shown. The normalization of the D^0 peak is therefore not investigated as event losses depend on the width of the Δm peak. The side peak centered around* 1.65 GeV/c^2 *in the data is due to the decay chain* $D^\star \to D^0\pi_s \to K^-\pi^+\pi^0$.

parameter	symbol	fitted value			units
		DIS		$DIS + \gamma p$	
		5 par.	3 par.	5 par.	
norm. Gaussian	A	164.7 $\pm$ 23.1	151.8 $\pm$ 17.1	235.3 $\pm$ 28.33	events
center Gaussian	Δ_0	145.37 $\pm$ 0.16		145.5 $\pm$ 0.12	MeV/c^2
width of Gaussian	σ	1.205 $\pm$ 0.205		1.043 $\pm$ 0.122	MeV/c^2
norm. background	B	927.2 $\pm$ 36.1	940.6 $\pm$ 33.0	1894. $\pm$ 50.0	events
exponent background	α	0.424 $\pm$ 0.068	0.392 $\pm$ 0.054	0.286 $\pm$ 0.039	

Table 4.4: *Results of the fits to the total data samples. The last column also uses events from photoproduction – with* $p_\perp^{D^\star} > 2.5$ GeV/c *– in order to have the maximal possible data set and therefore a small statistical error on the peak width. The uncertainty of the peak width was a source of a systematic error for the fits with only 3 free parameters.*

Reconstructed $D^\star - D^0$ mass difference

The number of reconstructed $D^\star$ events has been obtained from a fit to the Δm distribution. The world average of the measured mass difference is 145.42 ± 0.05 MeV/c^2 [24]. The π_s is therefore emitted with a momentum of 40.8 MeV/c and a kinetic energy of 5.85 MeV in the $D^\star$ rest frame. In Figure 4.14 the Δm distribution for the entire 95 data set is shown. It has been fitted by a Gaussian plus a background function:

$$\begin{aligned} f(\Delta_m) &= \frac{A}{\sqrt{2\pi}\sigma} \cdot exp\left(-\frac{(\Delta_m - \Delta_0)^2}{2\sigma^2}\right) \\ &\quad + B \cdot \frac{(\Delta_{max} - m_\pi)^{(\alpha+1)}}{\alpha + 1} \cdot (\Delta_m - m_\pi)^\alpha \ . \end{aligned} \tag{4.8}$$

The meanings as well as the obtained values of the five free parameters (A, B, σ, Δ_0 *and* α) are listed in Table 4.4 . The center and the width of the

var.	boundaries of bins											units
	Fitted number of $D^\star$ per bin											
$p_\perp$	1.5		2.0		2.5		3.5		5.0		10.0	GeV/c
N		31.2		39.1		48.6		19.8		15.2		
$\pm stat$		8.5		8.5		9.4		5.9		5.1		
A / B		9.1		20.5		17.7		24.0		32.8		%
η	-1.5		-0.75		0.0		0.75		1.5			
N		39.8		38.3		39.0		37.5				
$\pm stat$		8.6		8.8		8.8		8.2				
A / B		20.1		12.5		14.8		20.2				%
$log(x_g^{obs})$	-3.125		-2.75		-2.375		-2.0		-1.625			
N		22.8		54.0		35.3		23.4				
$\pm stat$		7.4		10.4		8.5		5.9				
A / B		10.4		14.5		14.1		42.5				%

Table 4.5: *Results of the $D^\star$ fits in bins of $p_\perp$, η and x_g^{obs}. No bin size correction has been applied yet. The last row of every block shows the signal (A) to background (B) ratio where B is the fitted number of events in the range $\Delta m < 0.17$ GeV/c^2.*

peak have also been determined using a data set with the maximum available statistics, including events from photoproduction. In the following these two parameters were fixed to the values obtained from that maximal sample. This made the fits to smaller subsamples of the data more stable. The center of the peak has been fitted very precisely and no significant change in the results of the fits with fixed center have been found if the center was moved within the errors given by the global fit. For the width, we found differences in the order of 7% when the fixed value was changed by $\pm 1\sigma$. This effect was included in the systematic error of the measurement. The exponent and the normalization of the background relative to the peak could not be fixed as one might have liked to do. Both parameters change significantly depending on the phase space of the selected subsamples.

The results of the fits in bins of $p_\perp$, η and $log(x_g^{obs})$ are shown in Table 4.5 .

All fits have been done using the *log likelihood* method as implemented in the *MINUIT* [55] program.

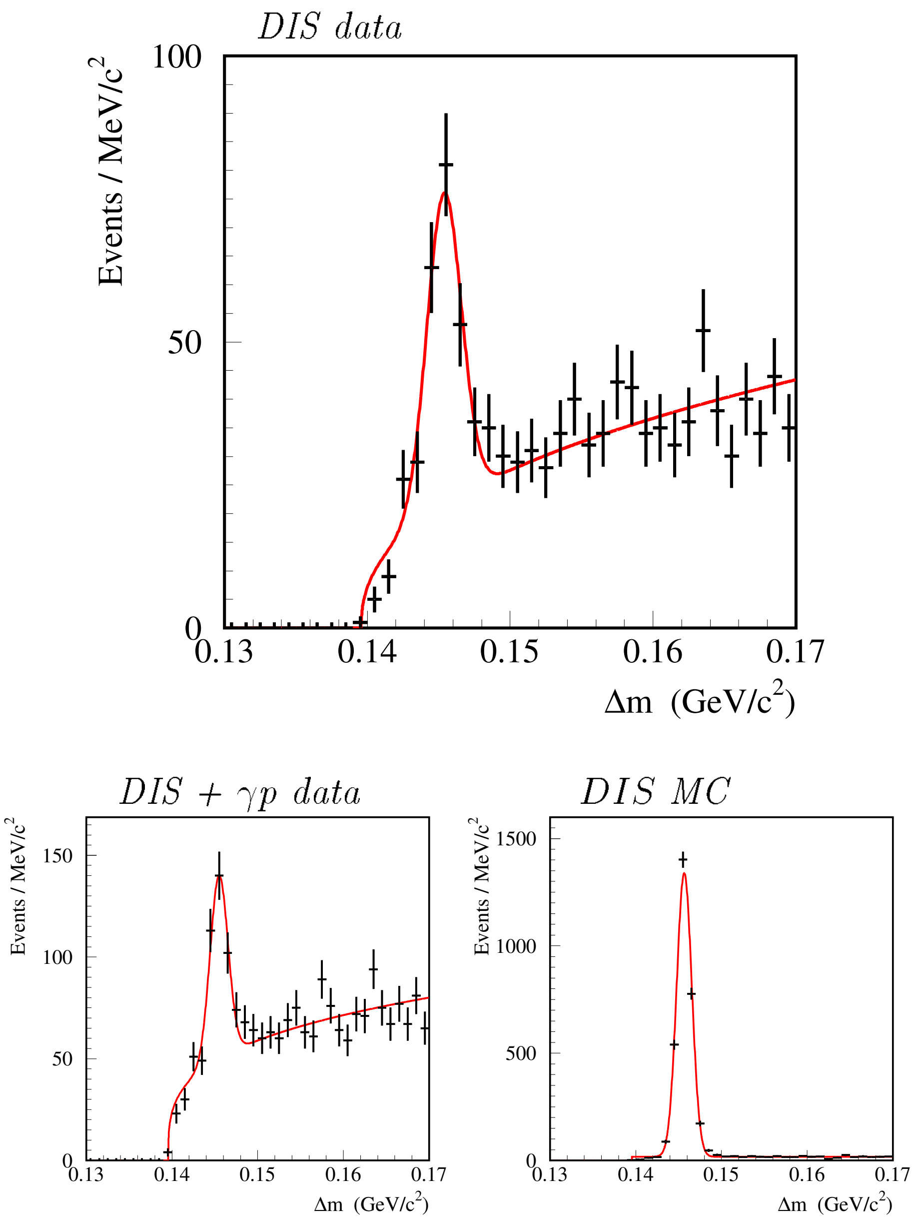

Figure 4.14: *a) Δm signal used for the calculation of the total cross section, the shown curve is the five parameter fit corresponding to column 1 in Table 4.4. b) Sample including high $p_\perp$ photoproduction as well, used to determine the width of the peak (col. 3). c) Signal from the DIS MC used here.*

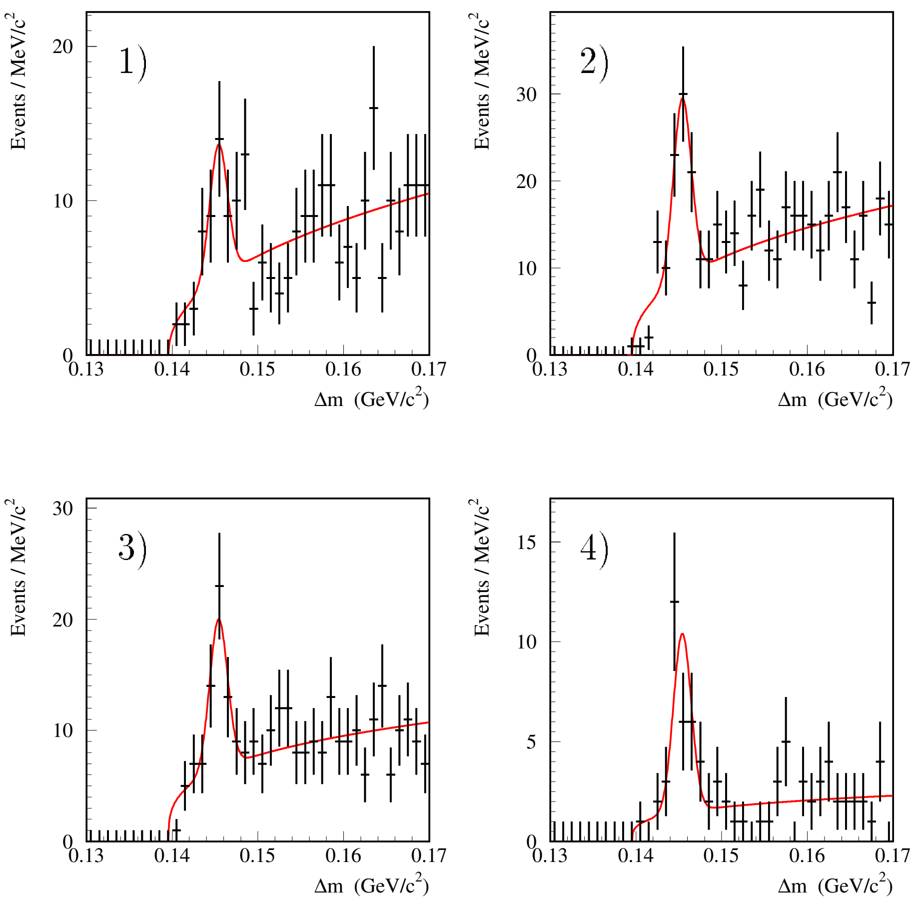

Figure 4.15: Δm *peaks for the four bins of* $log(x_g)$ *used for the measurement of the gluon density.*

4.4.4 Reflections

Reconstructed invariant masses of pairs of charged particles from the decays $D^0 \rightarrow K^-\pi^+\pi^0$, $D^0 \rightarrow \pi^+\pi^-$ and $D^0 \rightarrow K^-K^+$ may occasionally lie in the selected D^0 mass window and enter into the event sample. In the Δm plot these events cluster exactly in the peak region. We could handle the contribution to the Δm peak due to these channels as an increase of the branching ratio of the allowed process. We chose the opposite point of view and considered these events as a pollution of the data set and corrected the measured event numbers accordingly. A fit to *MC* distributions revealed that from a total of 73 $D^\star$ events where the $D^\star$ and the D^0 decay have not been restricted to a particular channel, 7.8 ± 5 were due to decays of the $D^\star$ through other chains than the one selected for this analysis. More detailed studies [56, 57] determined smaller contributions. As an average of the different values, the contribution of the reflections to the signal was determined to be $7 \pm 4\%$.

4.4.5 D* from beauty meson decays

Apart from direct production of c quarks, charmed mesons may originate from decays of particles containing b quarks (*beauty)*. The kinematical distributions of the $D^\star$ mesons from b quark decays differ from those obtained from direct $\gamma g \rightarrow c\bar{c}$ fusion (see Figure 4.16). The reconstruction efficiencies for $D^\star$ from b quarks may therefore differ from those calculated for direct charm production. The complete detector simulation has been run for a set of generated $D^\star$ events from b quark production. In the end we found 77.3 ± 13.5 events in 110 pb^{-1} of simulated luminosity. These events were — scaled down to the actual luminosity of the measurement — subtracted from the data before the efficiency corrections as described in Section 4.4.2 have been applied.

First measurements of b quark production in γp interactions indicated that *AROMA* underestimates the b quark cross section significantly [58, 59]. The b quark background correction of our measurement had therefore been assigned a very large systematic error in order to be consistent with zero b quark contribution as well as with four times the b quark cross section predicted by *AROMA*.

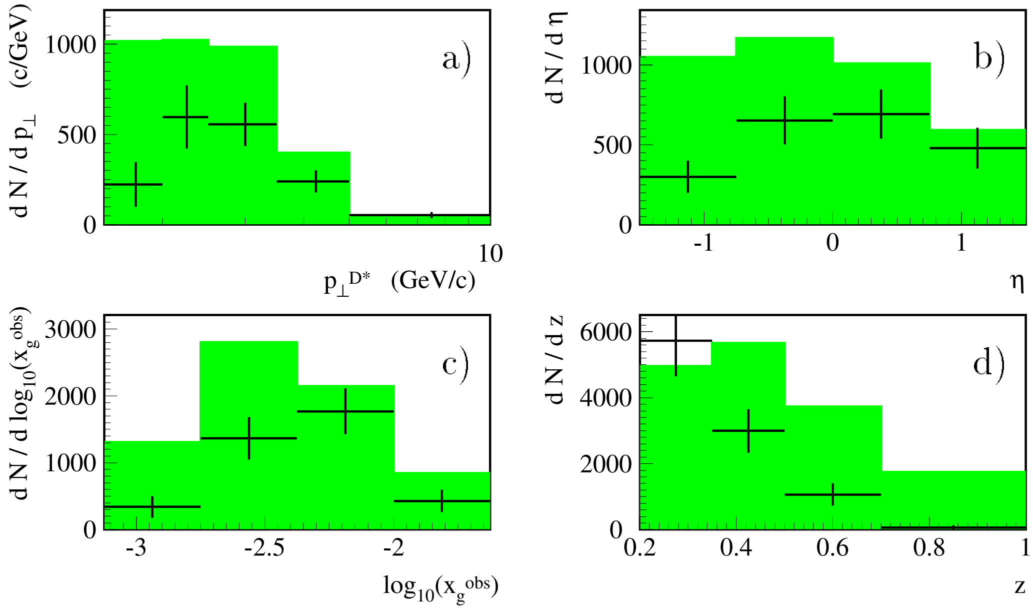

Figure 4.16: *Distributions of $D^\star$ mesons from b quark decays (black crosses) compared to $D^\star$ from direct boson–gluon fusion of charm (histogram). Both distributions are obtained from the MC generator AROMA, the contribution from beauty has been scaled by a factor of 50 relative to the charm prediction.*

4.5 Systematic errors

Some of the sources of systematic errors to the measurement have already been mentioned in the previous sections. All contributions are listed and explained here. The error sources have been divided into uncertainties which arise from corrections that had to be applied to the data and errors that are due to uncertainties of the detector calibrations or other constants.

Errors due to corrections

- Trigger efficiencies have been determined from data, for the track triggers the determined efficiencies were compared to the *MC* simulation and agreement was found. Run selections have been applied in order to reject runs with known problems of $r\phi$–, *zVtx*– and *IET*–triggers. A large uncertainty has however been attached to the trigger efficiency since the *SpaCal* was still being tuned while the first data analyzed here have been recorded (see Section 4.2.2).

Effect	Correction	Syst. Error on cross section	
		$\Uparrow$	$\Downarrow$
Trigger - efficiency	1.4 %	5.0 %	1.4 %
Photoproduction background	0 %	0.0 %	1.0 %
b induced background	1-2 %	corr.	$3 *$ corr.
Reflections	7 %	4 %	
Radiative corrections	3.4 % (6.5 %)	correction	

Table 4.6: *Corrections applied to the data. The given numbers are calculated for the $e\Sigma$ method, the values obtained when using the electron method are given in brackets if they are different.*

- Photoproduction background: due to their much higher cross section, γp interactions at $Q^2 \approx 0$ GeV^2 usually cause a significant background in *DIS* samples, with particles from the hadronic final state faking positrons in *SpaCal*. In this analysis we found no indication for γp background, neither in data nor in *MC*. The photoproduction background is significantly suppressed by the required final state, the cuts on the positron candidate and by the cut on $z_{D^\star}$. No correction had therefore to be applied to the data, the systematic error assigned is larger than the statistical error derived from the *MC* statistics (see Section 4.3.1).

- $D^\star$ from b quark production: we subtract the prediction by the *AROMA* generator from the data, setting the error such that it covers the range from no contribution at all up to four times the prediction. For the differential cross sections this is done binwise (see Section 4.4.5).

- Reflections in the Δm peak have been estimated using a *MC* data set containing all possible decay modes of the $D^\star$. The applied correction is an average of two different methods to calculate the contributions of other decay modes, with an error bar large enough to be consistent with both single results (see Section 4.4.4).

- Radiative corrections had to be applied in order to correct for event losses due to collinear γ radiation by the positron immediately before the DIS scattering process (ISR). The correction factors are different for the different kinematics reconstruction methods used and depend strongly on the selected final state. The properties of the $D^\star$ events could only partly be translated into cuts which could be fed into the program used to calculate the corrections. We therefore decided to set the error of this correction equal to the correction itself. Variations of the W cut and the proton structure function resulted in changes that were much smaller (see Section 4.3.3).

Errors due to uncertainties of calibrations and constants

- The luminosity measurement introduces an uncertainty on the normalization of all cross sections [60].

- Energy scales of the used calorimeters (*SpaCal* electromagnetic and hadronic, *LAr*): the uncertainties of the scales are given by the calibration procedures. In the case of the electromagnetic section of *SpaCal* it is e. g. given by the uncertainty of the re–calibration described in appendix C. Since no further cross check with another independent method, e. g. the double angle method has been done, the uncertainty of the energy scale has been taken to be as big as that final correction itself. The cell by cell calibration was not yet finally optimized at the beginning of the data taking. This is taken into account by smearing the energies in the MC by $\pm 1\%$. For the hadronic energy scales uncertainties have been assumed to be the same as in Reference [10]. The influence of the uncertainties of the energy scales on the measurement have been determined by repeating the data analysis, shifting the reconstructed energies by $\pm 1\sigma$.

- The determination of Q^2 depends on the accurate measurement of the positron scattering angle. Again, the entire analysis was carried out shifting θ_e by the uncertainty given by the BDC resolution. An additional uncertainty in the BDC hit finding had to be included due to discrepancies between the efficiencies observed in data and MC [10]. It seems however probable that these discrepancies are not due to a bad MC description but rather due to a pollution of the data sample

Effect	Uncertainty	Syst. Error on total cross section $\Uparrow$	$\Downarrow$
Scale electromagnetic	2 % at 27GeV 3 % at 7GeV	4 % (9 %)	
Scale had.	7 %	<1 % (0 %)	
Scale LAr	4 %	1 % (0 %)	
Positron angle	0.5 mrad	<1 %	
BDC hit finding	2 %	$\pm 2\%$	
Luminosity measurement		$\pm 1.5\%$	
Track - reconstruction		9 %	3 %
$D^{\star}$-Fit	$\pm 1\sigma$ of fit with free peak width	$\pm 7\%$	
Branching ratio		4 %	
Total (including errors from corrections)		15 % (16.7 %)	12.2 % (14.3 %)

Table 4.7: *Systematic errors of the data. The numbers are given for the* $e\Sigma$ *method, the values obtained when using the electron method instead are given in brackets if they are different.*

used to determine the *BDC* hit efficiency with photons from γp events [61].

- The *MC* description of the track reconstruction has been checked on 1994 data using K_s^0 decays [62]. The resulting systematic error on the $D^{\star}$ reconstruction efficiency reflects the accuracy reached with that method. Comparisons of the distributions of track–related variables in data and *MC* have shown that the description by the simulation in 95 is of about the same quality as in 94.

- The width of the Δm peak has been determined from a sample with maximal statistics, including events from photoproduction. The statistical uncertainty of that fit enters as a systematic uncertainty in the analysis where the width of the peak is kept fixed. The fits have therefore been repeated varying the peak width by $\pm 1\sigma$ (see Section 4.4.3).

- The error on the world average of the branching ratio for $D^\star \to D^0\pi_s \to (K\pi)\pi_s$ is taken from Reference [24].

4.6 Results

Based on the information obtained as described in the previous sections, we can finally determine the observed cross sections through:

$$\sigma^{vis}_{D^\star} = \left(\frac{N_{meas}}{\mathcal{L} \cdot BR_{D^\star - K\pi\pi}} \cdot \frac{C_{Reflect}}{C_{RaCo} \cdot \epsilon_{Trig}} - \frac{N^{from\ b}_{MC\ rec}}{\mathcal{L}^b_{MC}} \right) \cdot \frac{N_{MC\ gen}}{N_{MC\ rec}} \ . \qquad (4.9)$$

N_{meas} stands for the number of reconstructed $D^\star$ mesons, the total number of generated $D^\star$ mesons is obtained by dividing by the branching ratio. $\mathcal{L}$ is the luminosity of the data set. The second ratio in the equation is close to 1 and contains the trigger efficiency ϵ_{Trig}, the radiative corrections C_{RaCo} and the correction term due to the reflections $C_{Reflect}$. $N^{from\ b}_{MC\ rec}$ gives the contribution due to b quark decays predicted by the MC and is divided by the according luminosity. The last term is the inverse of the reconstruction efficiency for $D^\star$ from BGF of charm. The systematical and statistical errors are calculated accordingly.

With this we find the total cross section in the defined visible range to be

$$\sigma^{visible}_{D^\star} = 5.48 \ \pm 0.63(stat) \ ^{+0.82}_{-0.66}(syst) \ \text{nb}$$

This result is in excellent agreement with $\sigma = 5.77^{+1.15}_{-1.01}$ nb predicted by the program $HVQDIS$ using the GRV parametrization (the given errors are from varying m_c) and with σ = 6.05 nb using the $CTEQ4F3$ parametrization. The generator $AROMA$ predicts σ = 6.39 nb with m_c =1.5 GeV/c^2 and the *GRV LO* parton densities.

Differential cross sections are shown in Figure 4.17 with the main result $d\sigma/dlog(x_g^{obs})$ being enlarged in Figure 4.18 . The numerical values are given in Table 4.8 , together with the definition of the bins.

var.	boundaries of bins											units
	measured cross sections											units
$p_\perp$	1.5		2.0		2.5		3.5		5.0		10.0	GeV/c
$\frac{d\sigma}{dp_\perp}$		4.07		3.76		1.29		0.307		0.067		
$\pm stat$		1.14		0.84		0.26		0.094		0.023		$\frac{\text{nb}}{\text{GeV/c}}$
$\pm syst$		0.62		0.59		0.183		0.052		0.012		
η	-1.5		-0.75		0.0		0.75		1.5			
$\frac{d\sigma}{d\eta}$		2.02		1.54		1.71		2.42				
$\pm stat$		0.45		0.37		0.40		0.54				nb
$\pm syst$		0.34		0.22		0.26		0.37				
$log(x_g^{obs})$	-3.125		-2.75		-2.375		-2.0		-1.625			
$\frac{d\sigma}{dlog(x_g^{obs})}$		3.05		5.54		3.25		1.70				
$\pm stat$		1.00		1.09		0.81		0.44				nb
$\pm syst$		0.51		0.82		0.56		0.25				

Table 4.8: *Measured cross sections. The numbers in the first row per variable show the definitions of the bins. The following rows give the measured cross sections, their statistical and systematical error. For simplicity the asymmetric systematic errors have been averaged.*

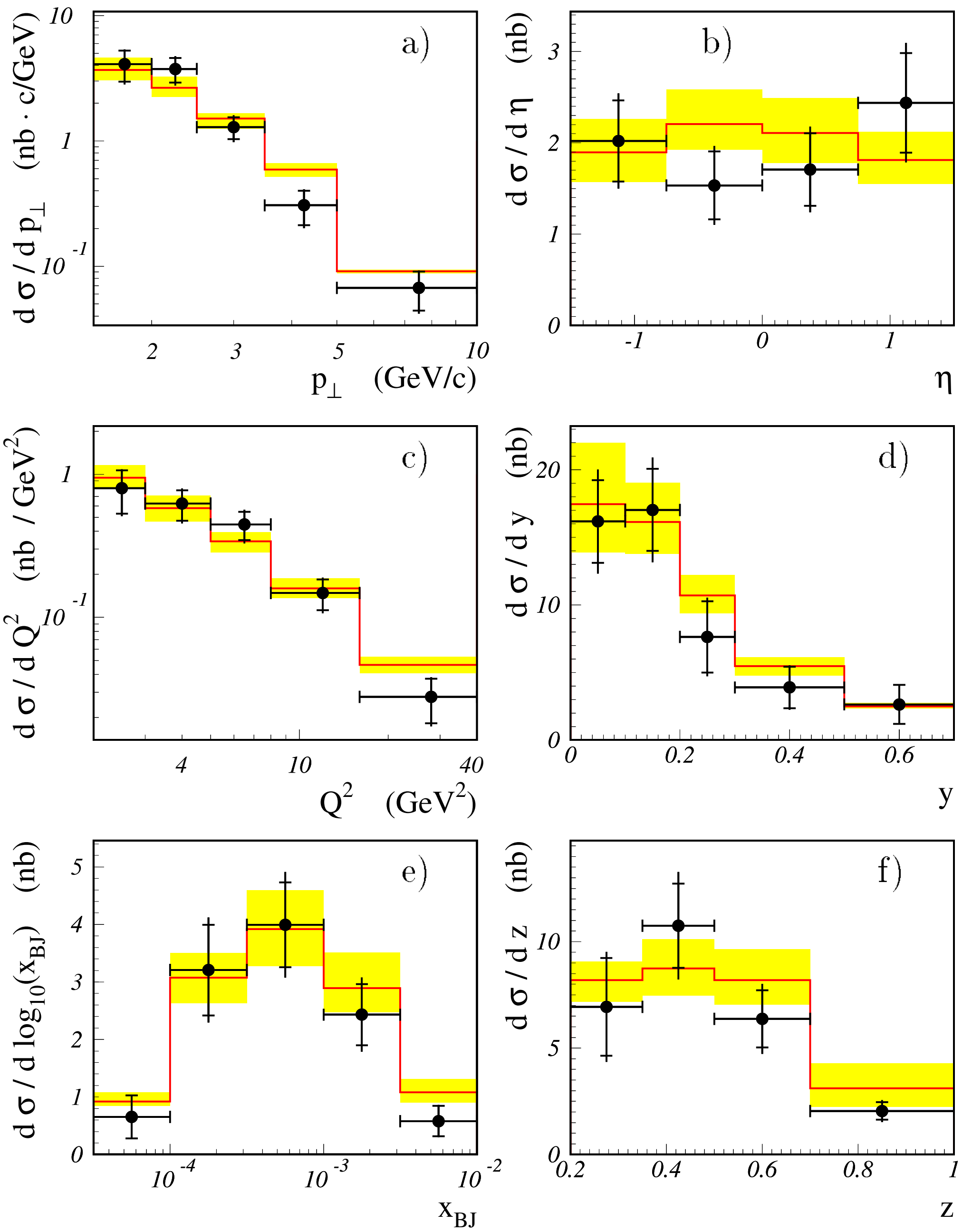

Figure 4.17: *Measured differential cross sections. The data are represented by the full points with the inner error bars according to the statistical errors. The outer error bars indicate the total errors with the systematical errors added in quadrature. The grey line shows the prediction by HVQDIS using the CTEQ4F3 gluon density, with the error band indicating the differences when the charm quark mass is varied from 1.3 GeV/c^2 to 1.7 GeV/c^2 .*

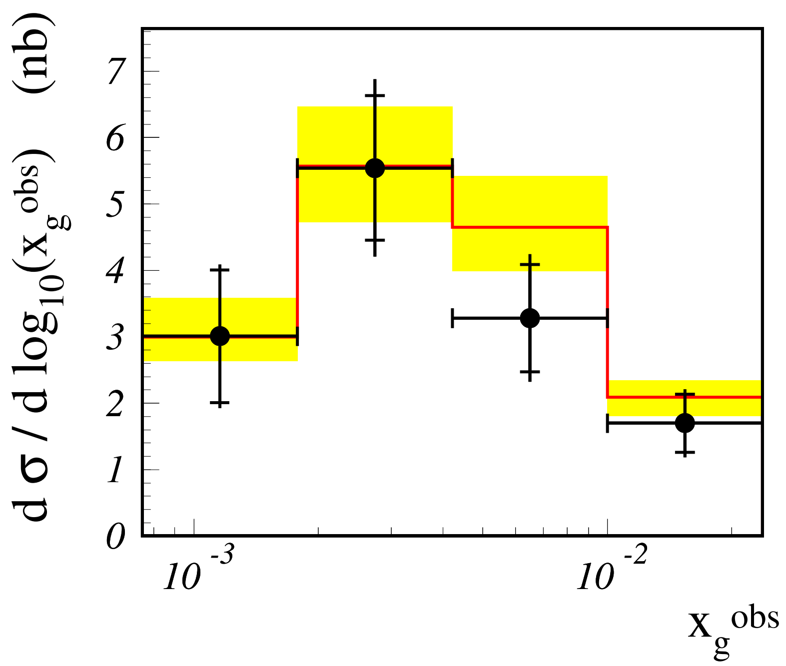

Figure 4.18: *Measured cross section as a function of log(x_g). The data are represented by the full points with the inner error bars according to the statistical errors. The outer error bars indicate the total errors with the systematical errors added in quadrature. The grey line shows the prediction by HVQDIS using the CTEQ4F3 gluon density, with the error band indicating the differences when the charm quark mass is varied from 1.3 GeV/c^2 to 1.7 GeV/c^2 .*

4.6.1 Comparison of the results obtained with the electron and with the $e\Sigma$ method

Since we have two largely independent methods to reconstruct the DIS kinematics at our disposal, we can of course check one against the other. The full analysis – including radiative corrections and evaluation of the systematic errors – has therefore been repeated for the electron method as well. The visible range has been tightened to $0.05 < y < 0.7$ for this comparison. The obtained results are overlaid in Figure 4.19 . The mean χ^2 has been calculated using the statistical errors only. The 'photon related' quantities such as y, x_g and x_{Bj} show similar χ^2 values as the $p_\perp$, η and Q^2 distributions where differences can only originate from differences in the event selection.

Table 4.9 lists the number of events accepted by only one of the two

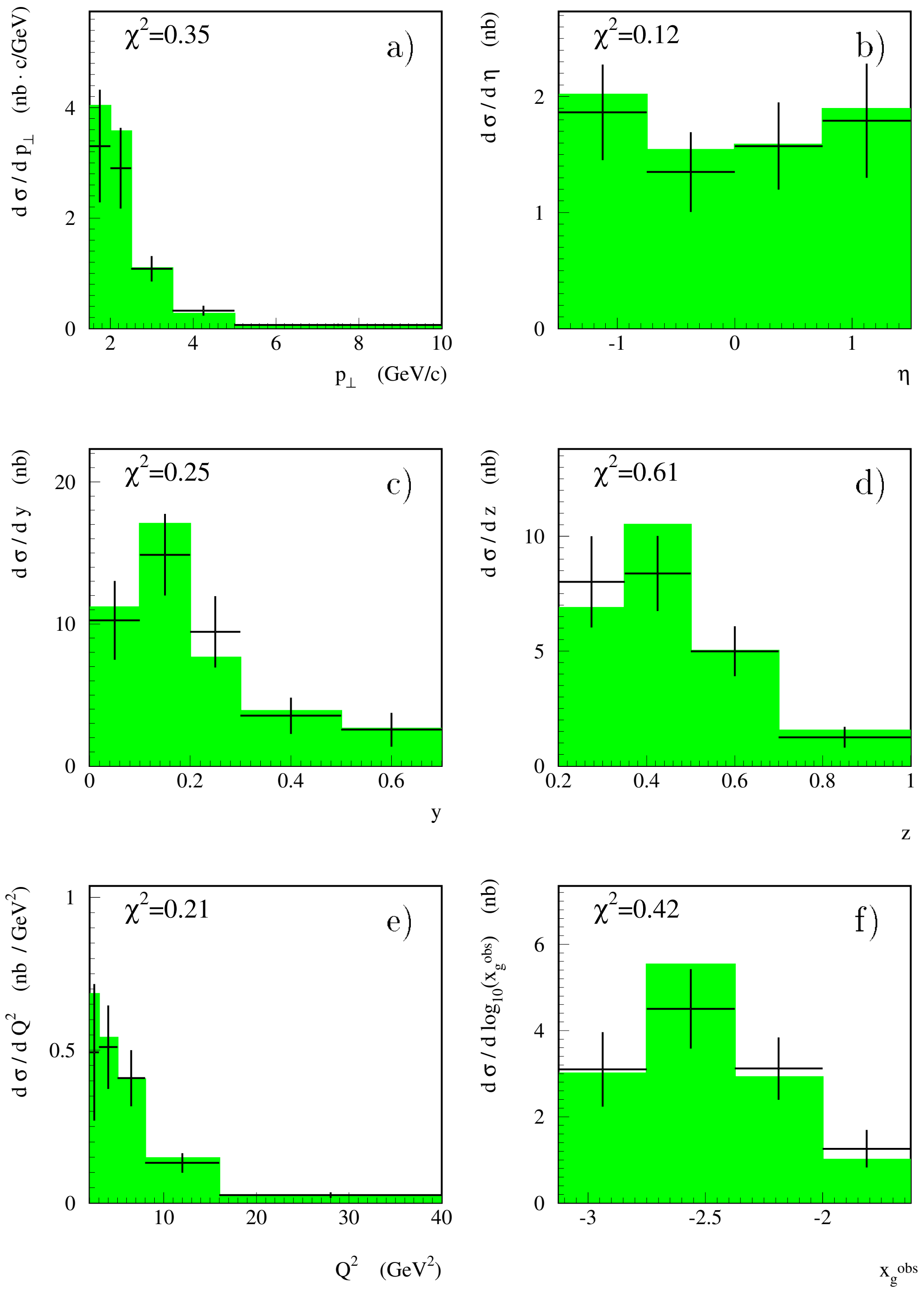

Figure 4.19: *Comparison of the results the electron (crosses with statistical errors) and the $e\Sigma$ (grey histogram) method. The mean χ^2 has been calculated using the statistical errors only.*

	Number of events		Result of fit	
	ele. acc.	ele. rej.	ele. acc.	ele. rej.
$e\Sigma$ acc.	1065	142	129.2	15.4
$e\Sigma$ rej.	86		12.0	

Table 4.9: *Differences between electron and $e\Sigma$ method in the event selection.*

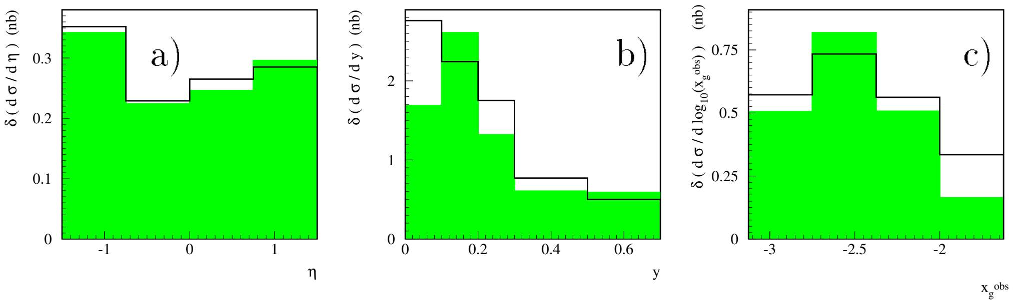

Figure 4.20: *Comparison of the total systematic error for the electron (black lines) and the $e\Sigma$ method (grey histograms). The distributions may show some fluctuations as all the contributions — including e.g. the variation of the peak width — have been been calculated for every bin separately. The large uncertainty for the electron method in the low y bin is of course due to bad resolution. The uncertainties of the electron method are larger than those from the $e\Sigma$ method for $0.2 < y < 0.5$ due to the large radiative corrections.*

methods. 135 out of the 228 events accepted by only one method lie in the interval $0.15 < z_{D^\star}(electron) < 0.25$. A comparison of the obtained systematic errors is given in Figure 4.20 .

Chapter 5

From the Cross Section to the Gluon Density

In Section 2.3.5 it has been shown that a NLO description of the γ–*gluon* fusion process and the subsequent hadronization process is available. Based on these calculations, we know for every 'event' the generated gluon momentum ($\rightarrow x_g^{true}$) as well as its approximation calculated from the hadronic final state ($\rightarrow x_g^{obs}$). Figure 5.1 a) shows the correlation between these two values. If the correlation matrix is normalized it can be understood as a smearing matrix which describes the migration of events from the *true* to the *observed* bin. For our measurement we need of course the opposite transformation, which takes the differential cross section as a function of x_g^{obs} as input and delivers the cross section as a function of x_g^{true}.

The first intuitive solution of this problem, matrix inversion, does not give reasonable results. Inversion of the smearing matrix is not necessarily possible and if so, it is very sensitive to statistical fluctuations of the matrix. In addition, the inversion of the positive definite smearing matrix leads to negative matrix elements and these may result in negative numbers for the unfolded distribution. Elaborate techniques to get around these problems have been presented e. g. in Reference [54] . A different procedure has been used in this analysis. It will be explained in Section 5.1 , its application to the case of our measurement is shown in Section 5.2 .

5.1 An unfolding method based on Bayes' theorem

We use an unfolding method introduced in Reference [63]. All evaluations shown in the following were made with a program furnished by the author of References [63, 64].

The advantages which triggered the choice of this method are:

- It allows the use of different binnings and domains of definition for observed and true distributions[1].
- It provides the correlation matrix of the result.
- It is easy to use.
- It has already been used by previous H1 analyses.

The procedure can be explained as follows: We start from a set of *causes* $(C_i, i = 1..n_C)$[2]. Due to these causes, we will observe *effects* $(E_j, j = 1..n_E)$[3]. Let us assume that we know the *initial probabilities* $(p(C_i) \equiv p_i)$ that the causes C_i occur and the *conditional probabilities* $(P(E_j|C_i) \equiv P_{ji})$. The conditional probabilities tell us how probable it is that we will observe the effect E_j if cause C_i has occurred. The full set of conditional probabilities is often referred to as *smearing matrix*. Bayes' formula tells us now, how to turn around the conditional probabilities:

$$\hat{P}(C_i|E_j) \equiv \hat{P}_{ij} = \frac{P_{ji} \cdot p_i}{\sum_{k=1}^{n_C} P_{jk} \cdot p_k} \,. \tag{5.1}$$

I.e. the probability $\hat{P}_{ij}$ that the effect E_j appeared due to the cause C_i is proportional to the corresponding conditional probability times the initial probability that cause C_i occurred.

[1] In the final version of the analysis, we did not use that feature.

[2] In our case a cause corresponds to the gluon momentum being generated in a specific bin.

[3] In our case an effect corresponds to the observable gluon momentum being expected in a specific bin.

The normalization factor in the denominator guarantees that

$$\sum_{i=1}^{n_C} \hat{P}_{ij} = 1 \ , \tag{5.2}$$

which means, that every effect has in total one reason. Note that this implies that all possible reasons for the effect, even background, must be included in the set of causes.

On the other hand only the weak condition

$$0 \leq \epsilon_i \equiv \sum_{j=1}^{n_E} P_{ji} \leq 1 \ , \tag{5.3}$$

must be fulfilled. This sum is the probability, that C_i leads to any of the considered effects and can therefore be understood as the probability that the cause C_i is detected by the measurement. It is the efficiency of the experiment.

The relation between the probabilities and the correlation matrix is obvious. Let us assume that we have generated n events with their distribution over the bins of the *causes* (x_g^{true}) given by the variables $\hat{n}(C_i) \equiv \hat{n}_i$, while $n(E_j) \equiv n_j$ describes the number of events detected in bin j (*effect* / x_g^{obs}). The entries of the *correlation matrix* $N(E_j|C_i) \equiv N_{ji}$ are then given by the number of events which are observed with effect E_j due to cause C_i. Initial- and conditional probabilities can now be calculated as

$$p_i = \frac{\hat{n}_i}{n} \ , \tag{5.4}$$

$$P_{ji} = \frac{N_{ji}}{\hat{n}_i} \ . \tag{5.5}$$

If we observed in an experiment $n(E_j)$ events with effect E_j, we may conclude that the number of events with cause C_i must have been:

$$\hat{n}_i = \frac{1}{\epsilon_i} \sum_{j=1}^{n_E} n_j \cdot \hat{P}ij \equiv \sum_{j=1}^{n_E} n_j \cdot M_{ij} \ . \tag{5.6}$$

The factor $1/\epsilon_i$ is necessary, because the selection of data events requires the effects to lie within the limited range accepted by the measurement.

In equation 5.6 we have defined the *unfolding matrix* M_{ij} through:

$$M_{ij} = \frac{1}{\epsilon_i} \cdot \hat{P}ij \equiv \frac{P_{ji} \cdot p_i}{\sum_{t=1}^{n_E} P_{ti} \cdot \sum_{k=1}^{n_C} P_{jk} \cdot p_k} \ . \tag{5.7}$$

What are the critical points if we want to use this matrix to unfold our measured cross section? The calculation of the conditional probabilities only requires good knowledge of the smearing process which is in our case the NLO processes and the hadronization of the generated charm quarks into $D^\star$ mesons[4]. The occurrence of the initial probabilities in Equation 5.7 however is very worrying. They directly depend on the gluon density which was input to the NLO cross section calculation. So the unfolding depends on a prediction of exactly the quantity we want to measure! Does our so called 'measurement' therefore not just reproduce the input distribution? It will be shown in the next paragraph, that this bias influences the results only in a minimal way which furthermore can be estimated from the data.

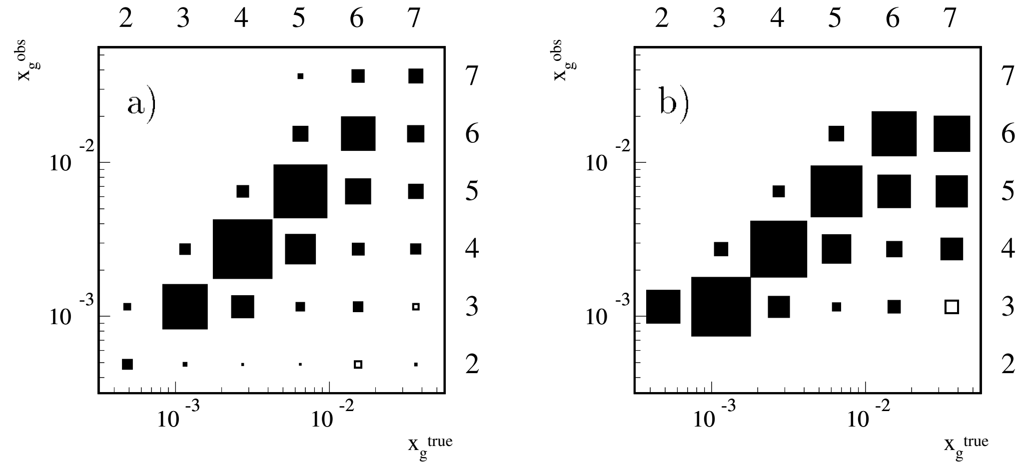

Figure 5.1: *Starting matrices of the unfolding procedure: a) Correlation matrix. b) Conditional probabilities calculated from a). The restriction to 4 bins of $log(x_g^{obs})$ corresponds to the limited range of our measurement. Open boxes indicate negative numbers (see text).*

The bias induced by using initial probabilities is strongly suppressed by iterating the unfolding. We start with gluon densities given by any reasonable parametrization. The unfolding is then repeated several times, calculating the

[4]Uncertainties in the calculation of that process (e. g. different fragmentation functions) were accounted for by unfolding with correlation matrices obtained with different parameter settings. The differences between the results have been used to determine the systematical error.

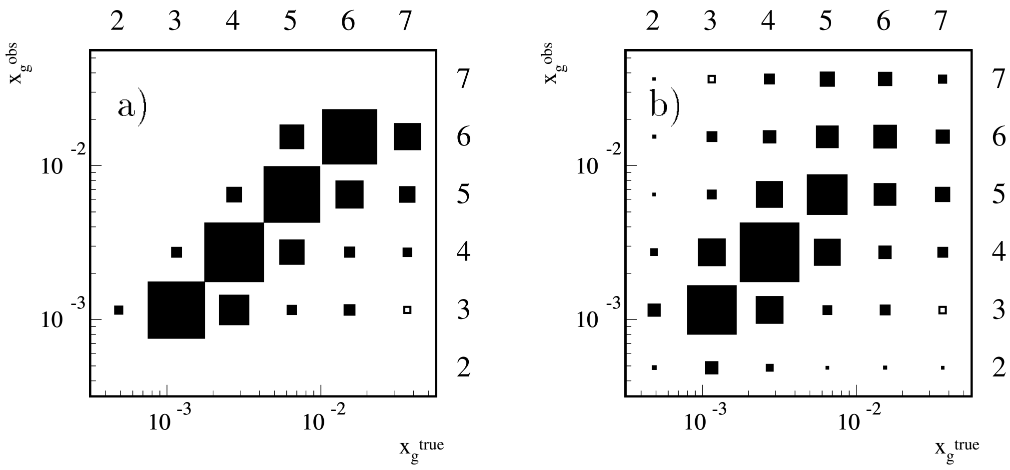

Figure 5.2: *The matrices resulting from the unfolding procedure: a) Unfolding matrix. b) Covariance matrix. Open boxes indicate negative numbers.*

initial probabilities from the data unfolded through the result of the previous iteration step. With this procedure the importance of the initial probabilities decreases step by step. Too many iterations however bear the risk that statistical fluctuations of the data lead to unreasonably high fluctuations in the unfolded distribution. It is therefore recommended [63] to parameterize the results of every iteration step and to use the resulting smooth functions as input to the next iteration. This however is not necessary in our case with only four bins and has therefore not been done. In Section 5.2 it will be shown that the procedure leads to very satisfying answers to our question, if four iterations are done. The systematic error due to this bias from the initial probabilities has been estimated by the difference between the last and the last but one iterations and can be neglected.

To summarize we can say that the procedure described allows us to find an input distribution, which, when folded with the smearing matrix, reproduces the observed data. The result of the unfolding only depends on the description of the smearing process but is independent of the initial probabilities.

Propagation of uncertainties

Up to now the statistical errors of the four measured cross sections in x_g^{obs} have been uncorrelated. This is not the case any more for the unfolded

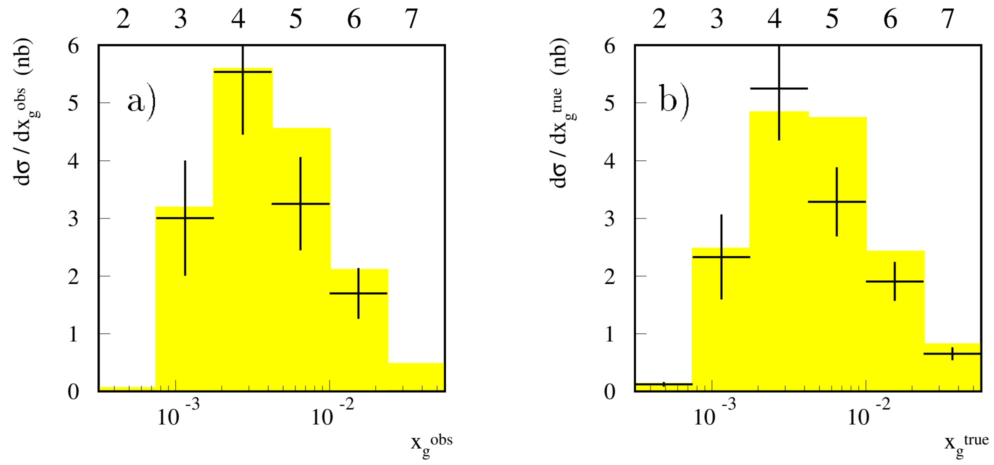

Figure 5.3: *Comparison of the differential cross sections of data (black crosses) and theoretical prediction (grey histogram), a) as a function of* x_g^{obs} *and b) as a function of* x_g^{true}*. The errors shown for the unfolded data are the square roots of the diagonal elements of the covariance matrix only.*

distribution, since every bin of x_g^{true} has received information from several points of the measurement. Fluctuations of one measured point lead therefore to a simultaneous movement of several points of the unfolded cross section. We therefore need to calculate the full covariance matrix through:

$$V_{ij} = \sum_{k=1}^{n_E} M_{ik} \cdot \delta n_k \cdot M_{jk} \cdot \delta n_k \ , \tag{5.8}$$

with δn_j being the absolute statistical error of the input quantity n_j. Note that this formula only holds, if the uncertainties of the n_j are completely uncorrelated. From the covariance matrix we can further calculate the correlation coefficients which are defined as

$$C_{ij} = \frac{V_{ij}}{\sqrt{V_{ii} \cdot V_{jj}}} \ . \tag{5.9}$$

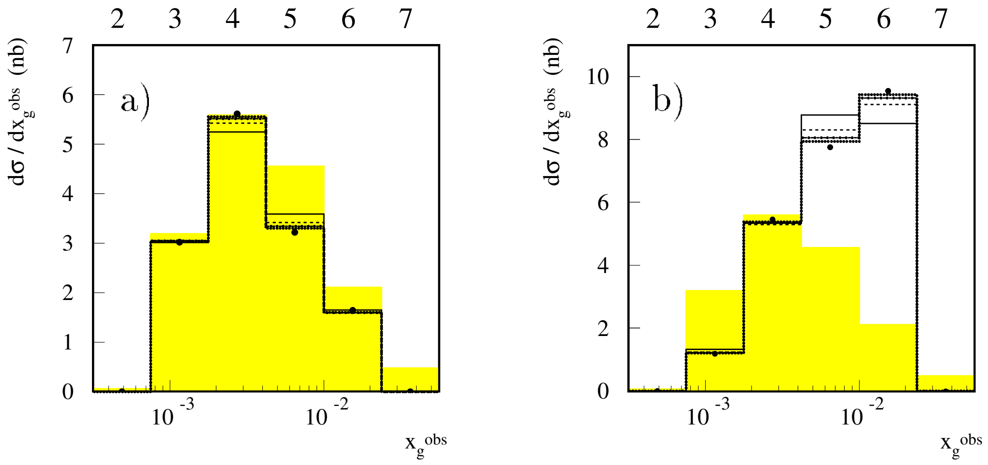

Figure 5.4: *Comparison of the results of different iteration steps of the unfolding. a) The result of the unfolding has been smeared again according to the correlation matrix. The dots are the measured data, the grey histogram indicates the prediction used to determine conditional- and initial probabilities. The lines show the re-smeared results after 0 (solid), 1 (dashed), 2 (dash dotted) and 3 (dotted) iterations. b) Convergence of the method for an extreme difference between predicted and measured distribution - the data points have been set to random values, the lines show the results after 0, 4, 8 and 12 iterations.*

5.2 Unfolding of the measured cross section

In this section we will show how the unfolding method introduced above has been applied to our measured cross section. Even though we measured the cross section only in 4 bins, the unfolding has been calculated using 10×10 bin matrices in order to keep control of possible long distance correlations. The bins of the measurement correspond to bins $\sharp 3 - \sharp 6$, the plots in this section will always show bins $\sharp 2 - \sharp 7$.

Figure 5.1 a) shows the starting point of the unfolding, the correlation matrix. Note that a few bins with negative entries are present. This is due to the character of the used NLO calculation which does not generate events in the usual sense but only 'contributions to cross sections' with event weights that may be positive or negative[5]. The conditional probabilities derived from this correlation matrix are shown in Figure 5.1 b). The matrices obtained

[5]Note that the *observable* cross section $d\sigma/dlog(x_g^{obs})$ is *always positive*.

after four iterations are shown in Figure 5.2 . The unfolding of the measured data points through this matrix is shown in Figure 5.3 b).

It is interesting to see, that bin ♯6 (the last bin of the measured range) is about one standard deviation below the prediction for the observed cross section. For the unfolded cross section, it is significantly further below the predicted value. This effect may partly be explained with the underestimation of the error bars: it is impossible to show correlated errors on a plot. We therefore follow the usual convention and show the square root of the diagonal elements of the covariance matrix as error bars which is reasonable as long as the correlation between different bins is small. The influence of the neighboring bin ♯5 is however relatively strong. The statistical error of bin ♯6 is therefore underestimated.

The correlation coefficients of the unfolded data points are given in Table 5.1 . The off–diagonal elements are in general small, as it was intended when x_g^{obs} was defined in Section 2.3.3 . Therefore we may speak of a *local measurement* where every data point in Figure 6.1 depends on almost only one of the measured data points.

	bin j			
bin i	3	4	5	6
3	1.00			
4	0.24	1.00		
5	0.03	0.28	1.00	
6	0.077	0.10	0.50	1.00

Table 5.1: *Correlation coefficients of the unfolded data points.*

5.3 Results

The cross section distribution $d\sigma/dlog(x_g^{true})$ is directly related to the gluon density in the proton via

$$\frac{d\sigma_{(ep\to D^\star X)}}{dlog(x_g^{true})} = BR_{(c\to D^\star)} \cdot \frac{d\hat{\sigma}_{(eg\to cX)}}{dlog(x_g^{true})} \cdot g(x_g) \ , \qquad (5.10)$$

where $\hat{\sigma}$ denotes the partonic cross section for the γ–*gluon* fusion process as calculated by the program *HVQDIS* and includes the event losses due to the cuts on the visible cross section as well as the $e\gamma$ vertex. The equation can naturally be used to calculate the gluon density $g(x_g)$ from the measured cross section. The result is shown in Figure 6.1 and compared to a more indirect measurement of the same quantity.

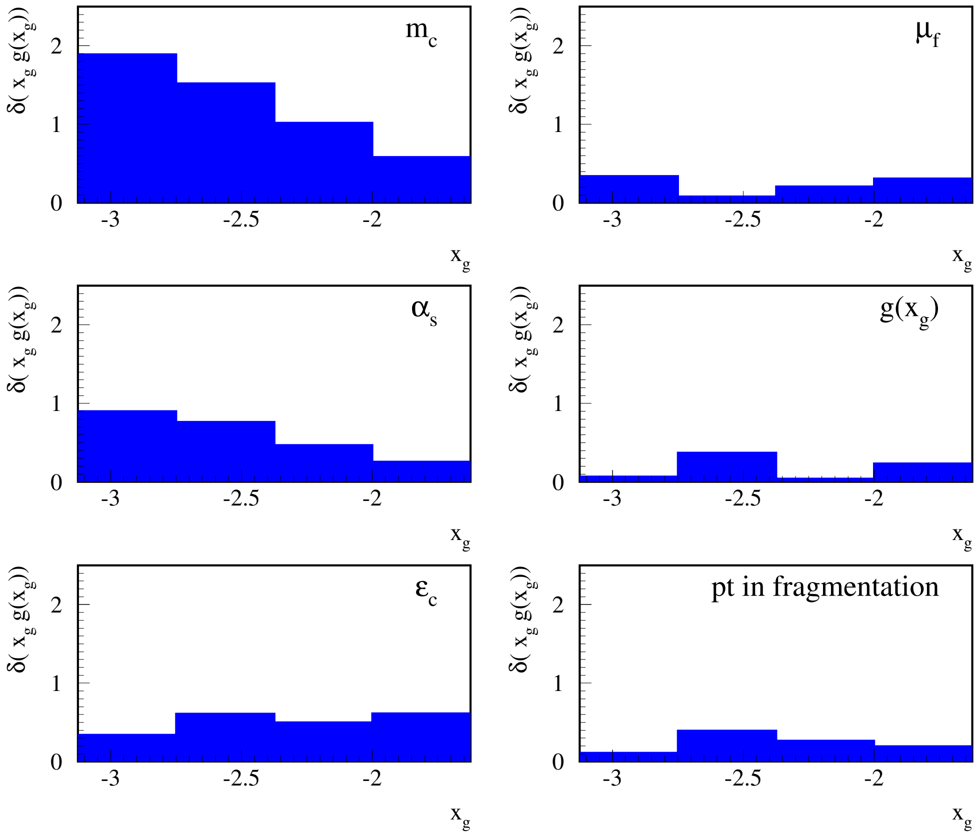

Figure 5.5: *Systematic uncertainties in the calculation of $g(x_g)$, from [65, 66], see text.*

A series of systematic uncertainties in the *HVQDIS* calculation have to be taken into account now as well.

- Uncertainties in the charm quark mass m_c have a strong influence on the partonic cross section since our kinematical regime is very close to the threshold for charm production. m_c also enters in the *QCD* scales μ_f^2 and μ_r^2 used in the calculation. The mass of the charm quark has been varied from 1.3 GeV/c^2 to 1.7 GeV/c^2 . This effect is the main contribution to the systematic error of the calculation.

- Only a small error arises from variations of the scales μ_f^2 and μ_r^2 from $4m_c^2/c^2$ to $4(4m_c^2 + Q^2)/c^2$.

- Uncertainties in the value of α_s are taken into account by variation of the scale Λ_{QCD}^5 from 176 MeV to 248 MeV.

- The unfolding procedure depends on an input distribution of the gluon density. The difference of the results obtained using the MRS(D0) and the MRSA' parametrizations has been used as an estimate of that systematic error. The MRS(D0) parametrization is already ruled out by measurements [15] and both are inconsistent with the *Three Flavor Number Scheme* used in the calculation. However the difference between these two parametrizations is bigger than between $CTEQ4F3$ and other more recent parametrization. Therfore we can only overestimate the systematic error with this choice. Only small variations of the result were found.

- Different settings of the Peterson fragmentation parameter as indicated in Figure 2.10 have been used.

- A different description of the fragmentation process has been used, giving the $D^\star$ meson a momentum contribution perpendicular to the direction of the charm quark. Randon numbers according to a Gaussian distribution with a width of 350 MeV/c have been used for the simulation of this momentum component.

Chapter 6

Conclusions

The obtained values of the gluon density of the proton at the scale $\mu_f^2 = 25$ GeV^2 are shown in Figure 6.1 with the statistical and systematical errors. The statisical uncertainties are still large and an analysis of the data collected after 1995 will certainly improve the accuracy of the measurement. The systematic error is dominated by the uncertainty of the charm quark mass which is used in the *NLO* calculation. On the experimental side, a large error arises from the uncertainty of the width of the $\Delta_m = m_{D^\star} - m_{D^0}$ peak. More events will help to determine that value more accurately. The operation of the *SpaCal* has been much better understood in the following years, which allows a better measurement of the scattered positron. However the *CJC* started to suffer from ageing effects in 1996 which might increase the uncertainties from the track finding.

The obtained gluon density is compared to the result of a recent H1 analysis of the scaling violations of the structure function F_2 [67], shown by the grey band in Figure 6.1 (see Section 2.2.3).

Even though the two measurements have been carried out at the same experiment, they may be considered to be completely independent since there is only very little overlap in the used data samples and completely different methods have been applied to extract the gluon density from the data. The observed agreement is a good confirmation of the universality of the gluon density function and of the theoretical concepts used.

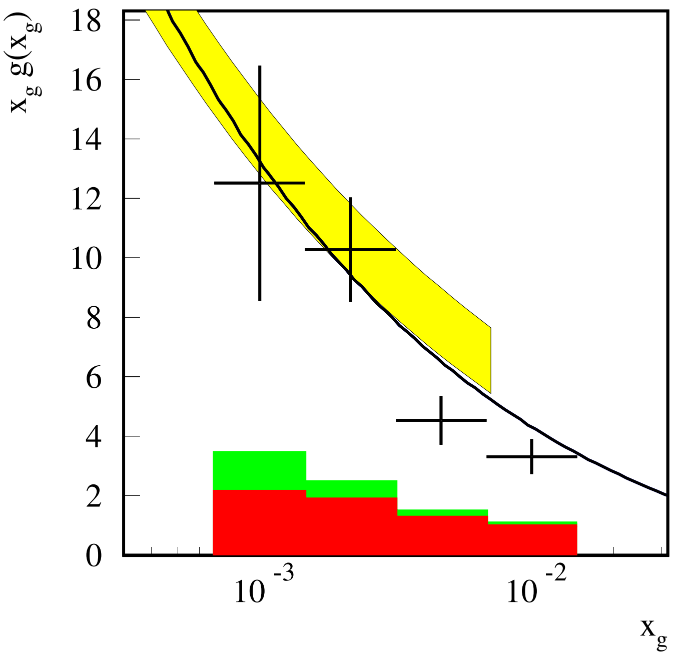

Figure 6.1: *Measured $x \cdot g(x_g)$ at the scale $\mu_f^2 = 25\ GeV^2$. The error bars on the data points give the statistical errors (diagonal elements of the covariance matrix). The dark histogram at the bottom indicates the quadratic sum of the systematic errors from theory, for the light histogram the experimental systematics have been added in quadrature. The line shows the CTEQ4F3 parametrization [30] and the shaded area represents the gluon density obtained from measurements of the scaling violations of F_2 at H1 [67]. Good agreement between the completely independent measurements is found.*

$log(x_g^{true})$	-3.125	-2.75	-2.375	-2.0	-1.625
$x_g \cdot g(x_g)$	12.5	10.3	4.54	3.32	
$\pm$ stat	4.0	1.8	0.83	0.59	
$\pm$ syst exp.	2.7	1.6	0.77	0.44	
$\pm$ syst theor.	2.2	1.9	1.28	0.99	
$\pm$ syst total	3.5	2.5	1.49	1.08	

Table 6.1: *Measured gluon densities and its error sources. For simplicity the asymmetric systematic errors have been averaged.*

Appendix A

The zVtx–trigger

A.1.1 Introduction

The *z–Vertex–trigger* is based on the multiwire proportional chambers *CIP*, *COP* and the first double-layer of the *FPC*. Due to the good time resolution (for *CIP* a FWHM of 21 ns has been measured), the *zVtx*–trigger is used to determine the correct HERA bunch crossing of an event, which is very important in order to stop the pipelines of the front–end electronics at the correct moment.

The signals of the cathode pads of each of the 16 ϕ–segments are first processed on their own. Figure A.1 shows that every straight particle track within the angular acceptance of the trigger passes through four layers of *MWPC*. If we find in an event that the corresponding four pads have fired, we have to assume that this happened due to that track. Electronically, this means that a four-fold coincidence called '*ray*' fires[1]. This apparent track can be extrapolated to the beam axis where it measures the z–coordinate of the vertex. Of course accidental coincidences may occur as well. The z–vertices of the 'good' coincidences should cluster whereas the accidentals are expected to form a flat background. The nominal interaction–region is therefore divided into 16 *zVtx*-bins with a length of 55 mm each. The logical circuitry including all rays originating from one bin is realized on a single printed circuit board, the *Rayfinder Card*. 16 *Adder Cards* sum the number of rays found in the 16 ϕ segments of every bin. The resulting trigger histogram is then fed into the *Vertex Finder Card* where the total number of active *rays* (*sum*) as well as the

[1] A *3_of_4 option* allows to preset dead pads and to retain the trigger efficiency if one layer of the *MWPC* is damaged.

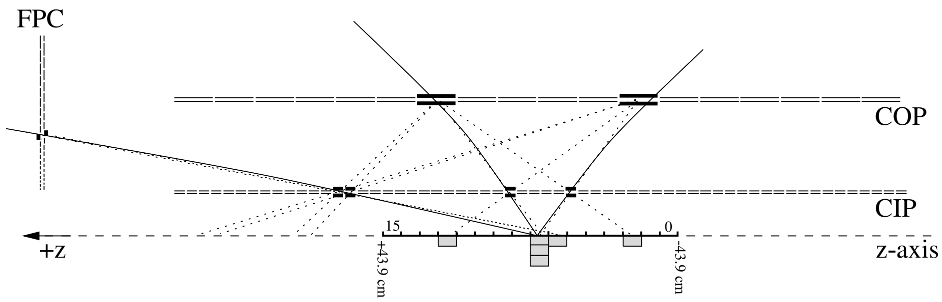

Figure A.1: *Principle of the* zVtx *trigger, see text for explanations.*

chamber	CIP		COP		FPC	
layer	inner	outer	inner	outer	first	second
segments in ϕ	8		16		inner pads: 8 outer pads: 16	
segments in $z(r)$	60		18		(20)	(19)
position in z [mm]	-1125..1065		-1107..1065		1451	1463
radius [mm]	157	166	501.5	514.5	167.5..750	

Table A.1: MWPC *geometry. The two layers of* CIP *and* FPC *are rotated one to the other by 1/16 in order to achieve a pseudo 16-fold segmentation.*

content of the highest bin (*peak*) and its position (*peak_pos*) are calculated. The results are transmitted to the *RAM Card*, a large look-up-table from where eight *trigger elements* are sent to the central trigger logics.

The hardware realization using a freely programmable RAM card for the definition of the trigger elements is very flexible and allows to change the definition of the *zVtx*–trigger elements repeatedly without having to touch a soldering iron. The 4MB RAM can be addressed by a 22 bit number which is composed of *peak* (8 bits), *sum* (12 bits) and two additional *quality bits*: the *cluster bit* is active if all entries in the histogram cluster in four adjacent bins[2]. The *edge bit* is a veto which is set if the peak has been found in

[2]As it is a trigger element determined on the Vertex Finder Card already, it passes the RAM Card unchanged.

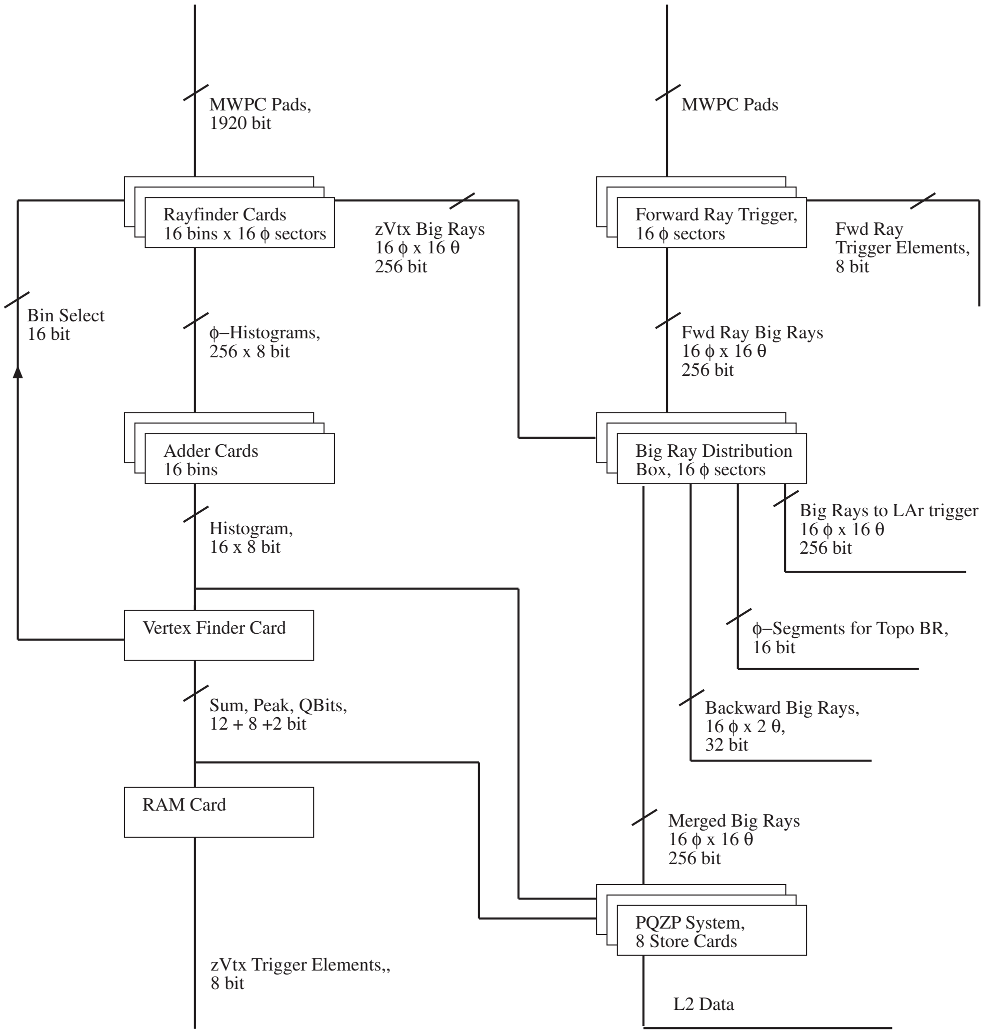

Figure A.2: *Data–flow in the MWPC trigger electronics. All signals travel from top to bottom, except the 'Bin Select' which goes from the Vertex Finder Card back to the Rayfinder Cards in order to enable the output of the Big Rays originating from the peak bin and its neighbors.*

Significance	Required trigger elements		
	95	96	97/98
σ_μ_D	N. A.	N. A.	$30 \vee 31$
σ_1	30	$30 \vee 31$	31
σ_{NET}	31	$30 \wedge 31$	$30 \wedge 31$

Table A.2: *Mapping of significance criteria on* L1 *trigger elements for different running periods.*

the first two or the last two bins of the histogram, i. e. outside the nominal interaction–region.

Detailed descriptions of the technical realization of the *zVtx*–trigger can be found in References [68, 69, 12].

A.1.2 Significance bits

The σ_1–condition makes use of the possibility to program the RAM card according to any mathematical formula. It is active if a significant peak has been found according to

$$\sigma\_1 \equiv \frac{P-B}{\sqrt{P}} > 1.5 \; , \tag{A.1}$$

where P is *peak* and B gives the average number of entries in the other ('Background') bins.

The reason for defining a new condition (σ_μ_D), which accepts more events with small *sum* will be shown in Section A.1.3 . The σ_μ_D condition, used for the first time in the 1997 data taking, is given by

$$\sigma\_\mu\_D \equiv \sigma\_1 \;\; \vee \;\; (6 \cdot peak > sum + 3) \; . \tag{A.2}$$

A much tighter cut on the significance of the peak in the histogram is defined through the σ_{NET} condition which has been optimized for the triggering of leptonic decays of J/ψ mesons [70].

All three σ conditions are vetoed by the *edge bit*, i. e. we require that the significant peak lie within the nominal interaction–region.

The three significance thresholds are encoded in two trigger elements according to Table A.2 .

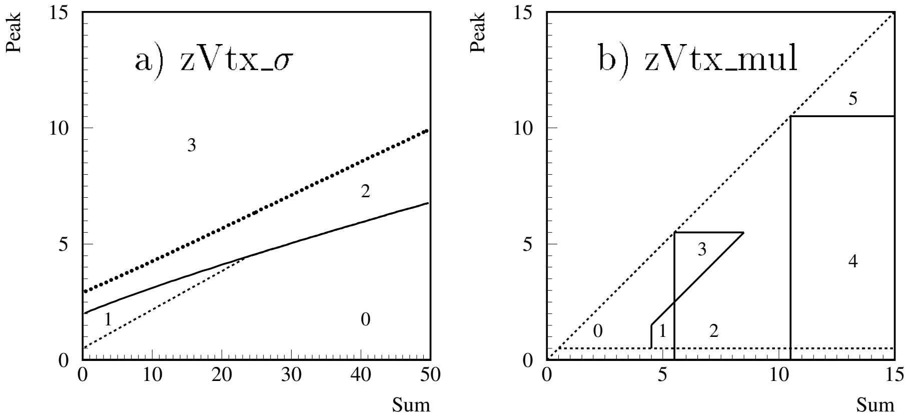

Figure A.3: *a)* zVtx *significance criteria plotted in the plane* peak *versus* sum*: σ_1 (solid line), σ_μ_D (dashed line, equivalent to σ_1 for sum > 20), σ_{NET} (dotted). Events with a peak greater than indicated by the plotted functions are kept. b) Definition of the regions encoded in the multiplicity bits. The dotted lines bound the mathematically possible range. See text for further explanations.*

A.1.3 Optimization of the significance criterion for D* in DIS events

For the 96 running period, $D^\star$–triggers were tightened by applying the σ_1 condition. From Figure A.4 it can however be seen, that this rejected too many of the good events with only few tracks in the central tracker[3]. The significance criterion had therefore been modified for the 97 data taking, relaxing it for events with a peak-value of less than 5 entries in the *zVtx*–trigger histogram, the new σ_μ_D–condition. The rate increased only moderately due to these additional events which could be tolerated because these events with only few particles in the central detectors represent a small data volume (Table A.3)[4].

[3]In 96 several dead channels of the central proportional chambers *CIP* and *COP* caused an additional inefficiency as their effect could not be compensated through the 3_of_4 option of the *zVtx*–trigger. Several layers have been damaged in the same ϕ –sectors due to a water leak in another detector part.

[4]The possibility of further improvements based on an active recognition of tracks from upstream vertices has been studied in Reference [36]. In principle, the number of track candidates found by that new device could be – at the cost of some of the accuracy for *sum* and *peak* – fed into the RAM card and used for the definition of some even more

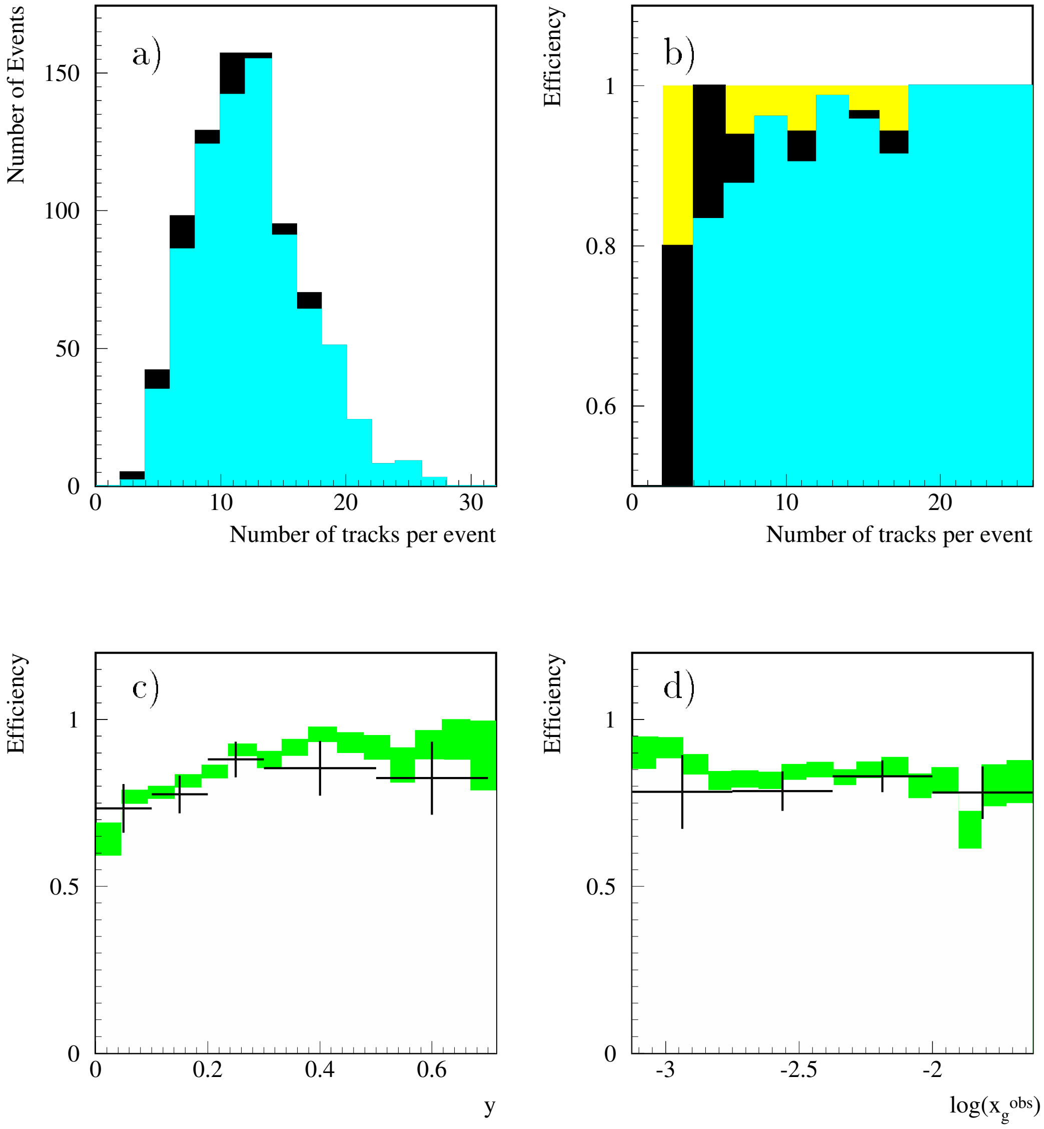

Figure A.4: zVtx–*trigger efficiency evaluation: a) Black histogram: the number of $D^\star$ in DIS events 1996 from an independent subtrigger as a function of the total number of tracks in the* CJC*; grey histogram: events which fulfilled the σ_1 condition. b) Efficiency of the σ_1 (dark grey) condition as a function the number of* CJC *tracks. The black area indicates the increase in efficiency, if the σ_μ_D condition had been used instead. c), d): Efficiency of the σ_1 condition versus $y_{e\Sigma}$ and log(x_g). The black crosses represent the values obtained from 96 data using a largely independent trigger (ST_1). Inefficiencies have been measured by a Δm–fit to the rejected events. The grey area represents the error bars of the values found in the Monte Carlo description.*

Condition	Efficiency for $D^\star$ in DIS		Rate reduction with $r\phi$–t_high		Bandwidth reduction with $r\phi$–t_high	
	$zVtx$ alone	with $r\phi$–t_high	t_0 ok	late	t_0 ok	late
σ_1	77 %	75 %	61 %	68 %	43 %	56 %
σ_μ_D	93 %	89 %	47 %	58 %	31 %	46 %

Table A.3: *Efficiency for the two significance criteria together with an $r\phi$–trigger condition, as derived from the 96 $D^\star$ in DIS data. The rate reductions have been determined from two runs with no event rejection at the higher trigger levels, using ST_1 (see Section 4.2.2). The relative consumptions of bandwidth have been estimated by counting the number of hits in the* CJC *of all the events accepted by the according trigger condition. Based on the event timing from the track fits, the data sample has been divided into events consistent with nominal beam–beam interaction (t_0* ok*) and a second sample containing the events arriving too late, most probably originating from the late satellite of the proton beam.*

Determination of the efficiency of the σ_μ_D–trigger condition for D* events in data and MC

Figure A.4 c) shows that the efficiency of the σ_1 condition drops significantly with decreasing y. This effect is ascribed to the increasing number of tracks passing at low angles through the detector. Since the momentum of the photon in the negative z–direction is approximately proportional to y, the boost of the events in forward direction tends to increase with decreasing y. Tracks going moderately forward pass through *CIP* and *FPC*. The forward *rays* have a poorer resolution on their origin on the z–axis than the central *rays* defined by *CIP* and *COP*. Therefore events dominated by central tracks yield a better peak to sum ratio in the trigger histogram and hence a better efficiency for the σ conditions. This behavior is – even though less pronounced – reflected in the efficiency curve as a function of $log(x_g^{obs})$ (see A.4 c)). A correct description of this inefficiency is thus vital for the analysis of the 96 data.

---

elaborate significance criterion. A combination of that new system with the $zVtx$–trigger on the level of trigger elements however showed almost equal results and would therefore certainly be preferred.

For the comparison, Monte Carlo events have been preselected in order to be comparable to the data sample which originates from ST_1: cuts on Q^2 and ϕ were indirectly applied by cutting away an asymmetric region around the beam pipe in the *SpaCal*. To make sure that we do not compare the *MC* result to the potentially different trigger efficiency for background events in the data, a fit to the mass peak has been used in order to determine the efficiency for $D^\star$ events in the data. Good agreement is found within the error bars. Since the higher statistics of the *MC* allow a finer binning, e. g. in y, I suggest to use the simulation to calculate event losses in the 96 $D^\star$ analyses.

A.1.4 Multiplicity bits

Three trigger elements are used to encode a *multiplicity code* for every event. The code can be calculated from the trigger elements as:

$$mul = TE(26) + 2 \cdot TE(27) + 4 \cdot TE(28)\ . \tag{A.3}$$

The assignment of the multiplicity code to the regions in the plane *peak* versus *sum* can be seen in Figure A.3 . Regions 4 and 5 extend up to $sum = 100$, where region 6 starts (for all values of *peak*). Region 7 covers $sum > 250$ and is used in several subtriggers as a veto against huge upstream background events.

year	1994/95		1996/97				
θ index	used code	0..13	used code	0..3	4	5	6..13
code 00		AND		F	OR	OR	C
code 01		OR		F	OR	C	C
code 10		F	•	F	F	OR	C
code 11	•	C		F	F	F	C

Table A.4: *Merging between forward and central BigRays. The 'code' is loaded into the hardware together with the forward ray–trigger and accessible offline via the 'FRTI' bank. 'F' means BigRays from the forward ray–trigger only, 'C' means zVtx–trigger BigRays; 'OR' and 'AND' are the logical combinations of both systems.*

A.1.5 Big Rays

In addition to forming the *zVtx*–histogram, the pointing–information of the *rays* is used: the solid angle has been divided in ϕ and θ by a 16×16 grid, according to the segmentation of the *LAr* calorimeter trigger. Taking into account the limited resolution, every ray points into one or more of these bins of the solid angle. The logical OR of all *rays* pointing into one bin is called a *BigRay*. A coincidence between a *BigRay* and a local energy sum in the *LAr*, called a *LAr BigRay* , is much less sensitive to electronic noise in the *LAr* than energy thresholds alone. It is realized on *L1* already. In addition, *BigRays* are used to tag the back-to-back topology of dileptonic decays of low $p_\perp$ J/ψ mesons. *BigRay* information is used on *L2* as well. The *Forward Ray –Trigger* — based on all three double-layers of *FPC* and on *CIP*— has better acceptance and resolution for forward going tracks. The *BigRay* signals from the two trigger systems are therefore merged according to Table A.4. [71].

Card nr.	word 1	word 2	word 3	word 4
i=0..3 : Big rays	$\phi = 4i$ (16bits)	$\phi = 4i + 1$ (16bits)	$\phi = 4i + 2$ (16bits)	$\phi = 4i + 3$ (16bits)
4 : *zVtx* hist.	$b_1 + 256 \times b_2$ (2× 8bits)	$b_3 + 256 \times b_4$ (2× 8bits)	$b_5 + 256 \times b_6$ (2× 8bits)	$b_7 + 256 \times b_8$ (2× 8bits)
5 : *zVtx* hist	$b_9 + 256 \times b_{10}$ (2× 8bits)	$b_{11} + 256 \times b_{12}$ (2× 8bits)	$b_{13} + 256 \times b_{14}$ (2× 8bits)	$b_{15} + 256 \times b_{16}$ (2× 8bits)
6	*peak_pos* (4bits)			
7	*peak* (8bits)	*sum* (12bits)	$edge + 2 \times cluster$ (2bits)	

Table A.5: *Assignment of* L2 *data to StoreCards.* b_i *denotes the content of histogram bin i.*

A.1.6 MWPC –trigger information on L2

The transmission of *MWPC*–trigger information to the *L2* system is achieved through the *PQZP (Parallel Quickbus Zero-suppression Processor)* system.

The data is fed into 8 *StoreCards* from where it is — as soon as the data taking is stopped by an *L1 keep* signal — transfered to the *L2L3Card* and subsequently sent to the second level triggers [72]. Every *StoreCard* can transmit 64 bits, grouped in 4 words of 16 bits.

The *BigRays* — after their merging with the forward ray –trigger information — are transmitted by 4 *StoreCards*. Two cards are needed for the *zVtx*–trigger histogram. The last two cards are only partly used and transmit the output of the *Vertex Finder Card*, i. e. *sum*, *peak*, *peak_pos* and the two *quality bits*. The assignment of the trigger information to the different *StoreCards* is given in Table A.5 .

A.1.7 Continuous check of the trigger electronics

The *zVtx*–trigger showed some instabilities at the beginning of the 95 running period. In normal conditions the electronics only need to be loaded after power glitches or if the setup of the trigger has been changed. This takes around 20 minutes.

However due to constructive interference of the cross talk from different signals on the *Rayfinder Cards*, the so–called *Program Enable* signal went above threshold occasionally. By this, the correct setup was overwritten which led to unpredictable behavior of the trigger. The problem was cured during the shutdown 95/96 by damping the *Program Enable* signal on all *Rayfinder Cards* with an RC circuit. To make sure that no runs with unknown trigger–efficiencies enter the analysis, the response of the trigger electronics is checked for every event on L5 (see [12]). For every run, the result of this verification of the *zVtx*–trigger is stored in the central H1 database. Four entries in the *XMO1*–bank as listed in Table A.6 represent the reliability of the trigger.

For each of these quantities, a mean verification value is given, together with its statistical error. Only events with a *zVtx–t*0 in real data or in the offline simulation are counted. Since this verification is done at the L5 step, no events rejected at any of the previous trigger levels enter in the statistical ensemble. Therefore we may be highly biased towards good physics events. Events triggered by a randomly malfunctioning L1 system are mostly rejected at the L4 filter farm and do therefore not appear in this statistics. Hence a malfunction can best be detected from the value of *ZVHIST*, and not from the *ZVT0* value. For the $D^\star$ analysis, a cut of 98 % verification of the *zVtx*–

histogram[5] and an ensemble of more than 200 tested events per run has been required.

Label	Meaning
ZVHIST	trigger histogram has been calculated correctly
ZVT0	*zVtx*–*t*0–trigger element correct
ZVALL	all *zVtx*–trigger elements correct
ZVBR	central *BigRays* correct

Table A.6: *Entries in the XMO1–bank for the verification of the zVtx –trigger.*

[5]The desired value of 100 % has often not been reached as one *Adder Card* used to deliver slightly too low values in the case of large events. The impact of that effect on the trigger efficiencies is however negligible.

Appendix B

Efficiency of CIP 1995-97

A replacement of *CIP* is being designed in order to satisfy the increasing demands for tracking and triggering after the lumiosity upgrade of HERA [73]. It is therefore interesting to check whether any efficiency drop could be observed in the existing chamber due to ageing during the last years.

The selection of tracks used for the present efficiency calculations has been described in Reference [12]. This procedure does not need subtriggers independent of the proportional chambers which barely exist. It obtains a sample of bias free tracks by requiring that the event would have been triggered equally without the corresponding particle.

This selection of *CJC* tracks defines the track sample *all_tracks*. Efficiencies calculated from this sample change drastically from one year to the other because of dead high-voltage sectors and broken readout cables. In order to be more sensitive to small variations of the pad efficiencies, this selection has been tightened, excluding tracks hitting dead channels. This selection has been based on the thresholds used to reproduce the chamber response in the *MC* simulation [1]. The *living_pads* selection excludes all dead pads (indicated black in Figure B.1 [2]) plus a few others with known malfunction [3]. The remaining sample has been called *living_pads*

[1] As the calulation of the thresholds has not yet been repeated with the 97 data, the values obtained from 96 are used for 1997, where known changes (repair during the shutdown) have been implemented.

[2] The dead sectors in CIP1 1995 were due to two broken anode wires where every wire affected three HV channels or $1\frac{1}{2}$ sectors. Most of the dead channels in 1996 were caused by damaged signal cables. In 1997, two preamplifiers with 15 channels each were wrongly connected to the chamber.

[3] For most of the *minimum bias runs* the HV of CIP0, ϕ–sector 2, had to be significantly

and should give much more accurate information about the performance of the operational part of the chamber. Figure B.2 compares the efficiencies calculated from these two samples for the second half of the 1997 running.

For some periods in 1997, the efficiency calculations suffered significantly from the presence of 'ghost tracks' in the *CJC* reconstruction, which do not correspond to real particles but rather are random combinations of hits. Even though these tracks affected the *COP* efficiencies much more than the *CIP* and have been suppressed by a tighter track selection [74] [4], the possibility of finding some kind of unphysical tracks in the sample remained. It has been improved by defining the *cip_validated* subsample: *living_pad* tracks are only used for the efficiency determination of *CIP* layer 1, if in addition *CIP* layer 0 has been efficient and vice versa. Requiring a signal from the neighbouring chamber guarantees, that there has really been a particle going through the chamber. Of course, regions excluded by the *living_pads* requirement in one layer of the chamber are now absent in the efficiency calculation of both layers.

Table B.2 has been determined from the *living_pad* sample. The last column (3) gives the measured inefficiency for an 'OR' of both chambers. One would expect that to be the product of the inefficiencies of both layers (column (1)), which is obviously not the case. Two reasons are possible for this effect: a) it can be due to 'ghost tracks' which do not have corresponding hits in any chamber; b) it is due to the fact that the efficiencies are not constant along the z–position of the pads (see Fig B.2 d)). To check the relative importance of the two effects, column (2) has been calculated from the single chamber efficiencies, taking into account the z–dependence of the efficiencies. The discrepancies between column (2) and (3) can be used as a first estimate of the systematic error of the efficiency determination.

Conclusions

Changes in the HV setting of the chamber are listed in Table B.1 . The determined efficiencies can be read from Table B.2 or Figure B.3 . The increase in efficiency of CIP0 from 95 to 96 can clearly be correlated to the change of the HV setting. The jump from bin 7 to bin 8 coincides with a

lowered due to frequent trips. That sector had therefore also been excluded from the *living_pad* selection for the entire 1997 data.

[4] Most of these tracks are measured in the outer *CJC* only and can therefore be rejected by requiring the starting radius to be less than 25 cm.

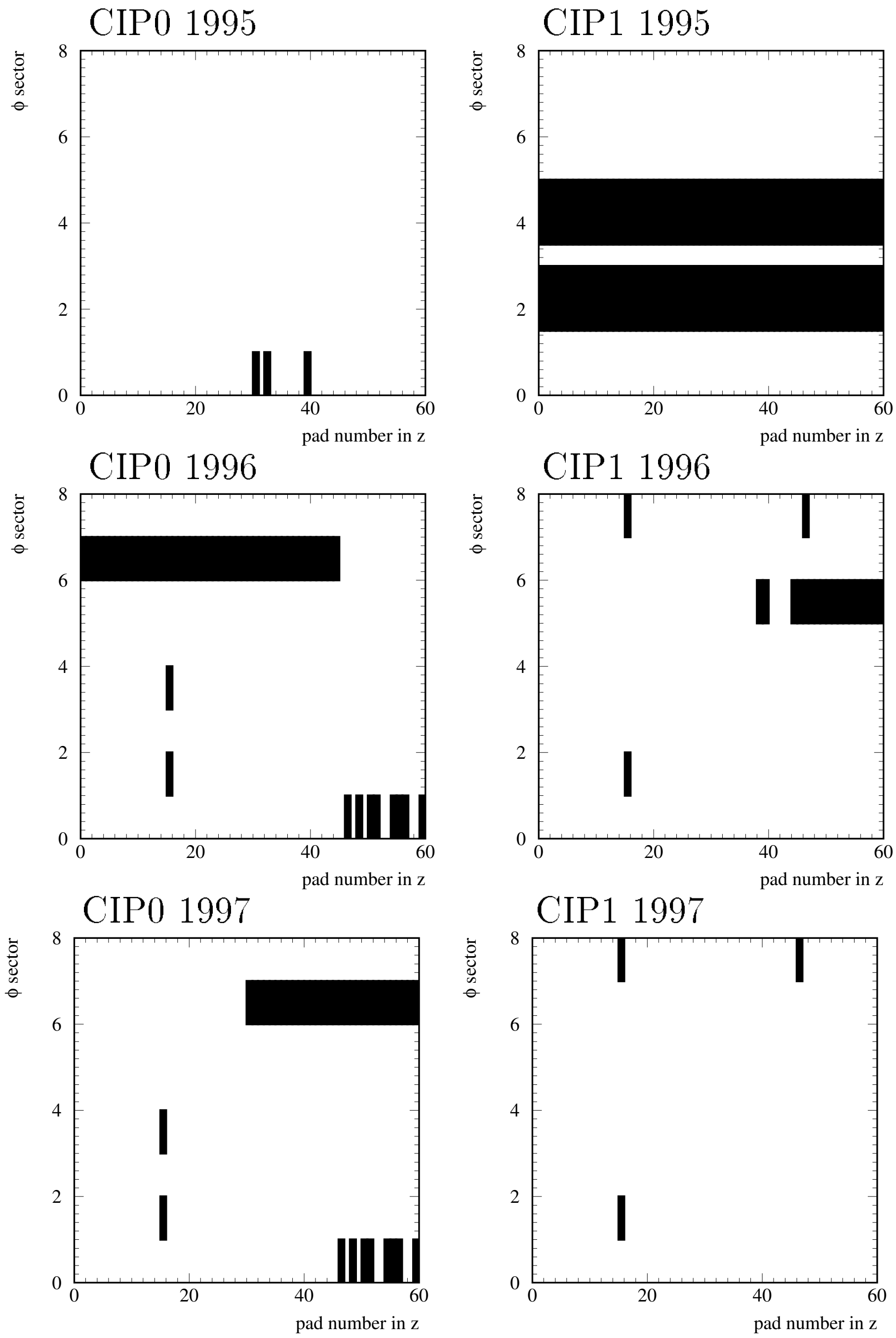

Figure B.1: *Dead channels of CIP 1995-97.*

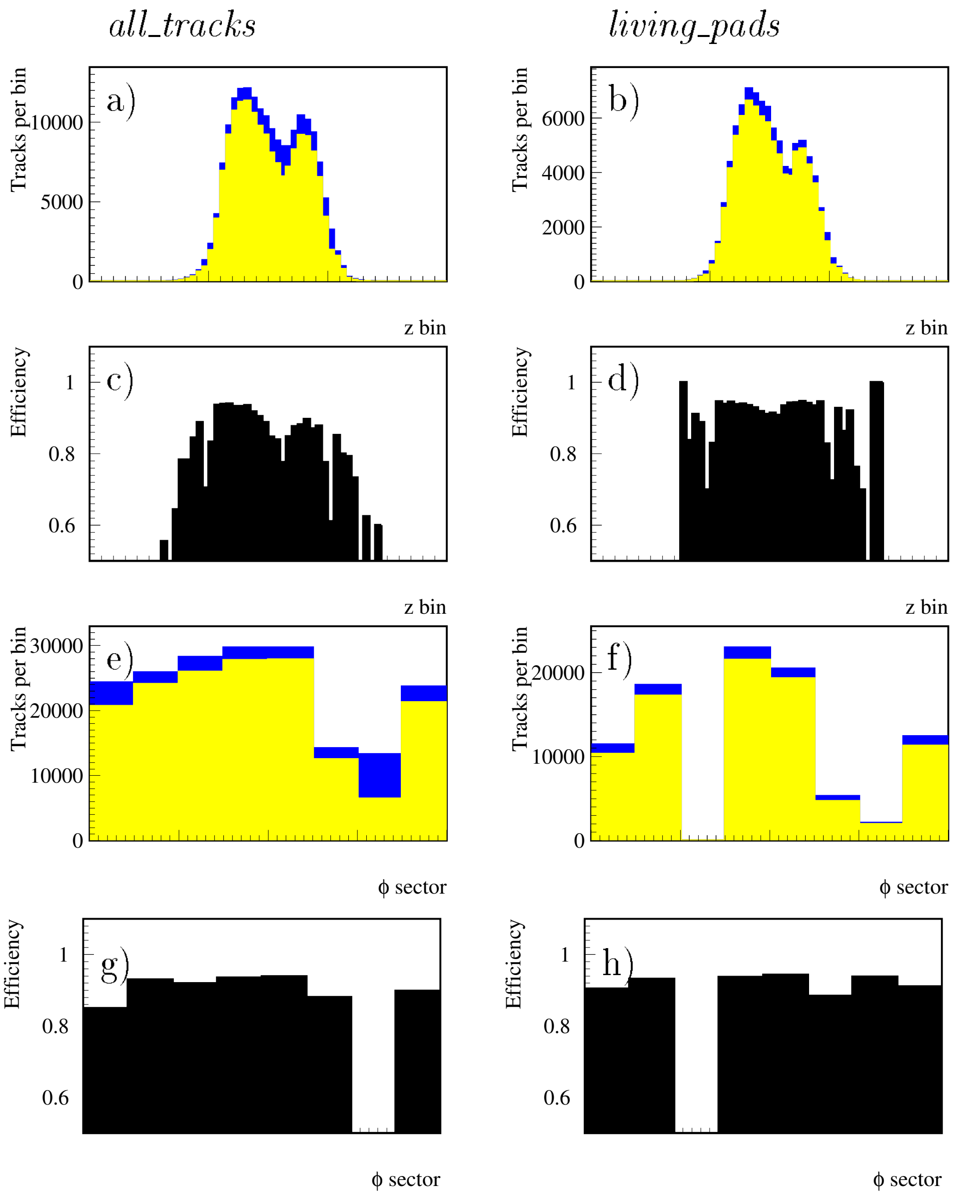

Figure B.2: CIP *0 efficiency 1997 (bin 7 in Table B.2). Plots a), b), e), f): number of selected tracks per bin (dark grey) and number of tracks (grey) with a signal in the chamber. Plots c), d), g), h): corresponding efficiencies; only efficiencies greater than 50 % are shown. Plots a) - d): as a function of the z–position of the hit pads. Plots e) - h): as a function of the ϕ–sector. Plots a), c), e), g) have been determined using the all_tracks selection, b), d), f), h) are based on living_pad tracks.*

bin	first run last run	year	corresponding bins in Table B.2	HV CIP0	HV CIP1
A	101008 131045	95	1, 2	2530 V	2500 V
B	144732 149727	96	3	2550 V	2500 V
C	150291 171573	96	3, 4, 5	2550 V	2510 V
D	176421 188637	97	6	2550 V	2500 V
E	188777 201519	97	6, 7, 8[3]	2550 V	2510 V

Table B.1: *High Voltage settings of* CIP *[75].*

drastic change of the trigger mix of H1, from the standard setting to the *minimum bias* setup. On the first glance one might suspect that this jump indicates that the track selection is not as bias free as it should be — such an effect would however lead to the opposite effect, an efficiency drop: the *minimum bias* setup accepted a much larger fraction of events without *zVtx*–trigger requirement than the standard setting. It seems much more probable that this apparent increase in efficiency is due to changed geometrical properties of the used track sample. Especially an increase of the statistical weight of low θ tracks would lead to higher efficiencies[5]. Similar arguments are to be checked carefully before one may conclude whether the drop from bin 5 to bin 7 must be attributed to a real efficiency loss of the chamber or rather to some artificial effect of this measurement. The fact that the efficiency curves of both chambers show a very similar behavior would be well explained by a systematic effect. However both layers of CIP have of

[5]For low angle tracks, the track length in the active part of the gas volume is longer and hence more primary ionization is generated. This effect is very critical if we want to calculate the global efficiency of the chamber. It is however no problem for the tuning of the *MC* description since there the efficiency measured with a sample of tracks is compared to the simulated response for the very same sample.

bin	first run last run	running period	♯ of used tracks	inefficiency $(1-\epsilon)$				
				CIP0	CIP1	CIP(0∨1)		
						1	2	3
				[%]	[%]	$[10^{-3}]$	$[10^{-3}]$	$[10^{-3}]$
1	110946 125847	1995 part 1	172025	7.5	5.3	4.0	4.6	9.4
2	125960 131045	1995 part 2	54122	7.3	4.9	3.6	4.2	8.9
3	146416 157300	1996 'RAL'	51968	5.4	5.2	2.8	3.6	8.4
4	157340 163276	1996 'LYON'	117307	5.2	5.0	2.6	3.3	7.2
5	163318 171156	1996 'DESY'	127830	6.1	4.9	3.0	3.7	15.1
6	182667 195353	1997 part 1	174851	6.1	5.1	3.1	3.9	9.0
7	195667 200407	1997 part 2	117564	7.3	6.0	4.4	5.3	11.0
8	200445 201519	1997 min. bias	63798	5.3	4.3	2.3	3.0	6.7

Table B.2: *Run ranges for* CIP *efficiency determination. The inefficiencies are determined using the* living_pad *track selection. See text for more explanations.*

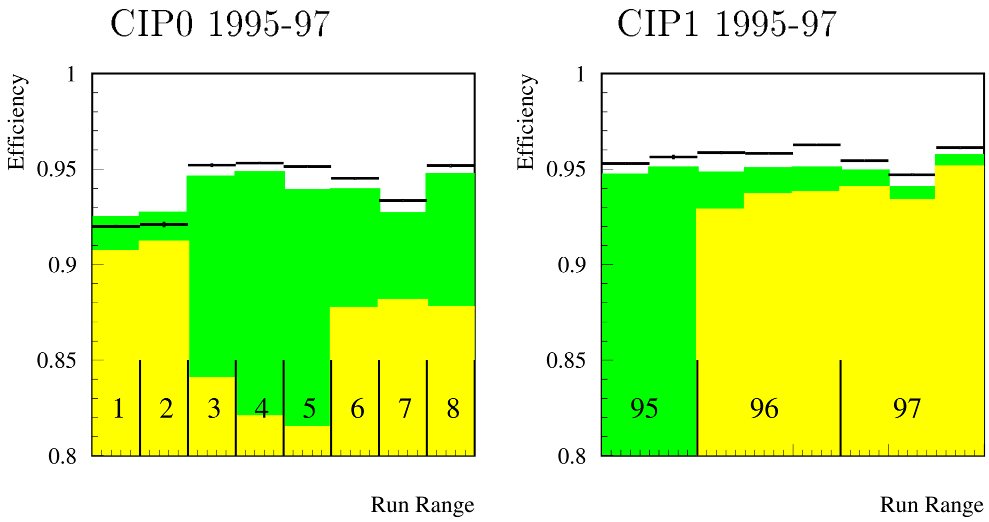

Figure B.3: CIP *efficiency for different run ranges 1995-97 (see Table B.2 for the definition). The light grey histogram has been determined from the* all_tracks *sample, the dark histogram corresponds to the* living_pads *and the black lines represent the* cip_validated *selection. Statistical errors are negligible.*

course experienced the same ammount of radiation during the last years and might therefore simultaneously degrade.

To better understand the efficiencies at the percent level, further studies of the systematics of that measurement would be needed.

Appendix C

SpaCal Calibration

The cell by cell calibration of the *SpaCal* has been continuously improved during 95. It is based on a cell–wise kinematical peak method [76], as well as on a comparison of the cell response to cosmics [77]. In the outer region, a method based on beam halo muons has been used, too [78]. Final correction factors to the analyzed data have been applied at the analysis step [46]. A global uncertainty on the overall energy scale for the data recorded early in 95 however remained. It was checked and corrected as described in the following.

The calibration procedure makes use of the redundancy of the H1 detector for the reconstruction of the *DIS* kinematics. Taking the measured value of y_Σ, the energy of the scattered positron can be denoted as

$$E_{e'}^{expected} = \frac{E_e \times (1 - y_\Sigma)}{\sin(\frac{\theta_e}{2})} \ . \tag{C.1}$$

At very low values of y, this method leads to a much more accurate determination of the energy than can be obtained with the *SpaCal* itself. Of course the energy measured by the *SpaCal* is much more accurate at moderate and high values of y. Therefore we must select events with a very low y_Σ [1]. The distribution of the energies measured by the *SpaCal* is then plotted for data and Monte Carlo. A difference in the mean value indicates a miscalibration of the calorimeter and must be corrected by shifting the measured energies

[1]Since we are limited by statistics and the number of $D^\star$ events drops significantly for $y_\Sigma \leq 0.04$, we have used all events with $0.02 \leq y_\Sigma \leq 0.10$. With inclusive *DIS* data samples one can go to lower y values.

accordingly. If the width of the distribution is larger in data than in *MC*, this most probably reflects problems with the intercalibration between different cells. It has been accounted for by smearing the energies in the Monte Carlo description.

This calibration method works of course only if the y_Σ distributions are the same for data and *MC*. This has not been the case, the *MC* does not describe the cutoff of events at low y, most probably due to the changing signal to background ratio in the data. Since on this step here we are only interested in a correct understanding of the detector and not of the γ*–gluon* fusion process, we can simply assign weights to the *MC* events such that the y_Σ distributions agree (see Figure C.1).

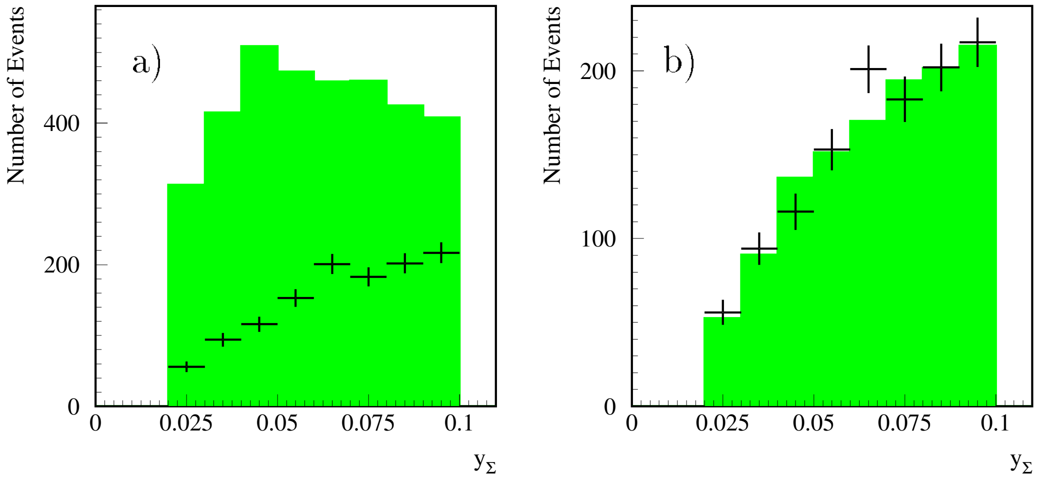

Figure C.1: SpaCal *calibration: a) Distribution of data (black crosses) and* MC *as a function of* y_Σ*. In b) the* MC *events have been assigned weights in order to reproduce the distribution of the data.*

The data set has been split into four run ranges with comparable luminosity. Independent calibration constants have been calculated for each of these ranges (see Table C.1). As a nice confirmation of the present calibration procedure, the correction factor determined for the last run period was very small. This must be the case since for this run period an optimal calibration was guaranteed by the *SpaCal* group.

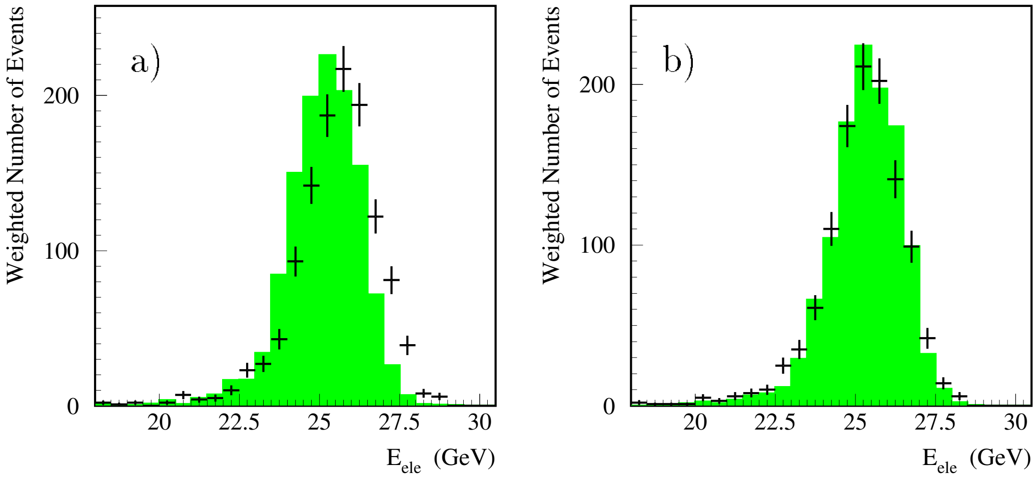

Figure C.2: *a) Energy spectrum of the selected events after weighting, but before calibration factors have been applied. The grey histogram shows the distribution of the* MC*, the crosses are the entire 95 data set. For b) an energy shift of* $\approx 1.5\%$ *for the data and a gaussian smearing of* $\pm 1\%$ *for the MC have been applied, exactly as in the analysis.*

first run	last run	correction factor applied to the data [%]	smearing applied to the MC [%]
100000	122499	-1.62	1.0
122500	123749	-2.20	1.0
123750	125959	-2.15	1.0
125960	200000	+0.58	1.0

Table C.1: *Calibration constants for the* SpaCal.

Bibliography

[1] F. Halzen, A. Martin, *Quarks & Leptons*, 1984, John Wiley & Sons.

[2] B. Martin, G. Shaw, *Particle Physics*, 1992, John Wiley & Sons.

[3] R. K. Ellis, W. J. Stirling, B. R. Webber, *QCD and Collider Physics*, 1996, Cambridge University Press.

[4] G. Wolf, *HERA Physics*, 1994, DESY internal report DESY 94-022.

[5] E. D. Bloom et al., Phys. Rev. Lett. 23, (1969) 930.

[6] M. Breitenbach et al., Phys. Rev. Lett. 23, (1969) 935.

[7] J. Aubert et al., EMC Collab., Nucl. Phys. B213 (1993) 31 .

[8] M. Bonesini et al., Z. Phys. C38, (1988) 371.

[9] C. Adloff et al. (H1 Coll.), Z. Phys. C74 (1997) 191.

[10] C. Adloff et al. (H1 Coll.), Nucl. Phys. B497 (1997) 3.

[11] K. Müller, *Measurement of the Proton Structure Function F_2 at low Bjorken x at the H1 Experiment*, 1994, PhD Thesis, Universität Zürich.

[12] H. P. Beck, *Measurement of the Total Photoproduction Cross Section at the Electron Proton Collider HERA at $W_{\gamma P}$ of 200 GeV*, PhD Thesis, 1996, Universität Zürich.

[13] S. Aid et al. (H1 Coll.), Nucl. Phys. B472 (1996) 32.

[14] M. zur Nedden, PhD Thesis, Universität Zürich, in preparation.

[15] S. Aid et al. (H1 Coll.), Nucl. Phys. B470 (1996) 3.

[16] M.A.G. Aivazis, F.I. Olness and W.K. Tung, Phys. Rev. D50 (1995) 3085; M.A.G. Aivazis, J.C.Collins, F.I. Olness and W.K. Tung, Phys. Rev. D50 (1995) 3102.

[17] M. Buza, Y. Matiounin, R. Migneron, J. Smith and W.L. van Neerven, Nucl. Phys. B472 (1996) 611.

[18] E. Zijlstra and W.L. van Neerven, Phys. Lett. B272 (1991) 127; Nucl. Phys. B383 (1992) 525.

[19] E. Laenen, M. Buza, B.W. Harris, Y. Matiounine, R. Migneron, S. Riemersma, J. Smith, W.L. van Neerven, Proc. of the Workshop *on Future Physics at HERA*, Hamburg, 1995, Eds. G. Ingelmann et. al., DESY, 1996, (393); `http://www.desy.de/~heraws96/` .

[20] C. Adloff et al. (H1 Coll.), Z. Phys. C72 (1996) 593.

[21] G. Ingelman , J.Rathsman and G.A. Schuler, DESY preprint, DESY 96-058, and hep-ph/9605285.

[22] Application Software Group, 1994, CERN, Computing and Networks Division.

[23] G. Ingelman, Proc. of the Workshop *Physics at HERA*, Hamburg, 1992, eds. W Buchmller and G Ingelman DESY, Hamburg, 1992 (1366-1394). TSL/ISV-92-0065 .

[24] R.M. Barnett et al., Physical Review D54, 1 (1996) and 1997 off-year partial update for the 1998 edition available on the PDG WWW page `http://pdg.lbl.gov/` .

[25] J. Chrin, Z. Phys. C 36, (1987) 163.

[26] R. van Wouldenberg et. al., Proc. of the Workshop *Physics at HERA*, Hamburg, 1991, Eds. W. Buchmüller, G. Ingelmann, vol. 2, p. 739.

[27] B. W. Harris, J. Smith, Phys. Rev., D : 57 (1998) 2806 5. FSU-HEP-970527.

[28] B.W. Harris, J. Smith, Nucl. Phys. B 452 (1995) 109.

[29] M. Cacciari and M. Greco, Phys. Rev. D55 (1997) 7134.

[30] H. L. Lai and W. K. Tung, Z. Phys. C 74, 463 (1997).

[31] M. Glück, E. Reya and A. Vogt, Z. Phys., C 67,433 (1995).

[32] ALEPH, DELPHI, L3 and OPAL Collab., Nucl. Instrum. Mehtod A378 (1996) 101.

[33] I. Abt et al., Nucl. Inst. Meth. A386 (1997) 310, 348.

[34] F. Sefkow et al., *Experience with the First Level Trigger of H1*, H1 internal note H1-11/94-407 (1994).

[35] J. Riedlberger, *The H1 Trigger with Emphasis on Tracking Triggers*, H1 internal note H1-01/95-419 (1995), 5th International Conference on Advanced Technology and Particle Physics, Como, Italy, 3-7 October 1994.

[36] D.Müller, F.Sefkow, *Improving the z-Vertex Trigger*, H1 internal note H1-04/98-539 (1998).

[37] J.C. Bizot et al., *Proposal for a topological level 2 trigger*, H1 internal note H1-06/91-181 (1991); *Hardware Study for a topological level 23 trigger*, H1-09/92-240 (1992).

[38] J. Köhne et al., *Realization of a Second Level Neural Network Trigger for the H1 Experiment at HERA*, H1 internal note H1-01/97-509 (1997).

[39] R. Prosi , *The 1994 L4 Filter Farm Selection Algorithm* , H1 internal note, H1-03/95-433 (1995).

[40] S.Egli et al., *Calculating Event Weights in Case of Downscaling on Trigger Levels 1-4*, H1 internal note, H1-04/97-517 (1997).

[41] A. Meyer, *Measurement of the Strucure Function $F_2(x, Q^2)$ of the Proton at Low Q^2 with the H1 Detector at HERA Using the New Detector Components SpaCal and BDC*, PhD Thesis, 1997, Univ. Hamburg, H1 internal report DESY FH1-97-01.

[42] E. Tzamariudaki, *Performance of the H1 Lead/Scintilating-Fibre Calorimeter*, Proceedings of CALOR97, VII International Conference on Calorimetry in High Energy Physics, Tucson, USA, November 1997.

[43] V. Boudry et al., *The Inclusive Electron Trigger for SPACAL: Design and CERN-Test Results*, H1 internal note H1-03/95-430 (1995).

[44] R. Wallny, *Untersuchung des strahlinduzierten Untergrundes bei der Datennahme von Ereignissen der tief-inelastischen Streuung durch den H1-Detektor bei HERA*, Diploma Thesis, 1996, Universität Heidelberg, unpublished.

[45] M. Kander, private communication.

[46] A. Meyer, private communication.

[47] U. Langenegger, private communication.

[48] U. Bassler, G. Bernardi, *On the Kinematic Reconstruction of Deep Inelastic Scattering at HERA*, DESY report 94-231, (1994), hep-ex/9412004.

[49] U. Bassler, G. Bernardi, *Structure Function Measurements and Kinematic Reconstruction at HERA*, DESY report 97-137 (1997), Submitted to Nucl.Instrum.Methods, hep-ex/9801017.

[50] A. Kwiatkowsky, H. Spiessberger and H.J. Mohring, Comput. Phys. Commun. 69 (1992) 155.

[51] A. Arbuzov, D. Bardin, J. Blümlein, L. Kalinovskaya and T. Riemann, Comp. Phys. Comm 94 (1996) 128.

[52] F. Lehner, private communication.

[53] V. Karimäki, Nucl. Inst. Meth. A305 (1991) 187

[54] V. Blobel, 1984, DESY report 84-118, Proceedings CERN, Geneva, 1985, CERN 85-09 88-127.

[55] F. James, CERN Program Library Long Writeup D506.

[56] K. Daum, private communication, 1997.

[57] St. Hengstmann, private communication, 1998.

[58] U. Langenegger, PhD thesis, 1998, ETH Zürich, in preparation.

[59] Y. Tsipolitis, Proc. of the DIS98 conference, Brussels 1998, to be published.

[60] N. Gogitidze, S. Levonian, H1 internal note H1-02/96-471

[61] J. Katzy *Messung der Strukturfunktion F_2 bei kleinen Bjorken-x und kleinen Impulsüberträgen am H1-Experiment bei HERA*, PhD thesis, 1997, Universität Heidelberg.

[62] W. Erdmann, *Untersuchung der Photoproduktion von D*-Mesonen am ep-Speichering HERA*, PhD Thesis, 1996, ETH Zürich, ETH No. 11441 and ETHZ-IPP 96-01.

[63] G. D'Agostini, Nucl. Inst. Meth. A362 (1995) 487.

[64] Fortran code available through `http://zeus.roma1.infn.it/pub/bayes_distr.txt` with additional information in `http://zeus.roma1.infn.it/pub/bayes_comments.ps`

[65] C. Adloff et al. (H1 Coll.) *Determination of the Gluon Density in the Proton from Deep Inelastic ep Charm Production using NLO QCD*, Submitted to the International Europhysics Conference on High Energy Physics, HEP97, Jerusalem, Israel, August 1997; Abstract 275.

[66] F. Sefkow, private communication, 1998.

[67] V. Shekelian, Preprint DESY 97-248; Proc. of 18th International Symposium on Lepton-photon Interactions, Hamburg 1997, 22, 1997.

[68] S. Eichenberger, *Development of the Ray Finder Electronics for the z-Vertex Trigger for the H1 Detector at HERA*, Diploma Thesis, 1988, Universität Zürich, unpublished.

[69] S. Eichenberger, *A Fast Pipelined Trigger for the H1 Experiment at HERA Based on Multiwire Proportional Chamber Signals*, PhD Thesis, 1993, Universität Zürich.

[70] S. Schiek, G. Schmidt, private communication; S. Schiek, *Untersuchung der inelastischen Photoproduktion von J/ψ-Mesonen im H1-Detektor bei HERA*, PhD Thesis, 1996, Univ. Hamburg,

[71] D. Müller, *Topological Coincidences between Tracking and Calorimetric Triggers at the H1 Experiment*, Diploma Thesis, 1994, Universität Zürich, unpublished.

[72] C. Beigbeder, D. Breton, *H1 PQZP System*, H1 internal note, H1-02/93-269 (1993).

[73] M. Cuje et al., *H1 High Lumiosity Upgrade 2000, CIP and Level 1 Vertex Trigger* H1 internal report, 1997.

[74] R. Roosen, private communication, 1998.

[75] M. zur Nedden, private communication, 1998.

[76] H1 BEMC Group, DESY 95-177 and [41].

[77] A. David, *Calibration of the SpaCal with Cosmics*, Diploma Thesis , Universität Hamburg, 1997 and M. Dirkmann *Calibration of the SpaCal with Cosmics*, H1 internal note H1-05/96-477, 1996.

[78] C. Arndt *Calibration of the Spaghetti-Calorimeter using Halo Muons*, Diploma Thesis, Universität Hamburg, 1995 (in German), unpublished.

List of Tables

List of Figures

Acknowledgments

I would like to thank Prof. Dr. P. Truöl for giving me the chance to participate in the H1 experiment. The great trust he has put in me allowed me to define many of my aims myself.

While doing this analysis I was strongly supported by Felix Sefkow. Without his optimism and experience I would never have been able to complete the measurement. I would also like to thank him for running the HVQDIS program and for his pioneering efforts in the use of the unfolding procedure.

I would like to extend my thanks to Martin zur Nedden and Stefan Hengstmann; the use and debugging of a common nTuple was not the only point where we could join our efforts. Also the time we spent together keeping CIZ, CIP and the zVtx–trigger up and running will be well remembered.

The progress of this analysis has been repeatedly discussed in the Heavy Quark Working Group of H1. The feedback provided invaluable help.

For the understanding of the photon kinematics I got excellent support from the ELAN Working Group and from the SpaCal experts. I would like to thank U. Bassler, A. Meyer, V. Shekelian, E. Tzamariudaki and R. Wallny. F. Lehner executed the calculation of the radiative corrections.

Special thanks go to all those people, who gave good ideas and advice every day and enriched my time in Hamburg: the 'swiss collaborators' Christoph, Daniel, Felix, Hans Peter, Hubert, Johannes, Josef, Katharina, Martin, Monika, Peter, Ueli, Urs, Stefan, Thomi and Yorgos from University and ETH, Rainer and the entire H1 collaboration.

Last but not least I want to thank my parents and Renate for their continuous support and for the wonderful time we could share so far!

This work has been supported by the Swiss National Science Foundation.

Curriculum Vitae

Personalien:

Name:	David Peter Müller
Bürgerort:	Zollikon und Pfäffikon ZH
Geboren:	26. 4. 69, Zürich

Bildungsgang:

1976 - 84	Primar- und Sekundarschule in Zollikon und Pfäffikon
1984 - 88	Kantonsschule Zürcher Oberland, Wetzikon, Matura Typus C
1989 - 94	Studium der Physik (Mathematik, Astronomie) an der Universität Zürich
1991 - 92	Mobilitätssemester an der Universität Lausanne
1993 - 94	Diplomarbeit in Experimentalphysik unter der Leitung von Dr. U. Straumann und Prof. Dr. P. Truöl
1994	Diplom in Experimentalphysik
1995	Diplom für das höhere Lehramt des Kantons Zürich
1995 - 1998	Wissenschaftliche Mitarbeit beim H1 Experiment am DESY Hamburg, Dissertation bei Prof. Dr. P. Truöl.

Dozentenverzeichnis:

Universität Zürich:

C. Amsler	D. Brinkmann	E. Brun	H. P. Dreyer
St. Egli	R. Engfer	M. Greuter	R. Gunz
P. Hess	H. Jarchow	H. Keller	W. Kündig
M. Mali	H. Müller	H. Nussbaumer	R. E. Pixley
H. S. Pruys	G. Rasche	W. Reichart	G. Scharf
W. Schmutz	N. Straumann	U. Straumann	P. Truöl
W. Vogel	D. Wyler		

Universität Lausanne:

G. Chapuis	T. Courvoisier	R. Huguenin	H. Kunz
J.-C. Mermillod	A. Quattropani	W. D. Schneider	G. Wanders